Validation of Computational Fluid-Structure Interaction Models By Comparison with Collapsible Tube Experiments

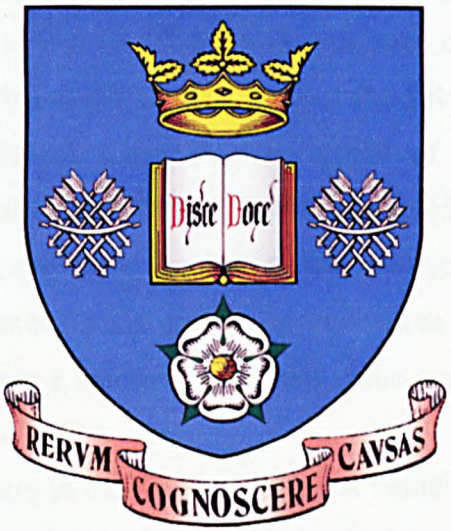

PhD Thesis

By

Richard A. Scroggs

mep97ras@sheffield.ac.uk

Supervised By

Dr S. B. M. Beck

Professor E. A. Patterson

Department of Mechanical Engineering

The University of Sheffield

August 2001

Summary

The objective of this thesis was to assess the validity of the fluid-structure interaction (FSI) facilities in LS-DYNA for the analysis of highly deformable structures interacting with flowing viscous fluids. The collapsible tube experiment was chosen as a validation tool for FSI since its three-dimensional computational modelling would have been impossible if the viscous internal fluid flow were not considered. An explicit three-dimensional finite element model of a collapsible-tube was constructed and solved using LS-DYNA. The fully coupled model included internal fluid flow; external, inlet and outlet pressures; tube wall tension; pre-stressing; and contact. The finite element boundary conditions were taken as the recorded values of flow rate and pressure from a standard collapsible-tube experiment for both steady and unsteady flows.

The predicted tube geometry in the steady LS-DYNA model showed good agreement with the experiment for operating points in the highly compliant region of the pressure-flow characteristic curve. The comparative position of the pinch at the outlet end differed by only 5.6% of the outlet diameter in the worst case.

This analysis represents an advance on other published work in that previously no comparison with experiments have been drawn for FSI models involving high Reynolds number flowing viscous fluids interacting with highly deformable three-dimensional structures. This analysis successfully made that comparison and the experimental and computational results have combined to form a more detailed picture of the collapsible-tube phenomenon by including detailed stress results of the tube walls and views of the internal fluid flow.

The collapsible tube model exhibited uncertainty errors due to the use of a coarser than desirable mesh and a reduced fluid speed of sound. Although both these approximations caused significant error in the model both were necessary in order to achieve acceptable solution times. Because of these errors a thorough quantitative validation could not be achieved although LS-DYNA has been proven to be qualitatively accurate. Increases in computing speed are required before thorough quantitative validation of FSI can be achieved by comparison with the collapsible-tube experiments.

Contents

SUMMARY **2**

CONTENTS **3**

NOMENCLATURE **7**

1 INTRODUCTION **8**

2 LITERATURE REVIEW **11**

2.1 COLLAPSIBLE TUBE THEORY AND LITERATURE REVIEW 11

2.1.1 Experimental Set-Up *11*

2.1.2 Steady Flow *12*

2.1.3 Unsteady Flow (Self-Excited Oscillations) *17*

2.1.3.1 Onset Of Oscillations 18

2.1.3.2 Frequency And Waveform Of Oscillations 19

2.1.3.3 Theoretical Methods For The Prediction Of The Breakdown Of Steady Flow 20

2.1.4 Finite Element Investigations Of Collapsible Tubes *22*

2.2 FINITE ELEMENT MODELLING OF FSI SYSTEMS 23

2.2.1 Viscous Fluid Interacting With Flexible Structures *23*

2.2.2 Other Examples of FSI *24*

3 NUMERICAL FORMULATIONS FOR FLUID-STRUCTURE INTERACTION **26**

3.1 ELEMENT FORMULATIONS 27

3.1.1 Lagrangian Formulation *27*

3.1.2 Eulerian Formulation *28*

3.1.3 Arbitrary Lagrangian-Eulerian Formulation *29*

3.2 TIME INTEGRATION 31

3.2.1 Implicit Method *31*

3.2.2 Explicit Method *33*

3.2.3 Implicit Verses Explicit Methodologies *34*

3.3 SELECTION OF AN FSI TECHNIQUE 36

4 ANALYSIS SOFTWARE AND HARDWARE **38**

4.1 LS-DYNA TECHNIQUE 38

4.1.1 Structural Elements *38*

4.1.2 Fluid Elements And The Equation Of State *39*

4.1.2.1 Equation Of State 40

4.1.3 Time-Step Control *41*

4.1.4 Boundary Conditions *43*

4.1.5 Fluid-Structure Coupling ... *45*
4.1.6 Artificial Viscosity ... *46*
4.1.6.1 Bulk Viscosity ... 46
4.1.6.2 Hourglass Viscosity ... 46
4.1.7 Units ... *48*
4.1.8 Pre- And Post- Processing For LS-DYNA ... *48*

5 COLLAPSIBLE TUBE EXPERIMENTS ... 50

5.1 CONSTRUCTION OF THE EXPERIMENT ... 50
5.1.1 Data Retrieval ... *50*
5.1.2 The Airtight Container ... *51*
5.1.3 Material Properties Of The Penrose Tube ... *54*
5.1.3.1 Wall Thickness ... 54
5.1.3.2 Density ... 54
5.1.3.3 Stress/Strain Characteristics ... 55
5.1.4 Mounting The Tube In The Airtight Container ... *57*
5.1.5 Other Components ... *58*
5.2 THE ZERO FLOW EXPERIMENT ... 58
5.2.1 Method ... *59*
5.2.2 Results ... *59*
5.2.3 Conclusions Drawn From The Zero Flow Experiment ... *60*
5.3 STEADY FLOW EXPERIMENTS ... 60
5.3.1 Method ... *61*
5.3.2 Results And Discussion ... *61*
5.4 UNSTEADY FLOW EXPERIMENTS ... 65
5.4.1 Method ... *65*
5.4.2 Results And Discussion ... *65*
5.4.3 Conclusions Drawn From Unsteady Flow Experiments ... *70*

6 PRELIMINARY VERIFICATION OF FSI IN LS-DYNA ... 71

6.1 MESH INDEPENDENCE ... 72
6.1.1 The Test Model ... *72*
6.1.2 Results ... *72*
6.2 TIME-STEP INDEPENDENCE ... 76
6.3 FLOW OVER A CYLINDER ... 78
6.3.1 Theory Concerned With Flow Over A Cylinder ... *78*
6.3.2 LS-DYNA Model Of Flow Over A Cylinder ... *81*
6.3.2.1 Model Construction ... 81
6.3.2.2 Results ... 82

7 MODELLING OF THE COLLAPSIBLE-TUBE USING LS-DYNA ... 85

7.1 CONSTRUCTION AND DEVELOPMENT OF THE LS-DYNA MODEL ... 85

7.1.1 Fluid and Structure Discretization *86*
7.1.2 Contact *88*
7.1.3 Preforming The Tube *89*
7.1.4 Tube Tension *90*
7.1.5 Material Properties *91*
7.2 CALIBRATION OF TUBE MATERIAL USING NO-FLOW SIMULATIONS 91
7.2.1 Model Properties *92*
7.2.2 Results *92*
7.2.3 Calibration Technique *94*
7.3 STEADY FLOW MODELS 95
7.3.1 Model Properties *95*
7.3.2 Results *96*
7.3.2.1 Effect of a Longer Outlet Tube and Higher Fluid Speed of Sound 98
7.3.2.2 Fluid Velocity Profiles 100
7.3.2.3 Stresses in the Tube Walls 102
7.4 UNSTEADY FLOW 110
7.4.1 Model Properties *110*
7.4.2 Results *111*

8 DISCUSSION 116

9 CONCLUSIONS 123

10 ACKNOWLEDGEMENTS 124

11 REFERENCES 125

A. PHYSIOLOGICAL EXAMPLES OF COLLAPSIBLE TUBES 129

A.1 VEINS 129
A.2 ARTERIES 130
A.3 LUNGS 130
A.4 AUTOREGULATION OF BLOOD FLOW 131
A.5 URETHRA 131
A.6 DIAGNOSTIC EQUIPMENT 132
A.7 EUSTACHIAN TUBE 133

B. CALCULATION OF GLASS THICKNESS 135

C. THE CONRAD EXPERIMENTS 136

C.1 METHOD 136
C.2 RESULTS 136
C.2.1 P_E Varied, R_2 Constant *136*
C.2.2 Ratio P_E : R_2 Constant *138*

C.2.3 P_E Constant, R_2 Varied 139
C.3 Discussion Of Conrad's Experiments 140
C.4 Conclusions Drawn From Conrad's Experiments 142

D. PREFORMING OF THE TUBE WALL IN LS-DYNA 143

E. FORTRAN EXECUTABLE FOR INITIAL STRESS LOADS 144

F. KEYWORD INPUT FILE FOR LS-DYNA 145

G. EVALUATION OF FSI IN MSC.DYTRAN 150

G.1 Elements 150
G.2 Boundary Conditions 150
G.3 Pre- And Post-Processing For MSC.DYTRAN 151
G.4 MSC.DYTRAN Model Of A Collapsible Tube 151
G.4.1 Construction Of The MSC.DYTRAN Model 151
G.4.2 Model Properties 151
G.4.3 Results and Discussion 152
G.4.4 Conclusions Drawn From The MSC.DYTRAN Model 153

H. EVALUATION OF FSI IN ADINA 154

H.1 FSI In ADINA 154
H.2 Pre- And Post-Processing For ADINA 155
H.3 ADINA Model Of Flow Over A Cylinder 155

Nomenclature

P	pressure	MPa, cmH_2O
Q	volumetric flow rate	$m^3\ s^{-1}$, litres min^{-1}
A	cross-sectional area	mm^2
t	time	s
t_n	time step n	-
M	mass matrix	-
C	damping matrix	-
K	stiffness matrix	-
K	bulk modulus	MPa
F	load vector	-
a	acceleration	$mm\ s^{-2}$
v	velocity	$mm\ s^{-1}$
u	mesh velocity	$mm\ s^{-1}$
d	material displacement	mm
ρ	mass density	$kg\ m^{-3}$
ν	Poisson's ratio	-
E	Young's modulus	MPa
c	speed of sound through material	$m\ s^{-1}$
μ	fluid viscosity	Pa s
L	length	mm
W	width	mm
w	wall thickness	mm
D	diameter	mm
R	fluid flow resistance	cmH_2O(litres min^{-1}) $^{-2}$

1 Introduction

There are many physiological components where thin flexible structures interact with a fluid. Such examples include heart valves, the lungs, the bladder and the veins. Not surprisingly it has been of interest to physiologists to model these structures in order to gain an insight into their workings. Analytical modelling of such components is, in the main, not viable due to the strong fluid-structure interaction (FSI) and the asymmetry involved. Hence experiments are the only viable source of data for the analysis of such systems. However, the difficulties an experimental analyst might face are numerous. These include the vast amounts of time and expense in creating an in-vitro experiment, the availability of materials that imitate those under study or the availability of the actual biological tissues. An alternative to constructing an in-vitro experiment is to study the component in-vivo. This technique raises a whole new set of problems including the intrusive nature of data retrieval techniques; the availability and suitability of hosts; or the moral connotations attached to the investigation of components within the bodies of laboratory animals. Whichever type of experiment is performed neither can provide detailed structural data. Detailed fluid and structural data can be gained by using computational modelling. However, the lack of confidence in this technique requires thorough validation of the software for every new application. Additional problems arise when considering the FSI of the system.

Computational models of physiological components have, in the past, been separated into two distinct groups; the computational fluid dynamics (CFD) analysis of flow around a rigid structure or the finite element (FE) analysis of a flexible structure without the fluid being modelled. Although both disciplines have contributed to knowledge in the medical field they both have limitations.

In the field of heart valve research, CFD has been preferred for the fluid flow analysis around a prosthetic heart valve in a fixed position. This is an acceptable situation considering the rigid nature of a prosthetic heart valve. Such computer models can give an indication of the potential for anomalous flow patterns that may result in the deposition of blood platelets and thrombosis [1,2]. The flexibility of real or bioprosthetic valves renders such models largely useless unless the deformation of the structure can be included.

The Soft Structures Research Group (previously the Heart Valve Research Group) at The University of Sheffield has, for several years, used the explicit finite element code LS-DYNA [3] to model the opening and closing of bioprosthetic heart valves. Patterson et al [4] computationally investigated the leaflets of a bicuspid bioprosthetic heart valve. A time-varying, spatially uniform pressure differential was applied across the leaflets to model their behaviour as they advanced through the cardiac cycle. These models gave an indication as to where a leaflet might be unduly stressed and offered a tool for the improvement of the design of bioprosthetic heart valves. In such models the large deformation characteristics of the leaflets were modelled but, until recently, the interaction of the fluid with the leaflets and the effect of this interaction on the surrounding structures was ignored.

One of the aims of the Soft Structures Research Group is to create a realistic computational model of a heart valve functioning in-vivo. This model requires that the blood be included in the analysis. The advent of the coupled FSI facilities in LS-DYNA allowed the possibility of including fluid flow in these models. Carmody et al [5] have computationally demonstrated the interaction of several elastic structures within a fluid flow including the highly deformable tissue of a single leaflet of a heart valve held within a column of flowing water. More recently the FSI between a fluid and the aortic valve including the aortic root and sinus has been modelled in the opening phase of the cardiac cycle [6]. Although the results of such investigations appeared qualitatively realistic there was no real attempt at rigorous validation. Therefore an investigation was formulated in an attempt to validate the FSI facilities of LS-DYNA and to investigate more generally the techniques available for modelling the interaction between flowing viscous fluids and structures undergoing large deformations.

This was not a mathematical investigation. The purpose of this research was to assess the FSI capabilities of existing analysis software and, where possible, draw comparisons with experiments. The investigation of the mathematics involved has been kept to a basic level. For the purposes of this research it was more important to determine how different mathematical techniques were used in the study of certain phenomena and the advantages and disadvantages that they possess. The understanding of the physical problems under study was of paramount importance and it is here that a large amount of attention has been directed. This was achieved

with the extensive use of FSI experiments and by thorough research of past experimental observations.

The FSI capabilities in LS-DYNA remain largely undocumented and unvalidated. It is the users of the code that must assess and validate it to determine its suitability for their own specific requirements. The ultimate aim of this particular project was to take a lead in validating the FSI facilities of LS-DYNA for the purposes of modelling highly flexible structures interacting with viscous fluids in three-dimensions. The particular phenomenon under study was that of collapsible tubes subjected to internal fluid flow and external pressure (sections 5 and 7). However, before such a complex system could be assessed a number of preliminary studies were needed in order to investigate how LS-DYNA modelled fluids and whether it was capable of modelling flow-induced oscillations (section 6).

2 Literature Review

Examples of fluid-structure interaction (FSI) that involve large deformation of a structure within, or containing, 'flowing' fluids are abundant in the bodies of living beings. However, the numerical modelling of these FSI systems is somewhat rare. A phenomenon that has received a large amount of attention from analytical and experimental researchers is that of the collapsible tube. This phenomenon is extensively reviewed in this section since it provided a tool for comparison of the computational FSI models with experiments.

There are a rich variety of other applications where fluids interact with structures, some of these are considered at the end of this section.

2.1 Collapsible Tube Theory And Literature Review

The fluid flow through collapsible axisymmetric tubes has long been of interest to physiologists. There are many fluid carrying vessels in the body that are elastic and can collapse when the transmural (internal pressure minus external pressure) pressure falls below a critical value (see appendix A for examples). The possibility that the collapsible tube could provide a viable model for the determination of flow through blood vessels and other tubes in the body provided an impetus to define some of the parameters of this type of flow.

2.1.1 Experimental Set-Up

The investigation of this phenomenon goes back to 1914 when Starling [7] employed a thin-walled collapsible tube as a hydraulic analogue for a vein in his canine heart-lung preparation; with which was described the intrinsic response of the heart to changes in right atrial and aortic pressure.

In the early 1940's Holt [8] investigated how the collapse of veins might affect peripheral venous pressure. He set up a model whereby water flowed from a reservoir through rigid pipe to a collapsible segment of thin-walled rubber tubing and out through more rigid pipe. A glass jacket in which the pressure was variable surrounded the collapsible segment. The inlet, outlet and external pressures were measured along with the corresponding flow rate.

Conrad [9] first presented systematic experimental pressure flow curves for both steady and unsteady flow inlet conditions of a Penrose tube (a thin-walled latex rubber tube). The experimental set-up used by Conrad is shown in Figure 2.1.

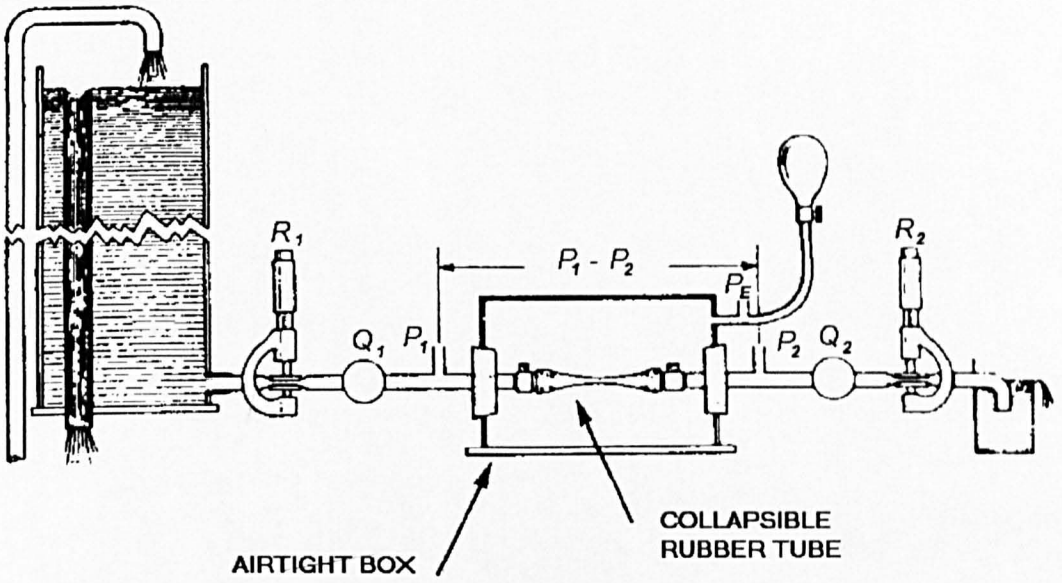

Figure 2.1 Experimental set-up used by Conrad [9]. Fluid flows from left to right. *R* = resistance, *Q* = flow measurement, *P* = pressure measurement.

Many researchers have since used this standard set-up and variations of it. An inlet reservoir feeds fluid through a resistance R_1, and into the collapsible tube section contained within an airtight box with controllable pressure P_E. The flow rate $Q_{1,2}$ and pressure $P_{1,2}$ are measured before and after the collapsible section. The fluid then flows through another resistance R_2 before exiting to an outlet reservoir.

2.1.2 Steady Flow

The method used by Conrad [9] was to fix P_E at some value relative to atmospheric pressure, P_{ATM}, and to fix the downstream resistance R_2. The value of R_2 was determined by measuring the pressure drop across it, which was described by R_2Q^2. P_1 and P_2 were free to vary as the flow was varied. The control of flow rate was obtained by varying the upstream resistance R_1, or by altering the height of the inlet reservoir.

Sets of data were recorded for constant values of P_E and R_2. These sets were then grouped into families. The membership of each family was determined by certain relationships of P_E and R_2 e.g. Constant P_E with varying R_2; constant ratio of P_E to R_2; or constant R_2 with varying P_E. Conrad presented his data in a series of

"characteristic curves" or "*P-Q* characteristics" whereby he plotted inlet to outlet pressure difference, $P_1 - P_2$, against flow rate, Q. The basic characteristic curve is shown in Figure 2.2.

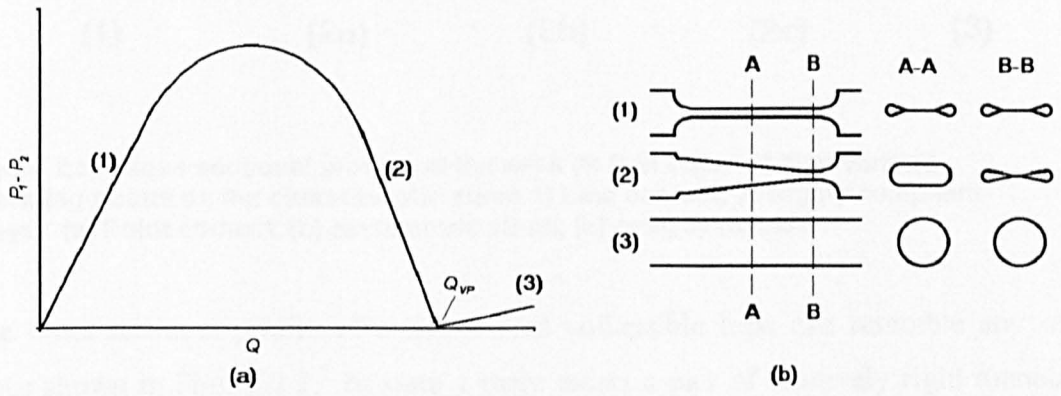

Figure 2.2. The characteristic curve and side profiles resulting from a collapsible tube experiment where external pressure, P_E, is maintained at a constant value above atmospheric pressure. Figure adapted from [10]

Figure 2.2 shows three general flow states for the geometry of a collapsible tube. State 1 corresponds to the values of flow between zero and peak pressure difference; state 2 corresponds to values of flow between peak pressure difference and the "valley point"; and state 3 corresponds to values of flow greater than valley point flow. The valley point, Q_{VP}, is the flow rate at which the transmural pressure first turns negative and a pinch in the tube results. It is the transition between an open and collapsed tube.

State 2 exhibits a convergent-divergent nozzle. The location of this nozzle is the result of a balance of various forces exerted upon the membrane of the tube as well as its material properties. These include forces due to the transmural pressure, fluid wall shear stress, axial, and circumferential tube wall bending stiffness and tube axial tension.

The three general states of Figure 2.2 can be further categorised by viewing the cross-sectional profile at the pinch. The various profiles are shown in Figure 2.3.

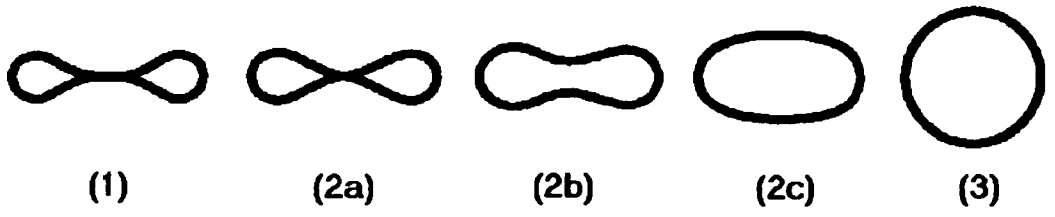

Figure 2.3. Cross sectional profiles at the neck (B-B in Figure 2.2) at various operating points on the characteristic curve 1) Line contact; 2) Highly compliant stages (a) Point contact, (b) asymmetric pinch, (c) oval; 3) Cylinder.

The cross-sectional profile of a thin-walled collapsible tube can resemble any of those shown in Figure 2.3. In state 1 there exists a pair of relatively rigid tunnels separated by a distinct area of line contact. This area of contact decreases axially with increased flow rate until line contact only exists at the downstream end as in Figure 2.3 (2a). As flow is further increased the tube walls at the pinch gradually move further apart and the pinch travels upstream. At flows greater than Q_{VP} the transmural pressure is positive (internal pressure greater than external pressure) and the tube becomes a relatively rigid cylinder due to the radial stresses exerted on it by the fluid pressure difference.

In states 1 and 3 the tube behaves like a Poiseuille resistance whose value in state 1 is much larger than in state 3 because of the difference in effective cross-sectional areas. The variable geometry in states 2(a) to 2(c) reflects the delicate balance between stresses in the wall and the transmural pressure distribution. The changing resistance of the geometry of the tube causes the pressure-flow relationship to be non-linear and it is between these states that instabilities can occur..

Katz et al [11] presented the volume within a collapsible tube as a function of transmural pressure (Figure 2.4) where the rigidity of states 1 and 3 mentioned above is clear since large changes in transmural pressure result in only small changes of volume. States 2(a) to 2(c) show that only small changes in transmural pressure are needed to substantially change the tube volume.

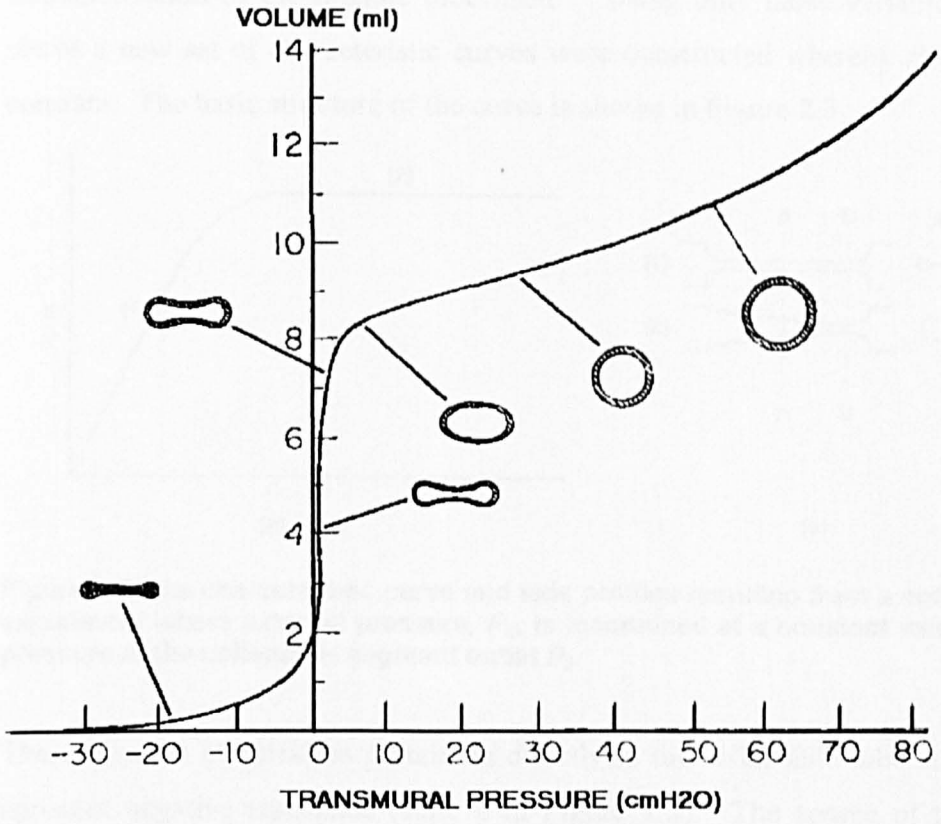

Figure 2.4. Internal volume of a collapsible tube as a function of transmural pressure. Figure from Katz et al [11].

Confusion was documented by Conrad [9] when he plotted on a single graph the experimental pressure flow relationships described in four previous published reports on the collapsible-tube phenomenon by Holt [8], Holt [12], Rodbard [13] and Rodbard and Saiki [14]. Not only did none of the curves coincide, but also there was not even agreement as to the qualitative behaviour of the curves. Brower and Noordergraaf [10] tidied up some of this confusion. They recognised that the collapsible tube was, essentially, "a three-terminal device: inflow pressure at terminal one, outflow pressure at terminal 2, external pressure at terminal 3. Considering average quantities, flow into terminal 3 is zero, and flow into terminal 1 equals the flow out of terminal 2. Since there are three terminals, only two independent pressure differences can be defined. The point is that in the steady state the flexible tube can be experimentally characterised by the quantities flow, Q, and two of the three definable pressure differences, $P_1 - P_2$, $P_E - P_2$ and $P_E - P_1$. The various other quantities such as R_1, R_2, and upstream and downstream reservoir pressures, while perhaps necessary to conduct the experiment, are unessential for the

characterisation of the flexible tube itself." Using only those variables mentioned above a new set of characteristic curves were constructed whereby P_E-P_2 was held constant. The basic structure of the curve is shown in Figure 2.5.

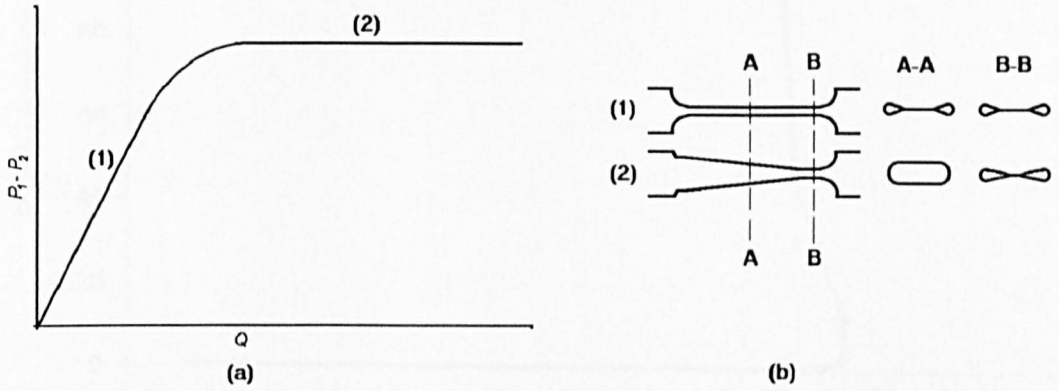

Figure 2.5. The characteristic curve and side profiles resulting from a collapsible tube experiment where external pressure, P_E, is maintained at a constant value above the pressure at the collapsible segment outlet P_2.

The utilisation of variables pertaining directly to the collapsible tube eliminated the apparent negative resistance (state 2 in Figure 2.2). The source of this negative resistance was the downstream resistance, R_2, which becomes more significant as the flow is increased [10].

The curve in Figure 2.5 is unlike that of Figure 2.2, the difference is the relationship which ties the individual points together i.e. Figure 2.2 used $P_E - P_{ATM}$ = constant and Figure 2.5 used $P_E - P_2$ = constant. The shape of the characteristic curve depends entirely on how the experiment is conducted and how data is grouped together. Figure 2.5 exhibits pressure-drop limitation, whatever the value of Q the same pressure difference $P_1 - P_2$ exists for a constant value of $P_E - P_2$. The characteristic curve that results when $P_E - P_1$ = constant can be seen by using the data from table 1(a) in Holt [8]. This is shown in Figure 2.6.

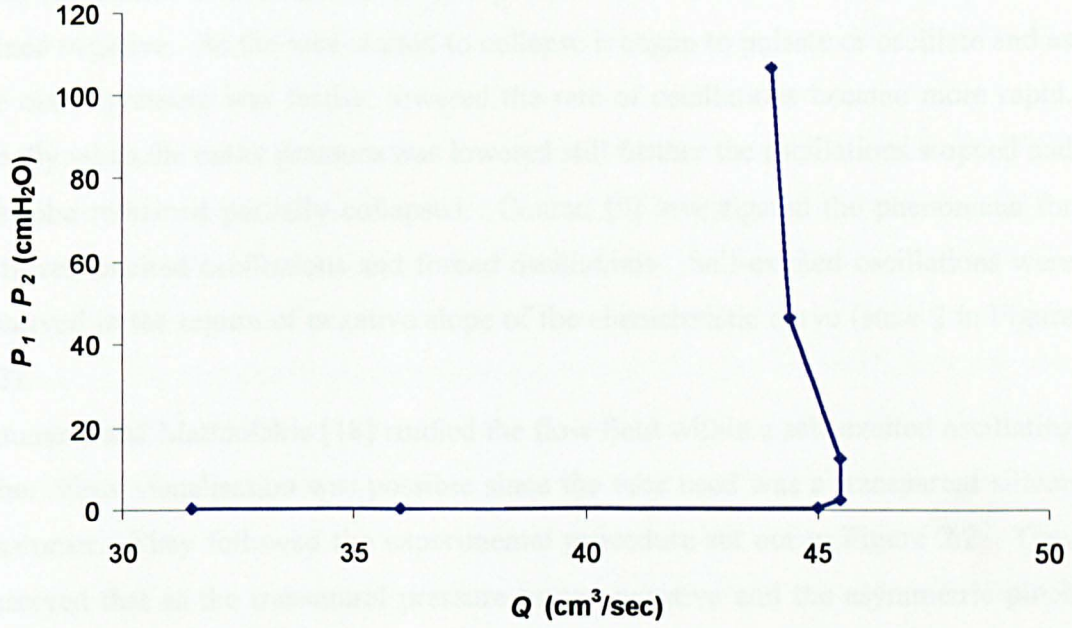

Figure 2.6. Characteristic curve constructed from Holt [8] table 1(a) where external pressure, P_E, is maintained at a constant value above collapsible tube inlet pressure P_1.

Holt observed that, with a constant $P_E - P_1$ and partially collapsed tube, the flow rate did not increase as the outlet pressure was decreased (thus increasing the pressure drop across the collapsible segment) and concluded that there was a higher resistance to flow as the outlet pressure decreased. Figure 2.6 exhibits flow-rate limitation, however much the pressure difference $P_1 - P_2$ increases the flow-rate remains relatively constant.

2.1.3 Unsteady Flow (Self-Excited Oscillations)

A phenomenon that renders the collapsible tube models more complicated is self-excited oscillations. In steady-state tube response the shape of the tube can be characterised by some measured parameters local to the tube. Where oscillations are present the experimental set-up as a whole is of importance.

The physical mechanisms responsible for the onset of collapsible tube oscillations are not yet fully understood but various researchers have deduced that energy loss by flow separation [15], variation in longitudinal wall tension [16] and propagation of fluid-elastic pressure waves [17] may be important.

Holt [8] observed oscillations in collapsible tubes when the transmural pressure turned negative. As the tube started to collapse it began to pulsate or oscillate and as the outlet pressure was further lowered the rate of oscillations became more rapid. Finally when the outlet pressure was lowered still further the oscillations stopped and the tube remained partially collapsed. Conrad [9] investigated the phenomena for both self-excited oscillations and forced oscillations. Self-excited oscillations were observed in the region of negative slope of the characteristic curve (state 2 in Figure 2.2).

Kounanis and Mathiolakis [18] studied the flow field within a self-excited oscillating tube. Flow visualisation was possible since the tube used was a transparent silicon elastomer. They followed the experimental procedure set out in Figure 2.2. They observed that as the transmural pressure turned negative and the asymmetric pinch was formed flow separation took place a little downstream of the tube neck so that there was a jet at the tube axis surrounded by stagnant fluid. At an arbitrary instant, without changing the flow conditions, the flow became attached at the upper wall of the nozzle and separated in the remaining part of the cross-section. When this asymmetry occurred, oscillations started.

2.1.3.1 Onset Of Oscillations

For a given tube there is a critical flow, characteristic only of the collapsible tube, which determines when oscillations are initiated. Brower and Scholten [17] presented results showing that the onset of oscillations in collapsible vessels can be associated with the fluid velocity approaching the phase velocity in a narrowed segment of the vessel. Brower and Scholten experimentally determined the phase velocity of a tube for a range of transmural pressures by measuring the speed of pressure signals along the tube. They found that as transmural pressure is reduced from a positive value the phase velocity drops to a minimum at approximately zero transmural pressure. As the transmural pressure is further reduced into negative values the phase velocity appears to increase linearly with transmural pressure (this was not confirmed for transmural pressures less than 4 cmH_2O). Another consequence of lowering transmural pressure is that the tube cross-sectional area reduces resulting in a higher local fluid velocity. This data suggested that the potential existed for the fluid velocity to approach the phase velocity. This theory was given weight by the observation that, in a collapsible tube experiment,

oscillations began roughly when fluid velocity exceeded the experimentally predicted phase velocity. The onset of unsteady behaviour in this case was analogous to the choking of sonic gas in a nozzle.

Pedley [16] theoretically investigated the fact that the longitudinal tension in the tube wall decreases with distance downstream as a consequence of the viscous shear stress exerted by the fluid. That is, for elements of the wall to remain in equilibrium the longitudinal tension must decrease with distance downstream. For a given value of tension at the upstream end of the tube the tension may fall to zero before the end of the tube if it were long enough or the initial tension small enough and the flow rate high enough. If this happened the wall would be extremely flexible and unsteady motion would then ensue; thus the prediction of zero longitudinal tension is assumed to correspond to the breakdown of steady flow. Therefore, increasing the initial tension in the tube results in a larger maximum flow rate before the onset of oscillations.

2.1.3.2 Frequency And Waveform Of Oscillations

Bertram's exhaustive analysis of collapsible tube oscillations [15, 19, 20, 21 and 22] has determined that the site of maximum oscillation amplitude is the tube throat and that the time-varying downstream pressure is far from sinusoidal, featuring a brief large negative-going spike once per cycle. Bertram also determined that the oscillation frequency is inversely related to the downstream resistance R_2.

Bertram investigated oscillation frequencies and waveforms in a thick-walled collapsible tube model. The use of a thick-walled tube tended to minimise the effects of the attachment of the tube to the rigid sections. Early observations [15] showed that the collapsible tube could exhibit two different modes of oscillation. Low frequencies were the result of a 'milking' action in which the local flattening developed in the upstream half of the tube and moved to the downstream end. High frequencies occurred when the tube formed a neck, at the downstream end, which vibrated laterally.

In later experiments [19] compound oscillations were observed where rapid oscillation existed within a lower frequency oscillatory cycle. 'Two out of three beats' oscillations were also observed. These were stable intermediate states that existed between two main oscillatory modes. When external pressure was increased the third beat would join in resulting in a conventional oscillation.

Bertram depicted the various modes of oscillation as closed regions in a space defined by $P_E - P_2$ and P_1 [22]. Within each region the oscillation frequency is a weakly increasing function of both $P_E - P_2$ and P_1 but across the boundaries the frequency and wave shapes may change abruptly. A probable topology for the abrupt changes of mode was suggested by Bertram and is shown in Figure 2.7. The axes are abstract but can be approximately identified with P_E and cross-sectional area, A.

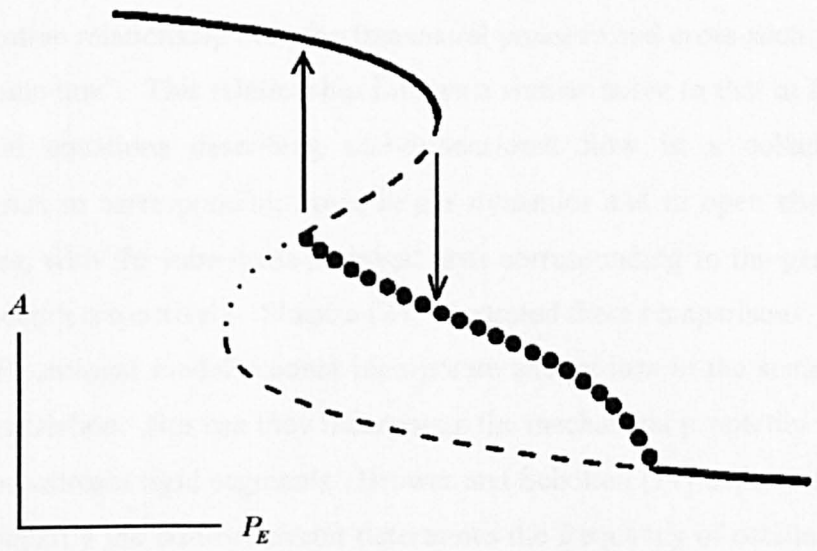

Figure 2.7. Probable topology for the abrupt changes of mode of collapsible tube oscillations. Taken from [22]

Starting at the top left and increasing P_E, the stable equilibrium at values of A of just less than 1 eventually disappears by folding under, leaving the oscillatory path as the only stable one. If P_E is subsequently reduced, the oscillatory path is followed until it meets the folded-under part of the S where it disappears in a bifurcation known as a 'blue-sky catastrophe'.

2.1.3.3 Theoretical Methods For The Prediction Of The Breakdown Of Steady Flow

Many authors have attempted the theoretical explanation of the breakdown of steady flow and self-excited oscillations of the collapsible tube model. The wealth of literature for which is just as voluminous as for the experimental work. Theoretical explanations of the collapsible tube model can be split into two general groups: lumped parameter models or one-dimensional models.

One-dimensional theory is based on the experimental observation that the onset of oscillations in a collapsible tube appears to occur only if the fluid velocity in the tube exceeds the phase velocity of the tube. Cancelli and Pedley [23] describe this phenomenon. They deduced that steady flow is impossible if flow velocity equals phase velocity anywhere; if that happens, the mathematical model must have broken down, and either unsteadiness develops or other neglected physical factors in the model become important.

In a one-dimensional model the elastic properties of the tube are represented by a constitutive relationship between transmural pressure and cross-sectional area known as a "tube law". This relationship follows a similar curve to that in Figure 2.4. The physical equations describing one-dimensional flow in a collapsible tube are analogous to corresponding flows in gas dynamics and in open channels with free surfaces, with the tube cross-sectional area corresponding to the gas density or the liquid depth respectively. Shapiro [24] illustrated these comparisons.

One-dimensional models cannot incorporate energy loss in the separated flow after the constriction. Nor can they incorporate the mechanical properties of the upstream and downstream rigid segments. Brower and Scholten [17] experimentally observed that primarily the outflow circuit determines the frequency of oscillation. However, the flow rate at which the oscillations start is independent of the other circuit elements. This means that although the one-dimensional model can predict the onset of unsteady behaviour at a particular point in the tube it cannot model the ensuing oscillations since frequency of these oscillations is determined, principally, by the outflow circuit. Examples of one-dimensional analysis of the collapsible tube model can be found in [17, 25 and 26].

The theoretical modelling of the collapsible tube system, including upstream and downstream rigid sections has been achieved using lumped-parameter models [e.g. 9, 11 and 15]. Lumped parameter models are those in which the geometry of the collapsible tube is represented by one or two time-dependent variables such as the cross-sectional area at the narrowest point. The elastic properties of the tube are represented by a single-valued relationship between cross-sectional area and the transmural pressure at the narrowest point. Conservation of fluid mass and momentum or energy are represented by integral forms of the governing equations. Lumped parameter models are valid for both steady state and oscillatory response but cannot incorporate wave propagation and choking mechanisms and therefore cannot

distinguish between subcritical and supercritical flow. The absence of choking makes them a fairly crude method. However, the modelling of the upstream and downstream sections of the system allow for the analysis of the unsteady pressure loss at the throat and subsequent pressure recovery. Bertram and Pedley [15] determined that an important factor in the predicted oscillations is the unsteady pressure loss at the throat and subsequent recovery. If no energy is lost, exponential collapse to zero cross-sectional area is predicted, with no oscillations. If all the excess kinetic energy is lost, so that there is no pressure recovery downstream, steady flow is always possible and there are no oscillations; only if some energy loss and some pressure recovery are allowed are oscillations predicted.

2.1.4 Finite Element Investigations Of Collapsible Tubes

The modelling of the collapsible-tube phenomenon using finite element codes can be defined as a separate topic from the theoretical predictions already considered since the tube shape and stresses within its walls are included in the results.

The steady-response collapsible-tube phenomenon has been modelled two-dimensionally by Rast [27]. The geometry considered by Rast involved a section of an otherwise rigid channel being replaced by a thin-walled membrane. The governing equations of the fluid were the two-dimensional Navier-Stokes equations in an adaptive finite element mesh (see section 3.1.3). These were simultaneously solved with the elastic membrane equations for the structure. Luo and Pedley [28] carried out similar work when they used the commercially available finite element code FIDAP for steady flow in a two-dimensional collapsible channel. This work was complemented by the independent development of a time-dependent simulation of the coupled flow-membrane problem, using the Spine method to treat the moving boundary and a second-order time-integration scheme [29] with which oscillations of the tube geometry were observed. A disadvantage of using a deforming mesh to represent the fluid was found to occur when the tube wall was sucked under the rigid wall. This movement caused the elements to deform to such an extent that the numerical scheme broke down.

Heil [30] successfully attempted the three-dimensional modelling of a collapsible tube when he coupled non-linear shell theory with the three-dimensional Stokes equations to analyse the slow viscous flow through a compliant tube. His results illustrated the fluid flow field in the tube and the tube deformation for several sets of

boundary conditions. Good comparison was drawn with Stokes' flow experiments that involved the passing of high-viscosity silicon oil through a thick-walled compliant tube. The limitation of Heil's numerical model was the fact that only very low Reynolds number flows could be analysed. Also, it could not be advanced in the time domain.

2.2 Finite Element Modelling of FSI Systems

There are a rich variety of other applications where fluids interact with structures and finite element modelling (or similar) has been attempted. The relevant literature is reviewed here.

2.2.1 Viscous Fluid Interacting With Flexible Structures

The FSI applications given here are relevant to this project since they represent the progression of numerical modelling for FSI applications involving flexible structures and flowing fluids. The lack of any experimentally validated models of this type of FSI highlights a major boundary of knowledge in this field.

Bathe et al [31] used the commercially available finite element software ADINA to analyse some example cases of FSI including a flow distributor, air compressor and a shock absorber. The solid structure was mathematically modelled using Lagrangian formulations whereas the fluid was modelled using an ALE formulation of the Navier-Stokes equations [32]. The fluid was coupled to the structure by satisfying the kinematic and equilibrium conditions between the fluid and the structural parts at the fluid-structure interfaces. This formulation allowed the fluid mesh to deform at the fluid-structure interface in a Lagrangian manner while allowing fluid to flow through the elements in an Eulerian manner (see appendix H.1).

In the case of the flow distributor the deformations of the structure were small, but the fluid pressures exerted considerable forces on the structure. ADINA computed flow rates in various parts of the device, the pressure and viscous stresses in the fluid and the stress distributions in the structure, all in one analysis run.

The analysis of the air compressor raised an interesting problem regarding the implicit method. The air compressor consisted of a rigid outer structure with an inlet valve modelled as the only flexible structure. The valve was initially closed but opened as a piston moved up and then closed again as the piston returned to its original position. Because of the implicit time-stepping used by ADINA the valve

closure was only detected after the valve had already overshot the closed-condition by a significant margin. This was due to the large size of the implicit time-step. This problem highlighted the inaccuracies of the implicit method when used to solve rapid events. In order to solve the problem the time-step would need to be reduced which, in turn, would vastly increase the CPU cost of a solution. The explicit method would then become the more attractive option due to its fine resolution in the time domain.

Tang et al [33] used ADINA to model wall stress and strain with FSI for blood flow in stenotic arteries although, again, the deformations of the structure were not large.

Bathe and Kamm [34] produced a similar model for pulsatile flow through a stenotic artery although this was a two-dimensional discretization.

Wang [35] adopted a mixed upwinding procedure and the ALE description (similar to the ADINA technique given above) to model the viscous Navier-Stokes flow of fluid past a simple hyperelastic solid. This two-dimensional model involved fluid flow passing over the surface of a slender structure that introduced both normal (pressure) and tangential (shear) stresses. The model demonstrated relatively large fluid-structure interfacial motions and large structural strains. The deformation and the motion of the structure altered the flow domain, which in turn changed the stresses exerted on the structure.

Peskin and McQueen [36] used the immersed boundary method to computationally model the mammalian heart and its valves. York et al [37] used a similar method (Material Point Method (MPM)) for the Fluid-Membrane interaction of airbags. The essence of these FSI techniques required that the structure be treated as part of the fluid in which additional forces (arising from the elastic stress) were applied. This was done using unconnected Lagrangian material points to discretize a membrane within an Eulerian (fluid) mesh in a similar way to that described in section 4.1.5.

2.2.2 Other Examples of FSI

This research was mainly concerned with the transient analysis of flexible structures and viscous fluids. However, a more general appreciation of previous work in numerical FSI was desirable. Fluid-structure interaction can be divided into several categories and sub categories although most of these are not directly related to this particular project. For this reason a detailed review of such work is not given but some examples are listed below.

In FSI models where compressibility is of importance and the fluid-particle motions are so small that any viscous stresses can be assumed negligible, the acoustic fluid is used. The acoustic fluid only transmits pressure waves. Applications of acoustic-fluid-structure interactions are found whenever the fluid undergoes only relatively small particle motions. The area of interest in such problems is usually the pressure, density and temperature of the fluid and its effect on the stability or integrity of the structure [e.g. 38, 39].

In some cases the displacement of a structure and the effect this has on the fluid flow may be analysed with no need to model structural stresses or deformation i.e. the structure is assumed to be movable but rigid. These are called moving boundary models. A typical example is the oscillation of a rigid cylinder in a fluid flow [e.g. 40, 41].

The coupling of two different solution techniques or indeed two different pieces of existing software has been attempted using a staggered scheme. A staggered scheme simply solves for one time-step of the fluid while the structural solution is halted and then this situation is reversed to solve for the structure [e.g. 42, 43, 44, 45, 46]. Problems found with this method include the presence of a time lag between the fluid and the structural responses.

3 Numerical Formulations for Fluid-Structure Interaction

There remains a fundamental difference in the way fluids and structures have been analysed computationally over the years. The mechanical principles governing fluids and solids are the same but they are separated by the different response characteristics that result in different solution difficulties. In both fields the component, or area of study, is split up (discretized) into simple elements in which the governing equations may be solved e.g. the finite element or finite difference method. These elements are connected together at their common nodes. In this research the finite element method was used. A detailed description of this method is beyond the scope of this thesis. Essentially the finite element method uses matrices to categorise the behaviour of each element in terms of the element's material and geometric properties, the distribution of loading within the element and the loads and displacements at the nodes of the element. The finite element method is described in detail by Bathe [47].

In a structural finite element (FE) analysis (e.g. ANSYS, LS-DYNA) the computational mesh is normally embedded in the structure and therefore moves with it (Lagrangian technique). General-purpose computational fluid dynamics (CFD) codes (e.g. FLUENT, STAR-CD, ADINA-F) tend to use an Eulerian grid where the computational mesh of elements is fixed in space and the fluid moves from one cell to another. The techniques for solving the governing equations of transient CFD and structural analyses can be further split into one or the other of two different general time-stepping approaches, an implicit approach or an explicit approach (see sections 3.2.1 and 3.2.2).

The tool used to create numerical FSI models must be capable of merging the two disciplines of solid/structural analysis and numerical fluid analysis. The fundamental differences between structural and fluid analyses are the main reason that a fully developed general-purpose FSI code has not materialised. However, the trend in engineering analysis, in recent years, has been towards "multiple physics". That is the simulation of a range of factors in a single system. Some of the big names in engineering analysis, such as ANSYS and MSC, have been making themselves bigger by buying up smaller specialist firms with strength in particular areas.

Therefore FSI facilities exist in several different analysis codes (ADINA, MSC.DYTRAN, LS-DYNA, FIDAP) but are still very much in their infancy.
The methods of FSI coupling are dependent on the particular code being used. However, the formulation of the fluid and the structural elements and the technique for advancing the solution in time can be generally defined.

3.1 Element Formulations

3.1.1 Lagrangian Formulation

In Lagrangian simulations, the computational mesh of finite elements is fixed to the fluid or structure and therefore moves with the local fluid/structural velocity. There is no movement of matter through the mesh. Therefore Lagrangian methods are well suited to maintaining material interfaces. In a fluid analysis the Lagrangian technique is generally limited to small displacement problems such as sloshing, as the representation of large deformations is hindered by shear and vorticity which tends to tangle the mesh.
In a Lagrangian time-step the solution is advanced in time from t_n to time t_{n+1}. The mesh is subjected to boundary and initial conditions and the movement or deformation of the mesh is dependent on these as well as the defined material properties and governing conservative equations. At the end of the time-step new boundary conditions are present on the element edges and time is then advanced from t_{n+1} to t_{n+2}.
A typical explicit (see section 3.2.2) Lagrangian time-step proceeds as follows [48]:

1) Knowing the stress, pressure, hourglass forces, etc. at time t_n in each element, the forces in the nodes are calculated. The accelerations of the nodes are calculated using f = ma since mass is known.
2) The accelerations are integrated to give the velocity at time $t_{n+1/2}$.
3) The velocity is integrated to give the displacement at time t_{n+1}
4) The constitutive model for the strength of the material is integrated from t_n to t_{n+1} now that the motion of the material is known.
5) The artificial shock viscosity and hourglass viscosity are calculated (see section 4.1.6)
6) The internal energy is updated based on the work done between t_n and t_{n+1}.

7) Based on the density and energy at t_{n+1}, the pressure is calculated from the equation of state (see section 4.1.2).
8) A new time step size is calculated based on the speed of sound through each of the elements and their geometry.
9) Advance the time and return to step (1)

To minimise the storage required, the solution is stored for only one time t_n within the program. At the completion of a time-step, the solution at the beginning of the time-step is overwritten by the solution at the end of the time-step.

3.1.2 Eulerian Formulation

At some point in a calculation involving 'flowing' fluids a Lagrangian mesh would become excessively distorted. In Eulerian simulations, the mesh is fixed in space and the fluid moves from one cell to another thus avoiding any distortion. However, Eulerian codes are not as accurate at tracking the transport of material as it flows through the mesh.

There are two schools of thought on how Eulerian codes should be structured. One approach updates the solution variables in a single step. The other separates the Lagrangian and Eulerian terms into two distinct steps. The latter is considered here. A Lagrangian step is performed first which allows the mesh to follow the material and distort. The solution on the distorted mesh is mapped back onto the original, spatially fixed, Eulerian mesh in a separate step referred to as a 'remap' or 'advection' step. This strategy is referred to as an 'operator split' since the Eulerian and Lagrangian operations are separated. There is no time-step associated with the Eulerian step; it is simply a projection of the solution from one mesh onto another. Time evolves only during the Lagrangian step.

In the area of fluids, both the Lagrangian and Eulerian descriptions have been employed; the Lagrangian seems to be preferred for 'contained fluids' in which there is only small motion. The Eulerian is preferred for any flow in which the mesh would be highly contorted if required to follow the motion such is the case with most 'flowing' fluid problems. Both formulations are depicted in Figure 3.1 for a simple two-dimensional mesh subjected to a positive pressure on the left-hand edge and fully constrained on the top and bottom edges.

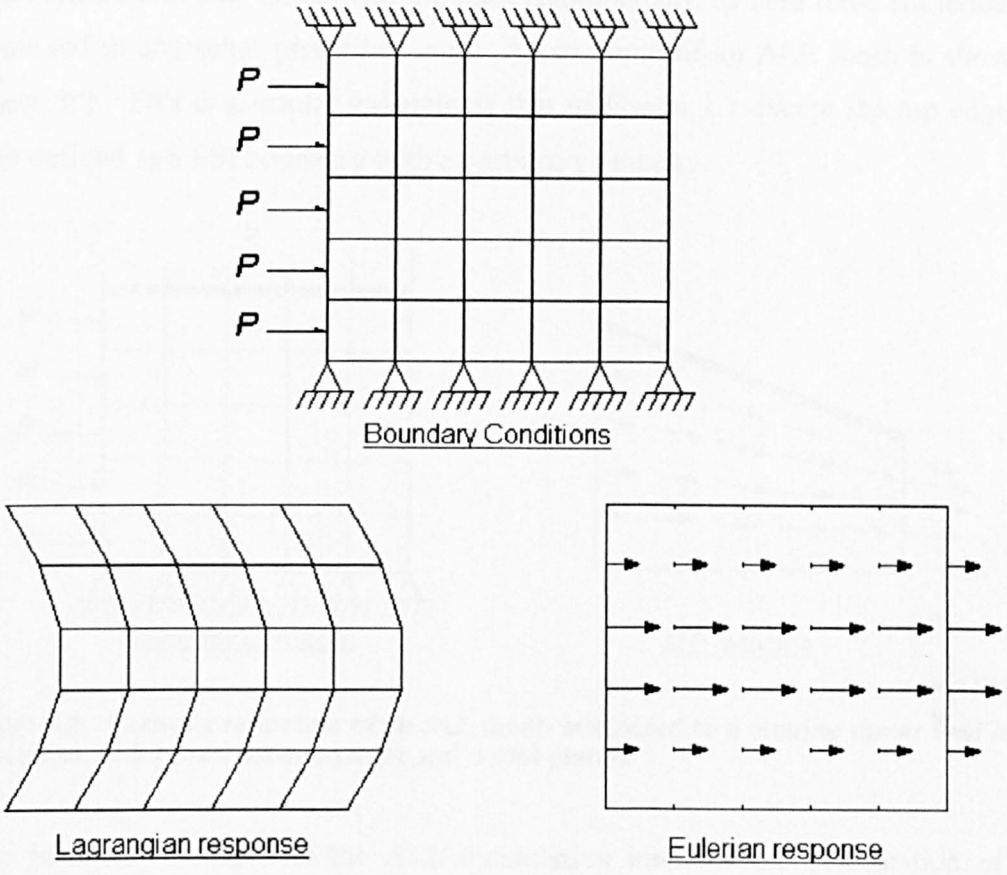

Figure 3.1. Response of Lagrangian and Eulerian meshes subjected to the same boundary conditions.

3.1.3 Arbitrary Lagrangian-Eulerian Formulation

For many free surface flows, and problems of fluid-structure interaction, it is necessary to have a more versatile description of the fluid domain. This has been achieved in the arbitrary Lagrangian-Eulerian (ALE) formulation. The ALE technique is a relatively new tool and has, so far, mainly been used in crash analysis and metal forming [49].

The ALE formulation was first published in 1974 by Hirt et al [50] where a technique was presented for the solution of the Navier-Stokes equations that was both Lagrangian and Eulerian, and that was applicable to flows at all speeds.

The Lagrangian and Eulerian representations are only two special cases of mesh motion; the essence of the ALE idea is that the mesh motion can be chosen arbitrarily, providing additional flexibility and accuracy. The method uses a mesh

with vertices that may move with the fluid (Lagrangian), be held fixed (Eulerian), or be moved in any other prescribed way. An example of an ALE mesh is shown in Figure 3.2. This is a similar example as that of Figure 3.1 except the top edge has been defined as a FSI boundary with an arbitrary velocity.

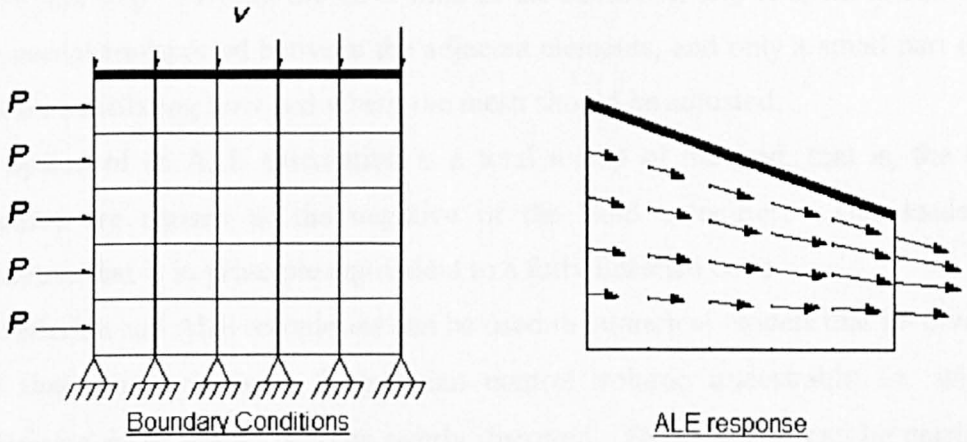

Figure 3.2. Example response of an ALE mesh subjected to a moving upper wall and a pressure difference between inlet and outlet planes.

This particular example of the ALE formulation involves the deformation of the mesh with the moving boundary while fluid flows through it in an Eulerian fashion. A mesh-smoothing algorithm must be used in order to spread the deformation from the top edge throughout the mesh; otherwise the top row of elements would become overly distorted.

ALE formulations may be thought of as algorithms that perform automatic remapping of the mesh. An ALE formulation, like the Eulerian 'operator split' formulation, consists of a Lagrangian time-step followed by a "remap" or "advection" step. The factors that distinguish an ALE formulation from an Eulerian formulation are the frequency of remapping and the restrictions placed on the remap strategy. An Eulerian advection must map the solution onto the original mesh after each time-step. An ALE advection may map the solution onto an arbitrarily defined mesh and is not constrained to do so in each time-step.

The overall flow of an ALE time step is [49]

1) Perform a Lagrangian time step (see section 3.1.1).
2) Perform an advection step
   a) Decide which nodes to move
   b) Move the boundary nodes

c) Move the interior nodes

d) Calculate the transport of the element-centred variables

e) Calculate the momentum transport and update the velocity

The cost of the advection step per element is usually much larger than the cost of the Lagrangian step. Most of the CPU time in the advection step is spent in calculating the material transported between the adjacent elements, and only a small part of it is spent on calculating how and where the mesh should be adjusted.

One option of an ALE calculation is a total remap of the grid; that is, the remap velocities are chosen as the negative of the fluid velocities. This leads to a simulation that is in principle equivalent to a fully Eulerian code.

The Eulerian and ALE techniques can be used in numerical models that involve fluid flow that would render a Lagrangian control volume undesirable i.e. where a Lagrangian mesh would become overly distorted. FSI coupling can be carried out between the Eulerian/ALE fluid and a Lagrangian structure. Such couplings are described in section 4.1.5 and in appendix H.1.

The use of the ALE method described above deals with fluids and FSI. However, ALE can also be used in structural analyses where there is large displacement which could cause tangling of the mesh if a purely Lagrangian method were used such as in metal forming or crash simulation.

3.2 Time Integration

The advancement of the finite element solution in the time domain can be performed using either of the two general approaches, the implicit or explicit approach.

3.2.1 Implicit Method

An implicit analysis is the basis of conventional static analysis (e.g. ANSYS, MSC.NASTRAN) where the assembly and inversion of a stiffness matrix is required to solve static systems. Since the 70's an implicit time-stepping formulation has been available to solve dynamic systems. The Newmark family of time integration schemes is normally implemented in the commercial codes to advance the solution in time.

Considering an element as a spring-mass-damper system. If the current time-step is step t_n, then a good estimate of the acceleration at the end of step t_{n+1} will satisfy equation 1 [51]:

$$Ma'_{n+1} + Cv'_{n+1} + Kd'_{n+1} = F^{ext}{}_{n+1} \quad (1)$$

where M = mass matrix of the structure, C = damping matrix of the structure, K = stiffness matrix of the structure, F^{ext} = vector of externally applied loads, a'_{n+1} = estimate of acceleration at step t_{n+1}, v'_{n+1} = estimate of velocity at step t_{n+1}, d'_{n+1} = estimate of displacement at step t_{n+1}, and the prime denotes an estimated value.

The estimates of displacement and velocity are given by [51]:

$$d'_{n+1} = d_n + v_n \Delta t + \frac{((1-2\beta)a_n \Delta t^2)}{2} + \beta a'_{n+1} \Delta t^2 \quad (2)$$

or

$$d'_{n+1} = d^{\times}{}_n + \beta a'_{n+1} \Delta t^2 \quad (3)$$

$$v'_{n+1} = v^{\times}{}_n + \gamma a'_{n+1} \Delta t \quad (4)$$

or

$$v'_{n+1} = v_n + (1-\gamma)a_n \Delta t + \gamma a'_{n+1} \Delta t \quad (5)$$

where Δt is the time-step and β and γ are constants.

The terms $d^{\times}{}_n$ and $v^{\times}{}_n$ are predictive and are based on values that are already calculated.

Substituting these values in the equation of motion results in

$$Ma'_{n+1} + C(v^{\times}{}_n + \gamma a'_{n+1} \Delta t) + K(d^{\times}{}_n + \beta a'_{n+1} \Delta t^2) = F^{ext}{}_{n+1} \quad (6)$$

or

$$\left[M + C\gamma \Delta t + K\beta \Delta t^2\right] a'_{n+1} = F^{ext}{}_{n+1} - Cv^{\times}{}_n - Kd^{\times}{}_n \quad (7)$$

The equation of motion may then be defined as

$$M^{\times} a'_{n+1} = F^{residual}{}_{n+1} \quad (8)$$

The accelerations are obtained by inverting the $M^{\times}$ matrix as follows:

$$a'_{n+1} = M^{-1} F^{residual}{}_{n+1} \tag{9}$$

This is analogous to decomposing the stiffness matrix in a linear static analysis. However, the dynamics mean that mass and damping terms are also present.

Most implicit time integration based solvers use an automatic time-stepping scheme. The time-step is increased when the response varies smoothly and decreased when sudden changes in global stiffness occur.

3.2.2 Explicit Method

The origins of the technology date back to the mid-70's and early 80's where explicit analysis codes were developed at the US Government Defence Laboratories. A leading pioneer was Dr John Hallquist, based at Lawrence Livermore National Laboratories, where the explicit code DYNA3D was placed in the public domain and made globally available.

The explicit analysis code is an important design tool for the assessment of structures and components undergoing sudden and rapid loading and is briefly described below [49, 51] and described in more detail by Benson [48].

Considering an element as a spring-mass-damper system the equation of motion at time-step t_n may be written

$$Ma_n + Cv_n + Kd_n = F^{ext}{}_n \tag{10}$$

where M is the diagonal mass matrix, a is the acceleration vector, C is the damping coefficient, v is velocity vector, K is the linear stiffness, d is the displacement vector and F^{ext} is the vector of externally applied loads. Simplifying $F^{ext}{}_n - (Cv_n + Kd_n) = F^{residual}{}_n$ means equation (10) can be rewritten as

$$a_n = M^{-1} F^{residual}{}_n \tag{11}$$

The acceleration can be found by inverting the diagonal mass matrix and multiplying it by the residual load vector. The matrix equation now corresponds to a set of independent equations for each degree of freedom as follows:

$$a_{ni} = \frac{F^{residual}{}_{ni}}{M} \tag{12}$$

The solution is now advanced in the time domain to t_{n+1} using the central difference scheme [48]. To have an algorithm with second order accuracy in time, the velocity must be staggered with respect to the displacement. The nodal velocity (v) and displacement (d) are simply calculated from known values on the right-hand side of the following equations:

$$v_{n+1/2} = v_{n-1/2} + a_n \Delta t_n \tag{13}$$

$$d_{n+1} = d_n + v_{n+1/2} \Delta t_{n+1/2} \tag{14}$$

where

$$\Delta t_{n+1/2} = \frac{(\Delta t_n + \Delta t_{n+1})}{2} \tag{15}$$

This assumes that the acceleration is constant over the time-step. The geometry of the mesh is then updated by adding the displacement increments to the initial geometry

Explicit methods do not require matrix decompositions or matrix solutions. Instead, the loop is carried out for each time-step. A typical example of an explicit Lagrangian time-step for a transient analysis is given in section 3.1.1.

3.2.3 Implicit Verses Explicit Methodologies

The inversion of the stiffness matrix in the implicit approach is more demanding both in terms of CPU time and data storage on computer resources than the explicit approach. The advantage of this approach is that stability can be maintained for much larger time-step values than for a corresponding explicit analysis. Some implicit methods are unconditionally stable, which means no matter how large the time-step a stable solution will be reached. This makes implicit methods more attractive for transient events that occur over a long time period and are dominated by low-frequency structural dynamics.

For explicit codes to remain stable the time-step must be governed by a stability criterion such as the Courant limit (see section 4.1.3) which can be generally described as the time taken for a shock wave to travel across the smallest element in the mesh. If the time-step is taken as a value larger than this the model will go

unstable and the solution would crash due to such things as numbers going to infinity or taking the square root of a negative number. However, since each iteration does not involve the costly formulation and decomposition of matrices, explicit techniques are still very competitive with implicit methods.

The small time-step of an explicit analysis can be advantageous since high resolution in the time domain can be important in accurately capturing the non-linear behaviour of a system. This could be material non-linearity, geometric non-linearity (such as contact and friction) or material and geometric non-linearity in combination with large displacements. The small time-step size effectively allows the development of numerical techniques that linearise the non-linear behaviour allowing a non-iterative solution. Consequently, there is negligible computational overhead for non-linear behaviour. In an implicit analysis the convergence becomes more difficult to achieve as the amount of non-linearity increases.

A small time-step is also an advantage when stress waves are significant and in models involving contact surfaces, the small amount of nodal penetration that occurs in a single time-step allows simple repositioning of the contact node back to the physical surface.

Explicit methods have increasing advantages over implicit methods as the model gets bigger. A geometrically small component would not be suited to the explicit technique since very small elements produce very small time-steps. However, small components can be modelled explicitly if a suitable speed-up technique is used.

The increase in computing power, software technology and the advent of massively parallel processor (MPP) machines has expanded the application of explicit methods for the analysis of large models and for longer duration events. Explicit analysis software has been designed to take full advantage of multiprocessor machines.

Implicit methods have also benefited from advances in computer technology for the solution of large global structural matrices. In-core and parallel sparse solvers and multi-frontal solvers have been facilitated by increases in computer memory and the advent of multiple processors.

In general the mathematical formulation of the two approaches and limited computing power continued to restrict their uses to two classes of problems. The explicit approach can be well employed for short-duration extreme loading events such as crash analysis and the implicit approach for longer-duration vibration events

such as the simulation of fatigue-testing procedures. Examples are given in Table 3.1.

	EXPLICIT	IMPLICIT
GEOMETRY	System models, interacting components	Monolithic structures
MATERIAL	Highly non-linear material	Mildly non-linear material
LOADING REGIME	Short duration	Long duration, Vibration
BOUNDARY CONDITIONS	Component contact, Self contact, Automatic contact	Small displacement contact

Table 3.1 Comparison of the explicit and Implicit Time Integration Techniques for the Solution of Finite Element Models. Table adapted from [52].

CFD codes are generally advanced in time implicitly since many flow models require a fine mesh resolution such as in the calculation of high Reynolds number viscous flows, where extreme changes in the flow field occur close to a surface.

Structural finite element codes can be either implicit (ANSYS, ADINA) or explicit (DYNA, MSC.DYTRAN). Indeed, some software houses offer both time-integration techniques within a single code.

3.3 Selection Of An FSI Technique

Several questions must be asked of the particular model of study before a suitable technique is chosen. These questions should be "Does the fluid flow or is it contained? Is viscosity significant? Are shock waves important in both fluid and structure? Can the fluid be regarded as incompressible? Is turbulence of interest? Is material non-linearity significant?" Broadly speaking the answers to the above questions will determine the resolution required in the time domain and the method of material motion.

For the purposes of this study the previous work of Patterson et al [4] and Carmody et al [5], from which this research stems, should be considered. Patterson et al looked at the 'dry' analysis of heart valves as they advanced through the cardiac cycle. 'Dry' meaning that there was no FSI and the valves were moved using time-varying pressure loads applied to the faces of the Lagrangian mesh. Carmody et al

took the heart-valve model a stage further by introducing an Eulerian fluid control volume to model the blood flow. In this case the valves were moved by applying time-varying loads to reservoirs at either end of the Eulerian control volume. This analysis of flexible structures undergoing large deformations coupled with 'flowing' fluids is definitive of FSI for this particular project and is inherent in the collapsible tube phenomenon. The Lagrangian formulation can be assumed for the structures and for the fluid there is a choice of the Eulerian or ALE formulations.

Heart valves and collapsible tubes may be regarded as small complex components and as such are not ideally suited to the explicit approach. Also, due to the compliance of the structure, the compressibility of the fluid and the effect of shock waves can, for most purposes, be neglected. However, the non-linear nature of the system, the large deformation of the structure and short duration of the applied loads or structural response requires that an explicit code be used. The small size of the elements needed for accurate modelling of the component means an unsuitably small time-step may result (particularly in an FSI analysis); therefore a suitable speed-up technique is needed to achieve reasonable CPU times.

4 Analysis Software And Hardware

The explicit finite element analysis code LS-DYNA was used extensively throughout this research. However, the FSI facilities of two other finite element codes were also evaluated over short time periods (one/two months), these were ADINA [53] and MSC.DYTRAN [54]. The findings of these evaluations can be found in appendices G and H. This chapter is entirely devoted to the LS-DYNA code.

4.1 LS-DYNA Technique

LS-DYNA is an explicit three-dimensional finite element code for analysing the large-deformation dynamic response of structures, including structures coupled to fluids. LS-DYNA is produced by Livermore Software Technology Corporation and distributed in the UK by Ove Arup and Partners. Several versions of the code were used for this research from version 945 Fixed Format, at the beginning of the research, through to version 950d Keyword. The analyses presented in this document used version 950d.

This section draws from the LS-DYNA theory manual [49], Benson [48], MSC.DYTRAN theory manual [51] and Souli [55] and describes some of the more important aspects of the code with regard to this research.

4.1.1 Structural Elements

The structural parts were constructed of four-noded Belytschko-Lin-Tsay shells, which included bending and shear deformation. Two through-thickness integration points were deemed sufficient when using linear elastic materials. This is because bending stresses at any point in the thickness of a shell can be interpolated or extrapolated from just two points as long as the response is linear. The shells were treated in much the same way as they would have been in a 'dry' analysis except they were placed within a fluid mesh and coupled to it enabling fluid-structure interaction (see section 4.1.5).

The Belytschko-Lin-Tsay shells use one-point integration in the plane of the shells. To suppress the hourglass deformation modes that accompany one-point integration, hourglass viscosity stresses are added to the physical stresses (see section 4.1.6.2).

The linear elastic material was used in most models where the density (ρ_s), Young's modulus (E) and Poisson's ratio (ν) were defined.

4.1.2 Fluid Elements And The Equation Of State

The fluid elements were constructed using eight-noded solid elements. The one-point-integration Eulerian formulation was used wherever possible. However, when there was a need to model voids in the fluid the one-point-integration-with-void formulation was more desirable.

In fluid dynamics analysis the standard conservative equations of the Eulerian formulation are the Navier-Stokes equations where the conservation of mass, momentum and energy are stated in standard Cartesian notation as [55]:

$$\frac{\partial \rho}{\partial t} = -\rho . div(v) - (v_i - u_i).\frac{\partial \rho}{\partial x_i} \tag{16}$$

$$\rho \frac{\partial v_i}{\partial t} = \sigma_{i,j} - \rho .(v_i - u_i)\frac{\partial v_i}{\partial x_j} \tag{17}$$

$$\rho \frac{\partial e}{\partial t} = \sigma_{ij} . \varepsilon_{ij} - \rho .(v_i - u_i)\frac{\partial e}{\partial x_j} \tag{18}$$

respectively, where v is the fluid velocity and u is the mesh velocity (u = 0 in a standard Eulerian formulation), $\dot{\varepsilon}$ is the strain rate, e is the specific internal energy, σ is the stress tensor, ρ is the fluid mass density.

LS-DYNA uses an operator-split technique (see section 3.1.2) to solve the conservative equations. In the Lagrangian phase the mass equation is automatically satisfied and since $u = v$ the momentum and energy terms become:

$$\rho \frac{\partial v_i}{\partial t} = \sigma_{i,j} \tag{19}$$

$$\rho \frac{\partial e}{\partial t} = \sigma_{ij} . \varepsilon_{ij} \tag{20}$$

The solution is then advected back onto the original mesh. The advection algorithm used in the Eulerian formulation in LS-DYNA was the Doner cell algorithm, which was stable, monotonic (the range of the solution variables does not increase during the advection) and first-order accurate. A second-order accurate algorithm would have allowed the calculations to be performed with far fewer elements but would have been more computationally expensive.

A problem with the Doner cell algorithm is that it is dissipative. This means that material that has just entered an element and should still be near the face is smeared over the whole element. This averaging of the fluid volume meant that a finer mesh than would have been necessary with a second order accurate algorithm needed to be used. However, due to the nature of the LS-DYNA models a fine mesh resolution was often required e.g. where FSI took place. Therefore, this limitation had little effect on CPU cost.

The fluid control volume was split into separate sections. The number of sections depended on the particular model; however, these sections fell into one of two categories: the flow domain or the reservoirs. The reservoirs were constructed from ambient elements that supplied or removed fluid from the flow domain. The main flow domain contained all the structural parts and was used in the FSI coupling.

The fluid properties were defined in a different way from those of structures. In LS-DYNA fluids were defined using a null material where the pressure was calculated using an equation of state to avoid deviatoric stress calculations. A pressure cut-off was specified to set a lower bound on the pressure.

4.1.2.1 Equation Of State

The equation of state used in the FSI analysis was the Gruneisen equation of state [3], which uses a relationship between the shock velocity (v_s), and the particle velocity (v_p) which determines the pressure for compressed materials as:

$$P = \frac{\rho_0 c^2 \theta \left[1 + \left(1 - \frac{\gamma_0}{2}\right)\theta - \frac{h}{2}\theta^2\right]}{\left[1 - (S_1 - 1)\theta - S_2 \frac{\theta^2}{(\theta+1)} - S_3 \frac{\theta^3}{(\theta+1)}\right]^2} + (\gamma_0 + h\theta)e_0 \qquad (21)$$

and for expanded materials as

$$P = \rho_0 c^2 \theta + (\gamma_0 + h\theta) e_0 \qquad (22)$$

where c is the intercept of the v_s-v_p curve; S_1 *(1.979)*, S_2, (0) and S_3 (0) are the coefficients of the slope of the v_s-v_p curve; γ_0 is the Gruneisen gamma (0.11); h (3) is the first order volume correction to γ_0; e_0 is the initial internal energy (0); ρ_0 is the initial density (defined in material); and $\theta = \frac{\rho}{\rho_0} - 1$.

The value of c is therefore the sonic velocity of the fluid at low Mach numbers and required definition for a successful analysis. The other parameters were taken as the values in brackets above on recommendation from LSTC (the programmers of LS-DYNA) for the modelling of water.

4.1.3 Time-Step Control

The CPU cost of an LS-DYNA analysis is controlled by the:

- number of elements in the model
- complexity of the model geometry
- termination time
- time-step

The time-step is the period of time between updates of the model parameters e.g. pressures, velocity, internal energy etc. A small time-step is undesirable since it will result in more cycles through the model before the required termination time is reached. The control of the time-step is, therefore, an effective way of lowering the CPU cost of an analysis.

The time-integration method used in LS-DYNA is the explicit central difference scheme described in section 3.2.2. The time-step size is given by the Courant limit which is the smallest amount of time that is necessary for a sound wave to cross an element in the mesh (this is typical of an explicit method). This number is a function of both the element geometry and the speed of sound within the material.

For the shell elements, the time-step is given by:

$$\Delta t_e = \frac{L_S}{c} \qquad (23)$$

Where L_s is the characteristic length ($\text{characteristic length} = \frac{\text{element area}}{\text{longest side}}$) and c is the speed of sound through the material defined in shell elements as:

$$c = \sqrt{\frac{E}{\rho(1-\nu^2)}} \tag{24}$$

where E is the Young's Modulus, ρ is the density and ν is Poisson's ratio.

It can be seen from the above equations that the time-step is dependent on the sonic velocity through the material, which in turn is dependent on the density and Young's Modulus. Increasing the density of a structural element will therefore reduce the time-step of an analysis, providing the time-step is controlled by that element in the first place. LS-DYNA incorporates several options that use this speed-up technique to control the time-step of the model e.g. adding mass or reducing the Young's modulus. This method of artificially controlling the time-step should not be used when shock waves in that particular material are of primary importance if realistic results are required.

The critical time-step size, Δt_e, is computed for solid (fluid) elements from

$$\Delta t_e = \frac{L_e}{\left\{\left[Q + \left(Q^2 + c^2\right)^{\frac{1}{2}}\right]\right\}} \tag{25}$$

where Q is a function of the bulk viscosity (see section 4.1.6.1) coefficients B_0 and B_1, The default values are 1.5 and .06 respectively.

$$Q = \begin{cases} B_1 c + B_0 L_e \left|\dot{\varepsilon}_{kk}\right| & for\ \dot{\varepsilon}_{kk} < 0 \\ 0 & for\ \dot{\varepsilon}_{kk} \geq 0 \end{cases} \tag{26}$$

L_e is the characteristic length ($\text{characteristic length} = \frac{\text{element volume}}{\text{area of largest surface}}$), c is the adiabatic sound speed and $\dot{\varepsilon}_{kk}$ is the strain rate. In solid elements used as fluids, c is defined in the Gruneisen equation of state (see section 4.1.2).

The time-step in LS-DYNA is generally limited by stability i.e. if the Courant limit is exceeded the analysis may become unstable. LS-DYNA automatically calculates the largest time-step that can be used without triggering numerical instability. It is possible to lower the time-step of a fluid element by lowering the speed of sound, c, in the equation of state (this was also possible using the Linear Polynomial equation of state; however, the Gruneisen EOS offered a more direct method). The result of this speed-up technique is that the fluid becomes more compressible. Great care must be taken when using this method to save CPU time, even in models where compressibility is unimportant. Too large a reduction in the speed of sound can result in numerical error. For example when the fluid velocity, relative to objects in the flow, approaches the altered value of the sonic velocity c; this renders the compressibility of the fluid in the numerical model significant when in reality it would be negligible.

All elements are checked when calculating the required time-step therefore the element with the smallest time-step controls the time-step of the whole model. When it is Lagrangian elements that control the time-step it is usually the case that the time step falls during an analysis as these elements become deformed.

4.1.4 Boundary Conditions

The setting of wall boundary conditions was accomplished by making adjustments to the velocities of the boundary vertices. For a rigid no-slip wall the fluid velocity was set equal to the prescribed wall velocity by rigidly constraining the nodes in all directions. A rigid free-slip boundary is mathematically more difficult to handle, since it is only the fluid velocity normal to the boundary that is constrained by the application of a rigid constraint in that direction only. A free surface could also be defined when no constraints were applied and the tangential and normal stresses were zero.

Prescribed inflow and outflow boundaries were imposed by setting fluid velocities, fluid displacements or fluid pressures to the desired values at the interfaces between the flow domain and the ambient Eulerian elements of the reservoirs. This interface provided a boundary that either supplied or removed fluid from the main flow domain depending on the defined condition at the interface. Figure 4.1 depicts the process of supplying a volume of fluid to the main flow domain using ambient Eulerian elements utilising a pressure boundary at the interface.

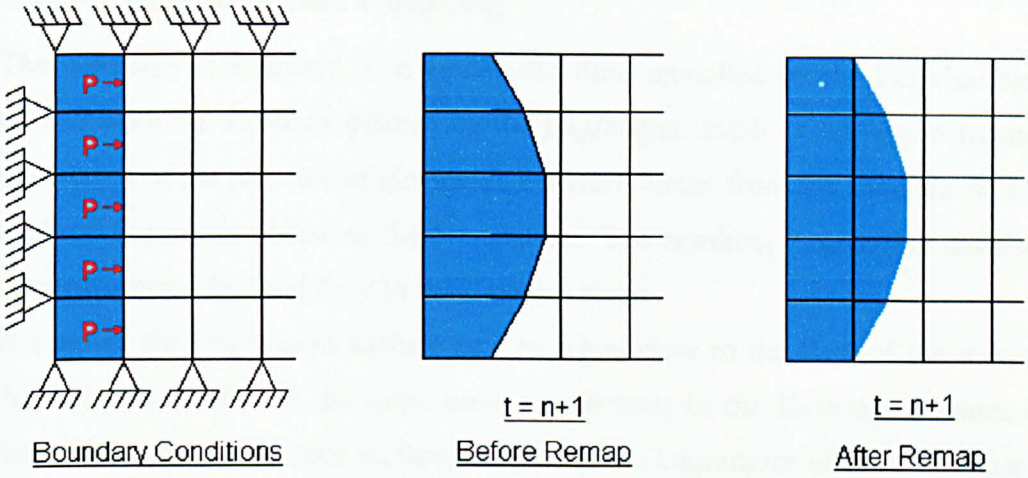

Figure 4.1. Ambient Eulerian elements supplying fluid to Eulerian elements via a pressure load at the interface. The results are shown after both the Lagrangian and Eulerian steps of the operator-split.

The left-hand column of elements (in blue) defines the ambient elements and the rest are normal Eulerian elements initially void of any fluid. The pressure loading on the interface results in a displacement of the material during the Lagrangian time-step. The mesh is then advected back to its original position leaving a volume of fluid in the second column of elements. Of course, the first-order accurate Doner cell advection algorithm (see section 4.1.2) causes the fluid that has just entered an Eulerian element to be smeared over the whole element and not to maintain its boundary as shown here. The ambient elements maintain their original volume of fluid no matter how much volume enters or leaves i.e. they represent a semi-infinite domain.

In this analysis pressure boundaries and displacements were used at the reservoir boundaries. The value of the displacement was controlled via a load curve where the gradient defined the fluid velocity i.e. the displacement load curve was differentiated in order to construct the velocity load curve. This method of flow rate control was found to offer more control over the flow than the velocity definition. The reason for this may be because the velocity and displacement are staggered in time in the explicit central difference method.

4.1.5 Fluid-Structure Coupling

The objective of coupling is to enable the fluid modelled by the Eulerian mesh to interact with the structure defined by the Lagrangian mesh. Coupling computes the interaction of the two sets of elements. Pressure forces from the Eulerian flow mesh load the Lagrangian mesh at the boundaries. The resulting Lagrangian deformation then influences the fluid flow in the Eulerian mesh.

In essence the Lagrangian surface acts as a boundary to the flow of the material in the Eulerian mesh. At the same time, the stresses in the Eulerian elements cause forces to act on the coupled surface, deforming the Lagrangian elements (Figure 4.2).

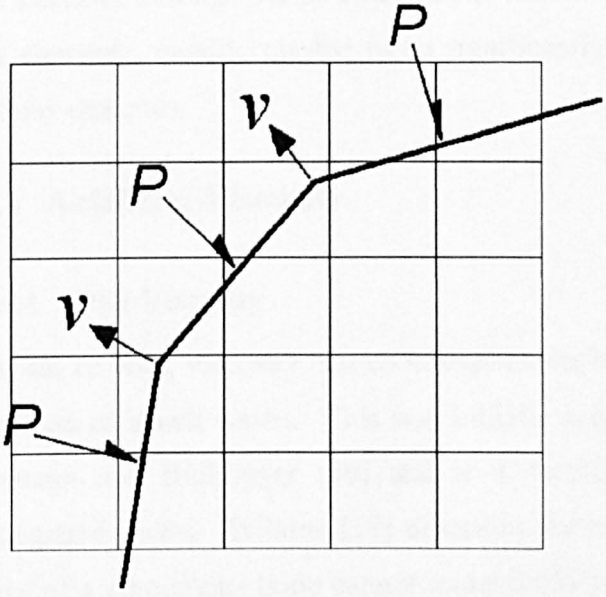

Figure 4.2. General coupling method used with the explicit technique. Lagrangian structural mesh within an Eulerian fluid mesh. *P* = pressure boundary condition exerted on Lagrangian elements by Eulerian elements, *v* = velocity boundary condition at Lagrangian nodes

This process is simplified in LS-DYNA since both Eulerian and Lagrangian parts follow the same explicit Lagrangian time-step. At the end of the time-step the Eulerian mesh is remapped while the Lagrangian structure remains deformed. By viewing the transient results of an Eulerian-Lagrangian coupling it would appear as if a fluid was moving through a spatially fixed mesh and deforming a structure defined by a separate mesh embedded within it.

The coupling method used in LS-DYNA was velocity coupling, which is related to the kinematic constraint contact method where [49] "Constraints are imposed on the global equations by a transformation of the nodal displacement components of the

slave (structure) nodes along the contact interface. This transformation has the effect of eliminating the normal degree of freedom of nodes. To preserve the efficiency of the explicit time integration, the mass is lumped to the extent that only the global degrees of freedom of each master (fluid) node are coupled. Impact and release conditions are imposed to insure momentum conservation.

Problems arise with this method when the master (fluid) surface zoning is finer than the slave (structure) surface zoning. Here certain master nodes can penetrate through the slave surface without resistance."

This may explain the observations of Carmody et al [5] who found that leakage of fluid occurred through the structural shell elements in the flow. To prevent this the shell elements, ideally, needed to be significantly smaller (half the edge length) of the fluid elements.

4.1.6 Artificial Viscosity

4.1.6.1 Bulk Viscosity

A shock, or bulk, viscosity is used in explicit codes such as LS-DYNA to control the formation of shock waves. This was initially proposed in one spatial dimension by Neumann and Richtmyer [56] and is a method now used in nearly all wave propagation codes. Wilkins [57] describes the method in detail. A finite element model of a continuous body cannot numerically represent a square shock wave such as would exist after an ideal impact between two flat surfaces. This is because severe oscillations in amplitude trail the shock front. These oscillations can be traced to the limitations imposed by the finite frequency spectrum of the finite element mesh.

Artificial bulk viscosity is introduced to control the oscillations trailing the shock front. The bulk viscosity increases the pressure in the shock front as a function of the strain rate. The effect on the shock wave is to keep it smeared over several elements.

4.1.6.2 Hourglass Viscosity

Hourglassing is a result of the use of single-point volume integration. One-point integration takes place at the centres of elements and is used since it is much less computationally expensive than integration at all the nodes of an element. A disadvantage is that zero-energy modes arise, called hourglass modes.

In two-dimensions there are eight degrees of freedom and eight modes of deformation in a four-noded shell element. These are depicted in Figure 4.3.

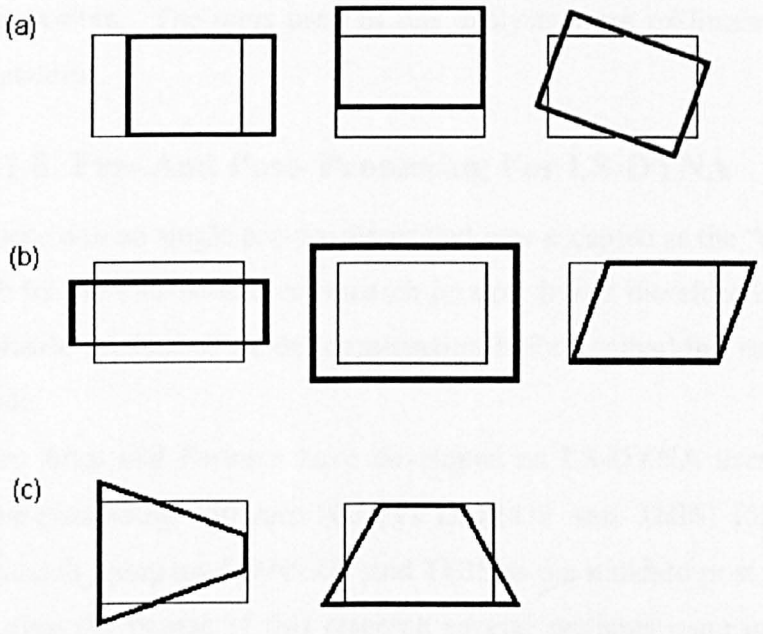

Figure 4.3. The eight degrees of freedom of a two-dimensional four-noded shell element; (a) rigid body modes, (b) stiffness modes, (c) hourglass modes. Figure adapted from [51]

There are two translational and one rotational mode where the element does not deform (Figure 4.3(a)). With single-point volume integration, two direct and one shear stress are calculated at the centre of the two-dimensional element. This means that only three modes of deformation have stiffness associated with them (Figure 4.3(b)). Two modes of deformation remain that correspond to linear stress terms; with single-point volume integration, these have no stiffness associated with them and are called the hourglass modes (Figure 4.3(c)).

Similar hourglass modes exist for hexahedral elements when single-point volume integration is used.

Hourglassing can rapidly spread through a mesh and degrade the accuracy of the calculation, reduce the time-step and cause the analysis to crash. One way of resisting undesirable hourglassing is by applying a viscous damping or small elastic stiffness capable of stopping the formation of anomalous modes, but having a negligible effect on the stable global modes.

4.1.7 Units

The units used by LS DYNA can be chosen arbitrarily providing the units are compatible. The units used in this analysis were millimetres, seconds, tonnes and Newtons.

4.1.8 Pre- And Post- Processing For LS-DYNA

There was no single pre-processor that was accepted as the "correct" software for the job by the soft-structures research group. It was therefore important to determine a suitable method of model construction before embarking on any serious use of the code.

Ove Arup and Partners have developed an LS-DYNA user interface that includes post-processing software (OASys D3PLOT and THIS) [58]. The soft-structures research group used D3PLOT and THIS as the standard post-processors.

During the course of this research several methods were used for constructing the LS-DYNA input file with FSI coupling. The reason for the changes was the ongoing development of LS-DYNA; and the inability or unsuitability of the older pre-processing software in successfully transforming a finite element model into an LS-DYNA input file complete with boundary conditions and FSI coupling.

The methods used are listed chronologically below and an example of modelling a flexible structure within a fluid control volume is used to give an explanation of the process.

Between 1997 and 1998 the fluid and structural models were created separately using the ANSYS [59] finite element package. The two ANSYS files were then converted into fixed format LS-DYNA input files using DYNASYS [60]. DYNASYS was a bespoke piece of Fortran software developed at the University of Sheffield and provided an interface between ANSYS and LS-DYNA. The separate structural and fluid input files were then combined using OASys INFMERGE [58]. The coupled fixed format input file was then manually edited in order to provide LS-DYNA with the additional information needed to model the fluid-structure interaction.

Between 1998 and 2000 HYPERMESH [61] was used to construct both fluid and solid parts together. HYPERMESH is a high-performance finite element pre-processor that enables the quick and efficient creation of finite element and finite difference models for many engineering simulation and analysis codes.

HYPERMESH is able to interface directly with LS-DYNA in Keyword format, although the Keyword library in HYPERMESH was far from complete. The HYPERMESH/LS-DYNA interface template required some editing in order to include coupling details needed for fluid-structure interaction and various other requirements.

The fluid and structural parts were created simultaneously in HYPERMESH. The coupled FE model was then converted into an LS-DYNA input file using the modified version of the standard LS-DYNA template file in HYPERMESH. Additional editing was carried out manually when needed.

From 1998 LS-DYNA and HYPERMESH were installed on a SUN ULTRA 10 (Ticker) with a single 336Mhz ULTRASparc processor, for exclusive use by the Soft-Structures research group, and a SUN ENTERPRISE E4500 (Gold) with 14 x 336Mhz ULTRASparc processors, although no parallel processing was attempted. The SILICON GRAPHICS ORIGIN 2000 (Kilburn) at Manchester University was also used to run LS-DYNA analyses up until the end of 1999.

5 Collapsible Tube Experiments

The experimental work presented here was conducted in the fluid mechanics laboratory at the University of Sheffield.

5.1 Construction of the Experiment

The experimental rig consisted of an airtight glass container through which ran a tube with a collapsible section (Figure 5.1).

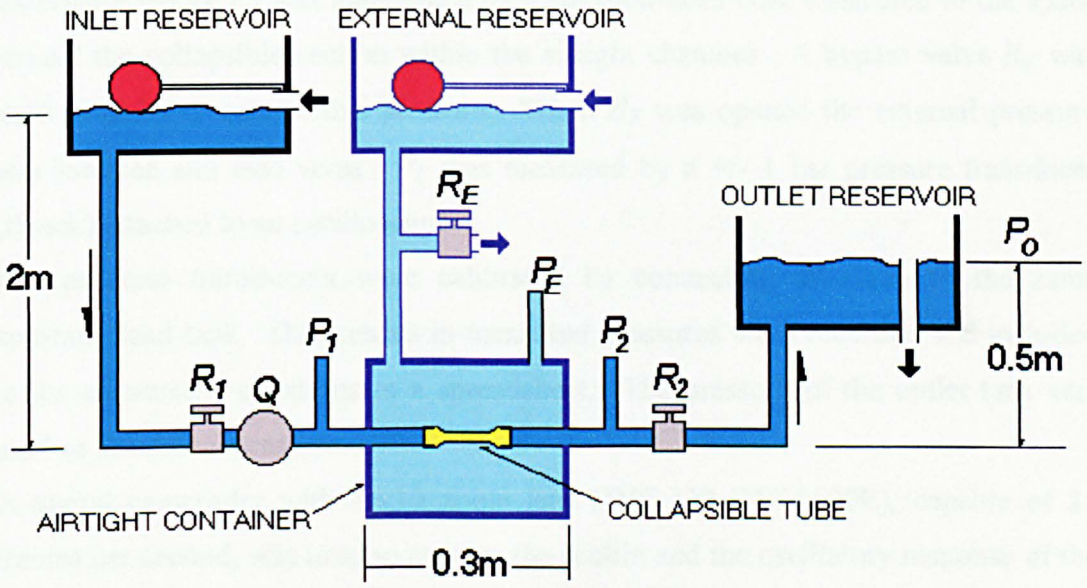

Figure 5.1. Schematic diagram of the experimental set-up used in the collapsible tube experiments. Some approximate dimensions are given. *P* = pressure measurement, *Q* = flow rate measurement and *R* = flow resistance

Water flowed by gravity from a constant-head inlet tank through the collapsible section within the glass container and out into another constant-head tank. The glass container was pressurised by a separate constant-head tank.

5.1.1 Data Retrieval

Flow rate, Q, was measured by one of two variable-area flow meters situated upstream of the collapsible section. One for flows between 0.133 – 1.33 litres/min (George Fischer). The other for flows between 0.02 and 0.2 litres/min (Fisher Scientific).

Flow was controllable via two resistances upstream, R_1, and downstream, R_2, of the collapsible section. Gate valves were used for these resistances.

Pressures were measured 18 cm upstream, P_1, and 18 cm downstream, P_2, of the collapsible section. Pressure transducers of +/- 1 bar sensitivity (Druck) and a 12V-power supply were used. These pressure transducers were then connected to a dual-band oscilloscope (Tektronix TDS210) for the steady-flow analysis. For oscillatory analysis the pressure transducers were attached to a floating-point controller board (dSPACE DS1102) and a computer with trace software (dSPACE) enabling oscillatory response to be captured over a period of time.

External pressure P_E was maintained by a constant-head tank connected to the space around the collapsible section within the airtight chamber. A bypass valve R_E was used in order to control this pressure. When R_E was opened the external pressure was lowered and vice versa. P_E was measured by a +/- 1 bar pressure transducer (Druck) attached to an oscilloscope.

The pressure transducers were calibrated by connecting all three to the same constant-head tank. Differences in measured pressures were recorded and included in the conversion equations in a spreadsheet. The pressure of the outlet tank was used as the datum pressure.

A digital camcorder with a x10 zoom lens (JVC GR-DVL9500E), capable of 25 frames per second, was used to capture the profile and the oscillatory response of the collapsed tube. A single 100-watt spotlight was used for lighting.

5.1.2 The Airtight Container

The design of the container had to comply with the following points:

- The container needed to be airtight.
- The volume of the airtight container needed to be large enough to render negligible the pressure change due to any changes of the collapsible tube volume. Conrad [9] used a value of 400 times the tube volume.
- The container needed to be designed to allow photography from the side, the top and a view facing the tube inlet and outlet.
- Access to the interior of the container was needed in order to replace the collapsible tube.
- Holes in the container were needed for inlet, outlet, external pressurisation and the bleeding of air

- The container needed to safely withstand the maximum pressures, stresses etc imposed on it.

It was decided to construct a rectangular box with glass sides. The dimensions were chosen as 300 x 300 x 190 mm (interior dimensions) since this allowed views from several angles and exceeded the specifications of Conrad (assuming a tube of 13 mm diameter not exceeding 25 diameters in length).

The airtight box was constructed from one-inch angle iron welded into a frame with a flange at the top to receive the lid. Holes were drilled in the flange of the frame and 5mm nuts were brazed in place on the under side so that bolts could be permanently positioned. Corresponding holes were drilled in the flange of the lid so that it could be positioned on the framework. The lid could then be attached using either 5mm nuts or G-clamps. A rubber gasket was situated at the frame/lid interface to render the container airtight

The thickness of the glass was dependent on the maximum working pressure. In experiments carried out by other researchers the maximum pressure was usually 44 mmHg (6 kPa) [9, 10, 11]. Rodbard and Saiki [14] measured a peak pressure of 100 cmH_2O (10 kPa). The size and material properties of the tube determined these values; a stiffer tube requires a larger pressure to collapse it.

The tube used in these experiments was similar to that used by the researchers listed above so their peak pressure values were used as an indication as to what was needed in this case. The maximum working pressure of the system was determined by the sum of the outlet reservoir head and the required maximum external pressure. The maximum required external pressure was 60 cmH_2O (6 kPa) and the location of the set-up meant that the outlet reservoir need not exceed 50 cm above the base of the container. So a pressure of 110 cmH_2O (11 kPa) was calculated as the maximum pressure the airtight box was likely to experience. For safety this was doubled to cater for rapidly applied loads and any increase in external pressure that may be required. Plate glass of 10mm thickness was used (see appendix B).

In all, four holes were needed in the container. An inlet and outlet for the collapsible section; an attachment to the external reservoir constant-head tank; and a means to bleed the air from the container and measure the external pressure P_E. The latter was placed in the frame but the former three needed to be in the glass walls. The size of these holes was determined by the tank attachments for ½ inch ABS tubing (Durapipe). Although 3/8 inch ABS tubing was used as the rigid inlet and outlet

tubes it was decided to use ½ inch tank attachments with reducing bushes in case a larger-diameter collapsible tube was to be analysed. Fittings any larger than ½ inch would have obstructed the view facing the inlet and outlet of the collapsible tube.

The plate glass was sealed into place in the framework using silicone sealant of a type normally used for building aquariums.

A pressure tap was placed just beneath the glass of the lid. This was done in order to provide a means for the attachment of a pressure transducer and to bleed the air from the container. This could be achieved by tilting the container as it filled up with water.

The design of the airtight box and means of lid attachment can be seen in Figure 5.2 and Figure 5.3 respectively.

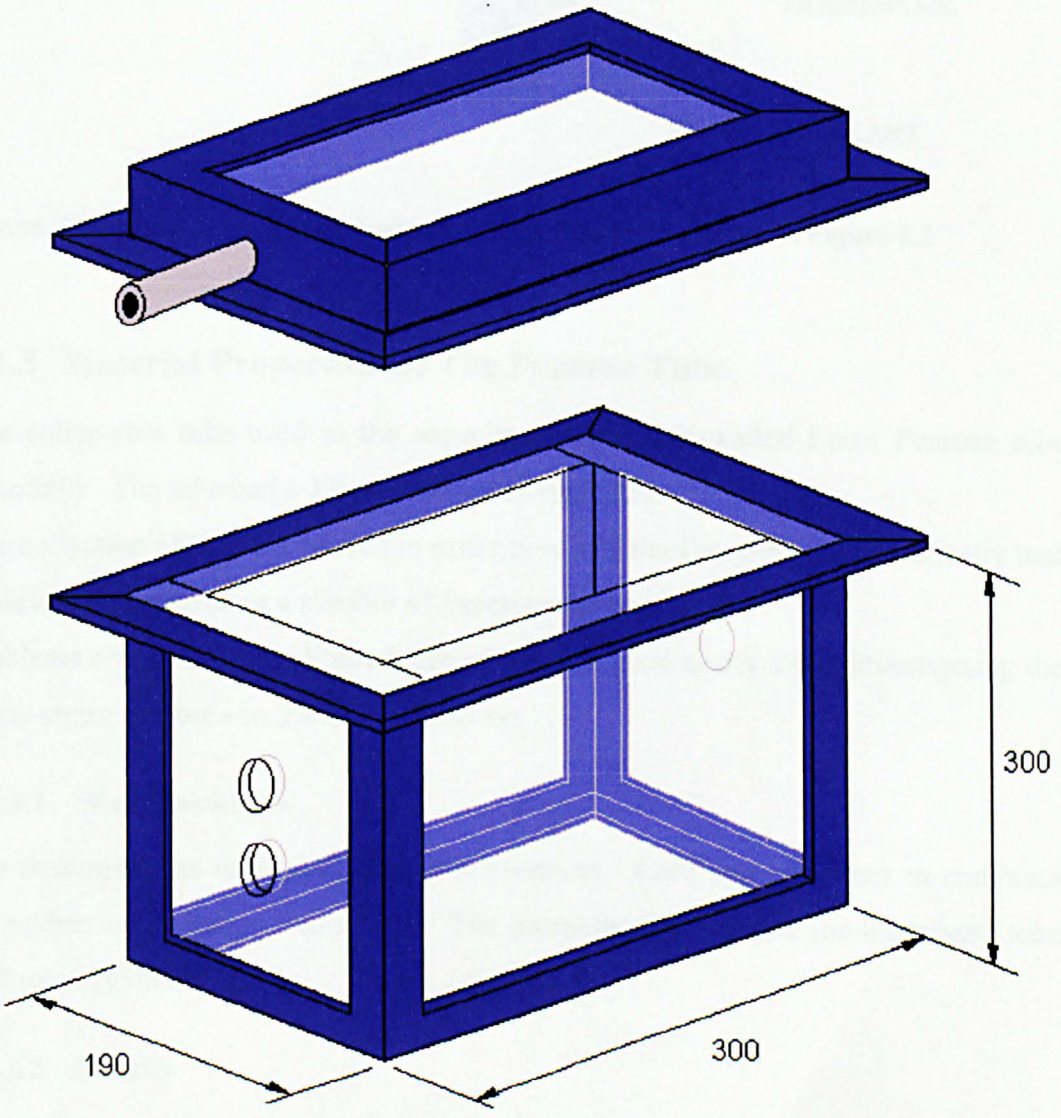

Figure 5.2. Diagram of the glass airtight box used in the collapsible tube experiments. Given dimensions are measured internally in mm.

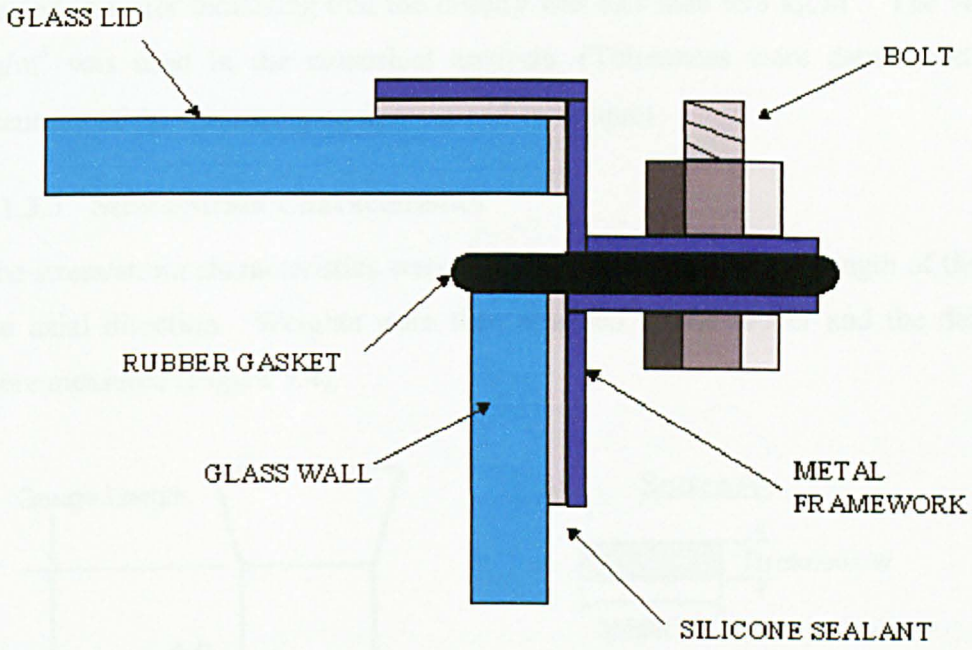

Figure 5.3. Method of lid attachment for the airtight box shown in Figure 5.2

5.1.3 Material Properties Of The Penrose Tube

The collapsible tube used in the experiments was thin-walled Latex Penrose tube (Kendall). The tube had a 13mm unstressed diameter.

The collection of the data needed in order to model the Penrose tube numerically was achieved by performing a number of experiments on the tube.

Problems arose due to the limited size of the tube particularly when investigating the stress-strain response in the radial direction.

5.1.3.1 Wall Thickness

The thickness was measured using a micrometer. Care was taken not to compress the rubber as the gauge was closed. The measured thickness of the unstressed tube wall was 0.35mm +/-0.01.

5.1.3.2 Density

The density of the rubber was measured by weighing several tubes on a set of electronic scales. The total volume of the tubes was then calculated from the measured values of width, length and thickness. Four tubes weighed 22.2g +/-0.1.

The total length was 1812mm, width was 38mm+/-0.5 and the thickness was 0.35mm +/-0.01. Density was therefore 920 kg/m^3 +/-4.5%. The tube material floated in water indicating that the density was less than 998 kg/m^3. The value 920 kg/m^3 was used in the numerical analysis. (Tolerances were determined by the accuracy of the measuring equipment and technique)

5.1.3.3 Stress/Strain Characteristics

The stress/strain characteristics were measured by marking off a length of the tube in the axial direction. Weights were then attached to the rubber and the deflections were measured (Figure 5.4).

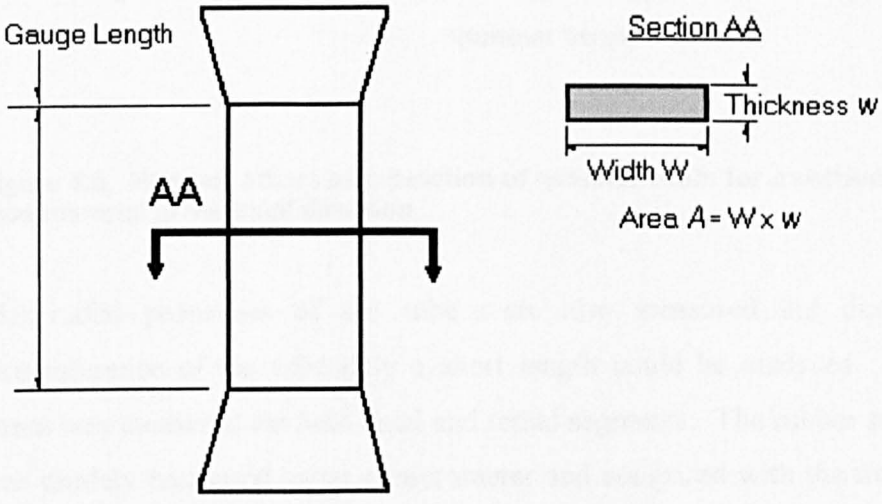

Figure 5.4. Description of the experiment used to retrieve stress v strain characteristics of the collapsible tube

From this force/deflection data a nominal stress and nominal strain were calculated and plotted as shown in Figure 5.5.

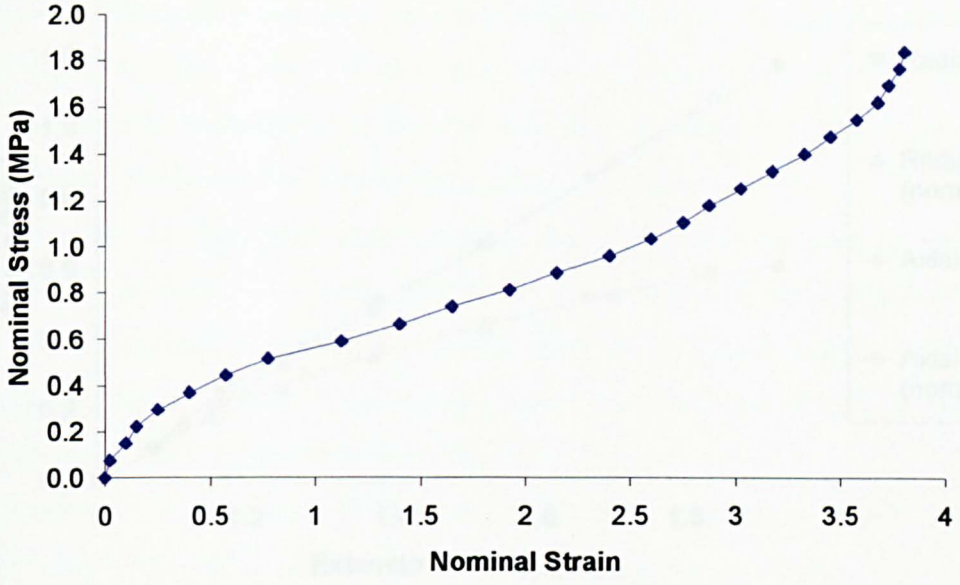

Figure 5.5. Nominal stress as a function of nominal strain for a section of the Penrose tube material in the axial direction

The radial properties of the tube were also measured but due to the small circumference of the tube only a short length could be analysed. The horizontal strain was measured for both axial and radial segments. The rubber section thickness was crudely measured using a micrometer and compared with the through thickness strain calculated by assuming that Poisson's ratio was 0.5 (typical value for natural rubber). This assumption meant that the thickness could be calculated since there was no change in volume of the rubber section.

$$w_n = \frac{L_0 \times W_0 \times w_0}{L_n \times W_n} \tag{27}$$

where w_n is the thickness of the rubber section at stress n, w_0 is the original thickness, L = length of rubber section, W = width of rubber section. These calculated thickness values differed by no more than 7% compared with the crude micrometer-measured values.

The true stress was plotted against the extension ratio (L_n/L_0). The results can be seen in Figure 5.6 for a range of axial and radial strains.

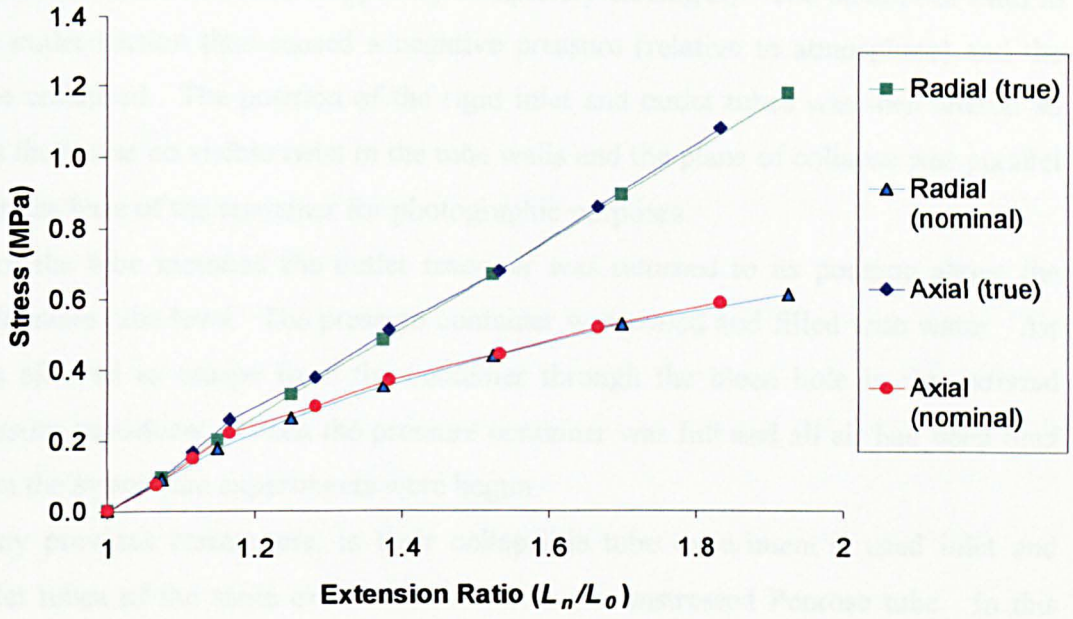

Figure 5.6. True and nominal stress as a function of extension ratio for sections of the Penrose tube in both the axial and radial direction

It can be seen that over this range the rubber is Hookean. There is also no significant difference between radial and axial properties over this range. Assuming the stresses in the tube wall during the collapsible tube experiments do not exceed 1 MPa the tube material can be approximated as an isotropic Linear Elastic material of Young's Modulus 1.3 MPa.

5.1.4 Mounting The Tube In The Airtight Container

The plane of collapse of the tube was determined by the residual stresses due to manufacture and packing. The Penrose tubes were packed flat.

A length from the centre section of a new tube was marked off using water-soluble ink. The tube was cut approximately 2 tube diameters either side of the marks in order to provide enough material to mount onto the rigid inlet and outlet sections. The tube was then carefully stretched onto the removable inlet and outlet sections and the marks were lined up with the edges of these sections. The tube was held in place using 9.5cm cable ties and rubber o-rings of a smaller internal diameter than the rigid sections. The inlet and outlet sections were then push-fitted into position within the pressure container. Fluid was allowed to flow from the inlet reservoir to the outlet reservoir that was temporarily placed in a position beneath the pressure

container. Flow was then stopped by completely closing R_1. The column of fluid in the outlet section thus caused a negative pressure (relative to atmosphere) and the tube collapsed. The position of the rigid inlet and outlet tubes was then altered so that there was no visible twist in the tube walls and the plane of collapse was parallel with the base of the container for photographic purposes.

With the tube mounted the outlet reservoir was returned to its position above the collapsible tube level. The pressure container was sealed and filled with water. Air was allowed to escape from the container through the bleed hole in the external pressure transducer. When the pressure container was full and all air had been bled from the system the experiments were begun.

Many previous researchers, in their collapsible tube experiment's, used inlet and outlet tubes of the same external diameter as the unstressed Penrose tube. In this study the rigid sections had an external diameter of 17mm and the Penrose tube 13mm diameter. These over-sized rigid sections were initially used for convenience since plastic (ABS) tubing of this diameter was readily available. The consequence was a radial tension in the collapsible tube when mounted and a corresponding axial tension due to the Poisson effect. The distance between the inlet and outlet sections was 65mm so a section of Penrose tube of unstressed length 65mm would be axially stressed when mounted. It was decided that there was no reason to change the 17mm diameter rigid sections for the following reason. The purpose of the experiment was for comparison with a numerical code and as long as the numerical code modelled this particular condition there was no need to change it.

5.1.5 Other Components

The inlet, outlet and external reservoirs were constructed of large plastic storage containers. Ball-cock valve controlled the inlet and external reservoir levels and a standpipe controlled the outlet level. The reservoirs, data-retrieval components and airtight container were connected to one other using hosepipe (Hoselock), hose fittings (Hoselock) and ABS fittings (Durapipe).

5.2 The Zero Flow Experiment

Before the standard collapsible-tube experiment could be performed the desired length of tube needed to be determined. The gap between inlet and outlet rigid

sections was 65mm. The unstressed tube was of diameter 13mm and was to be stretched onto the rigid sections of 17mm diameter.

5.2.1 Method

Unstressed tube lengths of 65mm, 66mm and 67mm were tested for transmural pressures of 0, -20, -40 cmH_2O.

In order to attain a zero flow condition the experiment was set up in a slightly different way to that shown in Figure 5.1. To ensure accuracy of the zero transmural pressure condition the pressure container and the tube inlet and outlet were all attached to the inlet reservoir. Provision was made for the bleeding of air from the system by allowing the water to flow through a valve open to the atmosphere. Once all the air had been expelled the valve was shut.

For the negative transmural pressures the pressure container was attached to the external reservoir while inlet and outlet were attached to the inlet reservoir. This meant that the external pressure could be altered independently of the internal pressure.

5.2.2 Results

The resulting tube profiles for unstressed tube lengths of 65mm and 67mm can be seen in Figure 5.7.

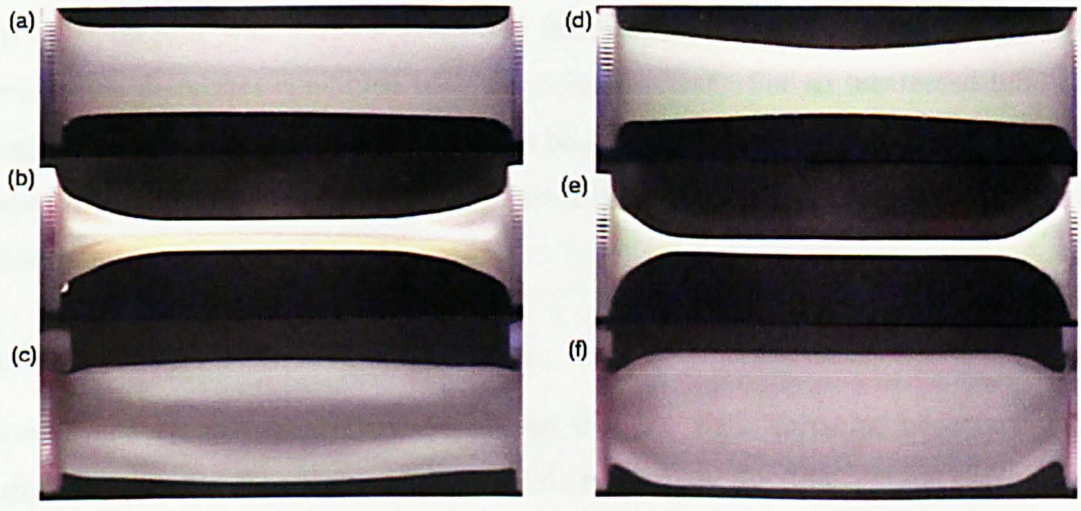

Figure 5.7 Tube profiles for various unstressed tube lengths and transmural pressures with zero flow. (a) side view, L = 65mm, P_{TM} = 0 cmH_2O; (b) side view, 65mm, 40 cmH_2O; (c) top view, 65mm, P_{TM} = 40 cmH_2O; (d) side view, 67mm, P_{TM} = 0 cmH_2O; (e) side view, 67mm, P_{TM} = 40 cmH_2O; (f) top view, 67mm, P_{TM} = 40 cmH_2O.

At zero transmural pressure the 65mm tube (Figure 5.7(a)) had very straight upper and lower walls while the extra slack in the 67mm tube (Figure 5.7(d)) was apparent due to the curved nature of the top and bottom surfaces. In all cases the tube collapsed when the transmural pressure turned negative. The tube came into contact with itself at the centre and as the transmural pressure was further decreased the contact region in the centre of the tube moved towards either end. The collapse of the 65mm tube at a transmural pressure of –40 cmH_2O (Figure 5.7(b) and (c)) resulted in ridges on both top and bottom surfaces which were slightly offset from the centreline. The corresponding collapse for the 67mm tube can be seen in Figure 5.7(e) and (f) and is the profile observed by many past researchers for a collapsible tube with negligible internal flow [e.g. 9, 11]. On both sides of the tube in Figure 5.7(f) the edges can be seen to bulge up slightly more than in the centre of the tube. This is due to the bending stresses where the tube material folds over and results in two relatively rigid tunnels.

The flat collapse profile of Figure 5.7(e) and (f) was more desirable, from an analytical viewpoint, than that of Figure 5.7(b) and (c) purely because it was a simpler geometry and that this was the collapse profile observed by so many other researchers. The reason for the ridges in Figure 5.7(b) and (c) was the stresses induced by the 13mm diameter tube being stretched onto a 17mm rigid tube.

5.2.3 Conclusions Drawn From The Zero Flow Experiment

An axial tension was introduced by the difference between rigid and unstressed deformable diameters combined with the Poisson effect. For an unstressed tube of length 65 mm this tension caused ridges to be present on the top and bottom walls of the tube after collapse. In order to maintain a 'flat collapse' unstressed tube lengths of 66 mm or 67 mm needed to be used.

5.3 Steady Flow Experiments

Brower and Noordergraaf [10] determined that the state variables necessary and sufficient to define steady flow in collapsible tubes were the flow, Q, and two of the three definable pressure differences, $P_1 - P_2$, P_E-P_2, and P_E-P_1. The various other quantities R_1, R_2 and upstream and downstream reservoir pressure, while perhaps necessary to conduct the experiment, were unessential for the characterisation of the flexible tube itself. The important parameters were all measured close to the tube

and therefore experiments that utilised two of the above pressure differences and the flow rate were desirable for comparison with the computational model since it would not be practicable to model the whole system.

The experiments performed by Conrad [9] required a controllable value of downstream resistance and a known outlet reservoir pressure and were therefore not ideal for comparison with the computational model. However, these experiments were performed in order to gain a better understanding of the collapsible tube phenomenon. The method and results of these experiments are given in appendix C.

5.3.1 Method

A section of Penrose tube was mounted on the inlet and outlet sections so that an undeformed length of 66 mm occupied the 65 mm gap. The 1 mm of slack was taken up by the radial and axial tension caused by the inlet and outlet tubes being of larger diameter than the undeformed Penrose tube diameter.

The method employed for each characteristic curve was to fix external pressure P_E at some value above the measured outlet pressure P_2 ($P_E - P_2$ = constant). The control of the downstream constriction, R_2, was not required in this particular experiment and was left fully open. P_1 and P_2 were free to vary as the flow was varied. This control of flow was achieved by opening or closing the upstream resistance R_1.

The tube was initially flat with zero flow. As flow was increased P_2 increased and the pressure difference P_E - P_2 was maintained at a constant value by gradually closing the external reservoir bypass valve, R_E.

5.3.2 Results And Discussion

The values of P_1 - P_2 were recorded for 16 flow rates between 0 and 1.17 litres/min. Plotting these values on a graph for $P_E - P_2$ values of 60 cmH_2O down to 10 cmH_2O, in increments of 10 cmH_2O resulted in a family of characteristic curves as shown in Figure 5.8. The experimental procedure was carried out from left to right on the graph.

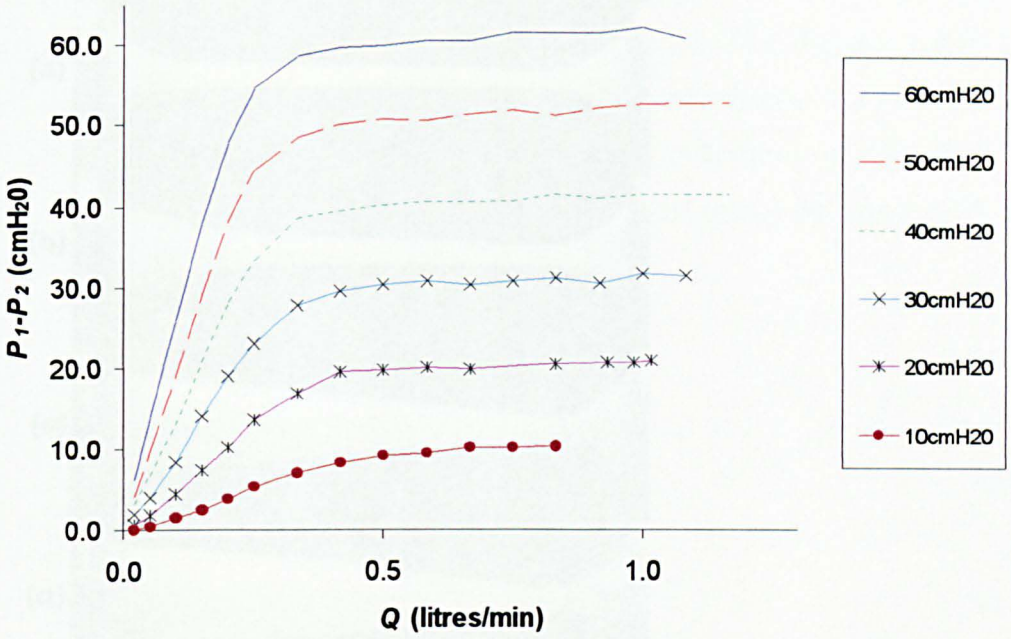

Figure 5.8. Family of characteristic curves for values of $P_E - P_2$ shown in the legend (cmH_2O) and an undeformed tube length L = 66mm.

The highly collapsed tube at low flow rate formed a rigid structure consisting of two channels of small cross-sectional area. This meant that viscosity was significant and the resistance to flow was proportional to both the viscosity and the length of the collapsed section and inversely proportional to the cross-sectional area. Therefore Poiseuille's law was true, this can be seen by the linear nature of the curves of P_1 and P_2 up to approximately $Q = 0.25$ litres/min.

The side profile of the tubes can be seen at various values of Q in Figure 5.9.

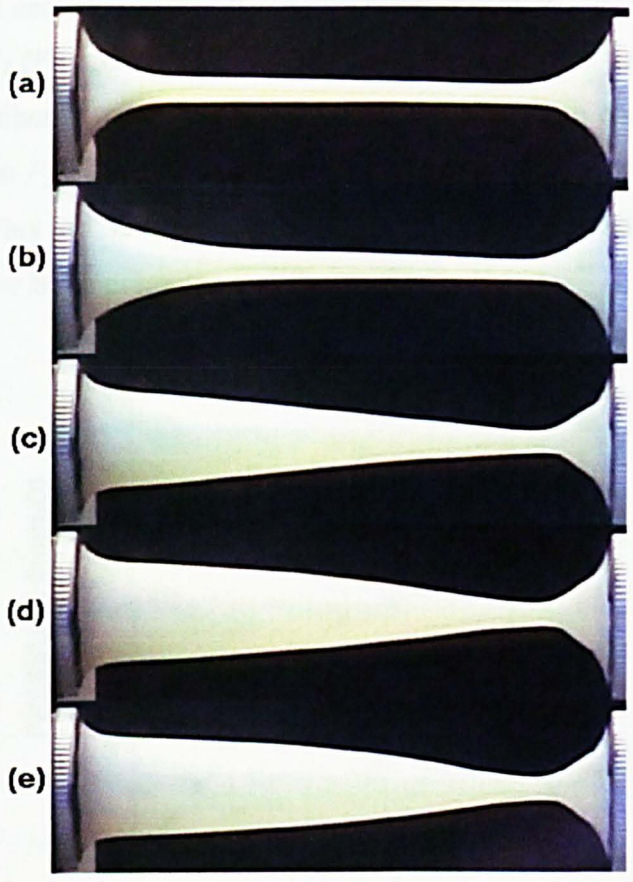

Figure 5.9. Side profile of the collapsible tube under steady flow conditions $P_E - P_2$ = 40 cmH_2O and Q = (a) 0.02 litres/min; (b) 0.25 litres/min; (c) 0.5 litres/min; (d) 0.75 litres/min; (e) 1 litres/min.

Figure 5.9(a) shows the rigid geometry explained above. As Q was increased the contact at the centre of the tube was broken at the upstream end and began to open up into a circular or oval cross-section. This can be seen in Figure 5.9(b), which corresponds to the area on the curve in Figure 5.8 where the relationship between flow rate and pressure drop stopped being linear. This opening of the tube reached further downstream with increases in Q until just a single pinch existed near the downstream (Figure 5.9(c)).

As the flow rate was increased further the tube geometry did not appear, to the naked eye, to alter while $P_1 - P_2$ remained constant (Figure 5.9(d) and (e)). However, further analysis of the profiles proved that there was a slight change in geometry in that the pinch moved slightly closer to the outlet. At some value of Q oscillations began and increased in frequency and magnitude as Q was further increased (not shown in Figure 5.9).

It can be seen that the maximum value of P_1 - P_2 was very close to the value of P_E - P_2 (Figure 5.8) for all of the curves. It can also be seen that this value of P_1 - P_2 was adhered to as Q is increased. This is pressure drop limitation; P_1 - P_2 depends only on P_E - P_2 and is independent of P_1, which now influences only the flow rate, Q. This can be explained by viewing Figure 5.10, which shows the relationship between the three pressures at different flow rates.

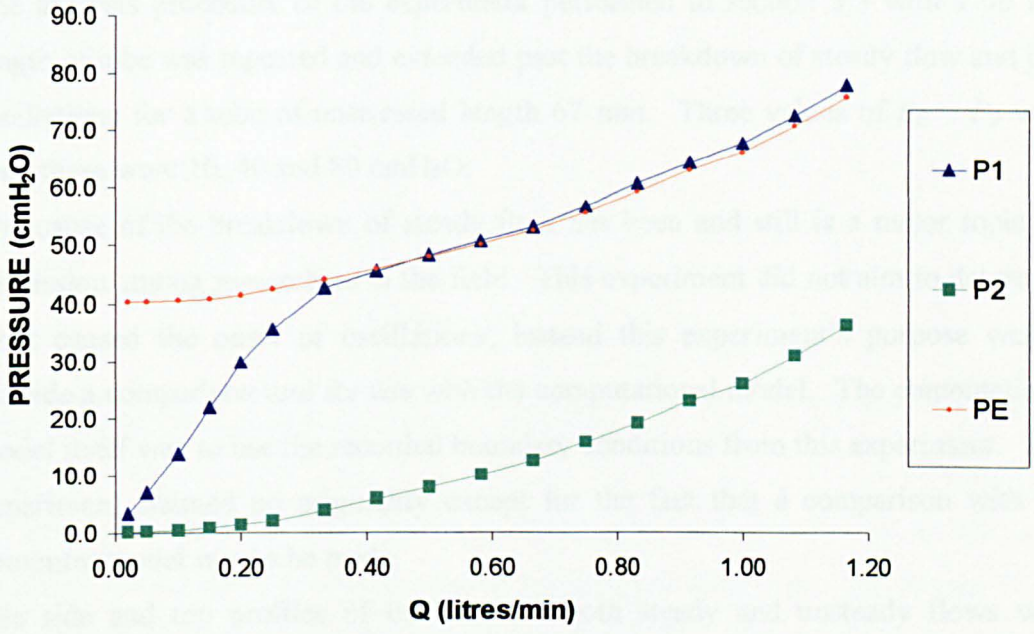

Figure 5.10. Relationship between P_1, P_2 and P_E for P_E - P_2 = 40 cmH$_2$O

For flow rates lower than about 0.33 litres/min small increases in Q resulted in large increases in P_1 and relatively small increases in P_E and P_2. This was explained above as a consequence of the high resistance of the heavily collapsed tube. While P_1 was less than P_E the tube would remain collapsed along its length and this high resistance to flow would remain.

As P_1 approached P_E between 0.25 and 0.33 litres/min the increase in P_1 with Q became less significant since the tube was more easily opened which reduced the length of the contact region and hence reduced the resistance to flow. This had the effect of increasing P_2.

For flow rates larger than about 0.33 litres/min any further opening of R_1 resulted in an increase in P_2 while P_1 maintained the same value as P_E. P_E then needed to be increased for a constant value of $P_E - P_2$ to be maintained. The value of P_1 increased

as P_E was increased. This resulted in the constant value of $P_1 - P_2$ for any value of Q above about 0.33 litres/min.

5.4 Unsteady Flow Experiments

5.4.1 Method

The analysis procedure of the experiment performed in section 5.3 with a 66 mm length of tube was repeated and extended past the breakdown of steady flow and into oscillations for a tube of unstressed length 67 mm. Three values of $P_E - P_2$ were used these were 10, 40 and 80 cmH_2O.

The cause of the breakdown of steady flow has been and still is a major topic for discussion among researchers in the field. This experiment did not aim to determine what caused the onset of oscillations; instead this experiment's purpose was to provide a comparison tool for use with the computational model. The computational model itself was to use the recorded boundary conditions from this experiment. This experiment claimed no originality except for the fact that a comparison with the computer model was to be made.

The side and top profiles of the tube for both steady and unsteady flows were captured for use in comparison with the computational model.

5.4.2 Results And Discussion

The characteristic curves are shown in Figure 5.11.

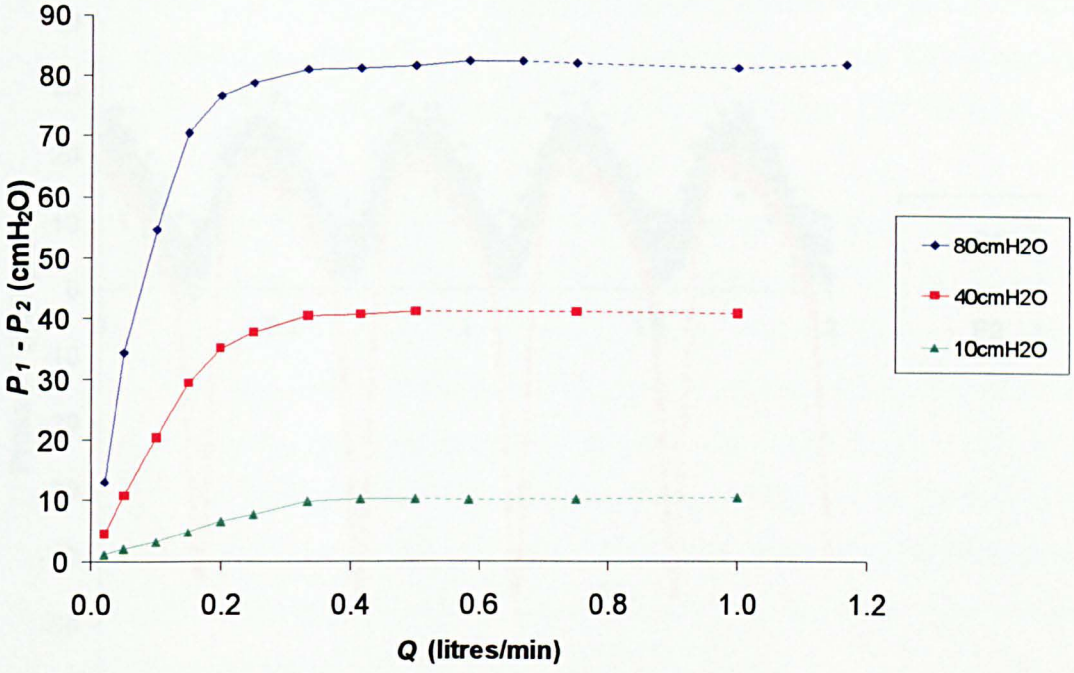

Figure 5.11. Family of characteristic curves for values of $P_E - P_2$ shown in the legend (cmH_2O) and an undeformed tube length L = 67mm.

The first observation when comparing Figure 5.11 with Figure 5.8 is that the breakdown of steady flow occurred at a much lower flow rate. In Figure 5.11 oscillations were present at Q = 0.5 litres/min for all P_E - P_2 values. In Figure 5.8 oscillations are not visible until at least 0.8 litres/min and in most cases not until flow exceeded 1 litres/min. This was due to the initial tension in the tube being lower for the 67 mm tube and therefore the critical flow rate at which oscillations occurred was also lower. This corresponded qualitatively with the theory of Brower and Scholten [17] who related the breakdown of steady flow to the fluid velocity approaching the phase velocity of the tube. Removing some of the axial tension in the tube reduced the phase velocity in this case; hence oscillations began at lower flow rates.

The response of P_1 and P_2 was recorded at a flow rate of 1 litres/min for $P_E - P_2$ values of 10 cmH_2O and 80 cmH_2O. These are shown in Figure 5.12 and Figure 5.13 respectively using different scales of pressure but similar scales in the time domain.

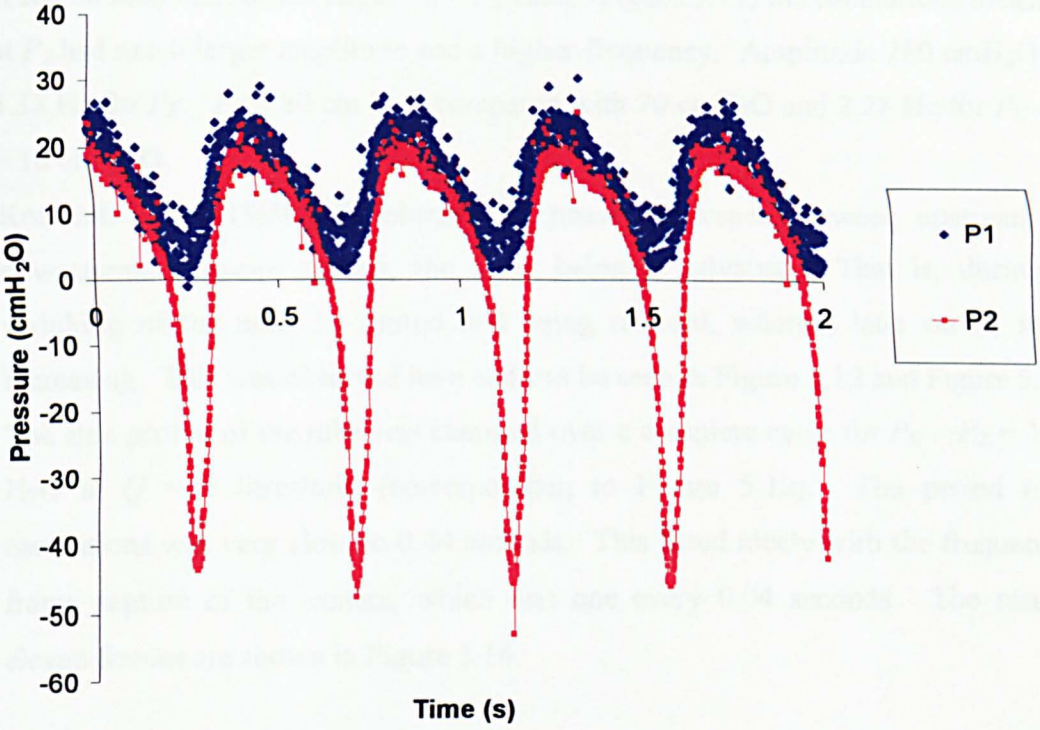

Figure 5.12. Unsteady pressures at P_1 and P_2 at a flow rate of 1 litres/min for $P_E - P_2$ = 10cmH_2O

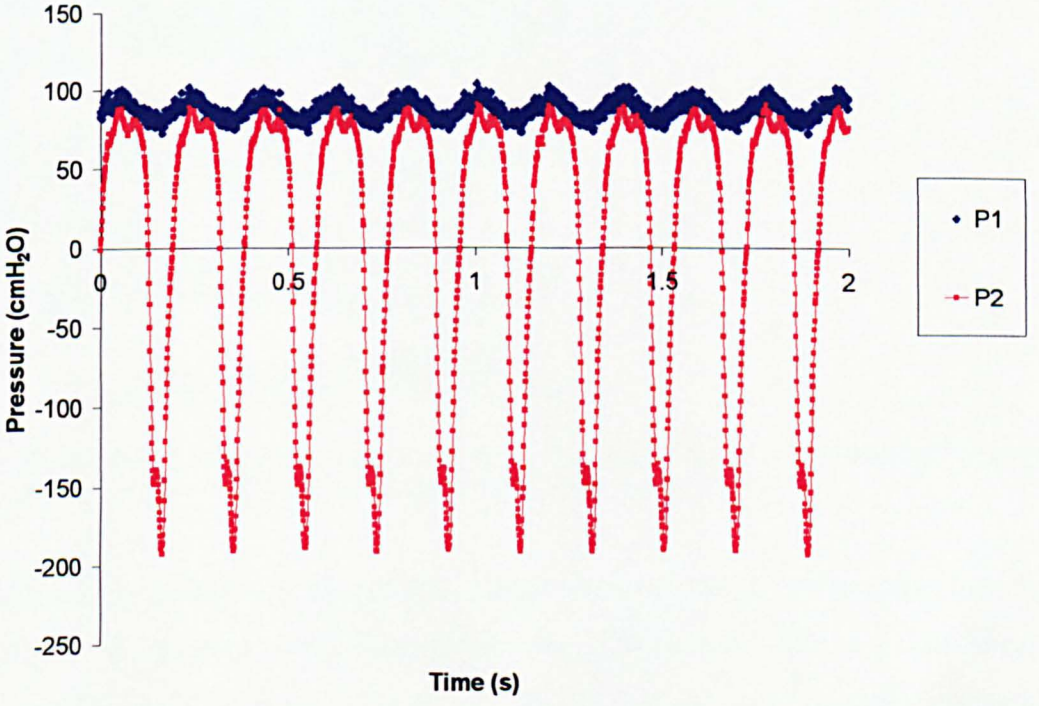

Figure 5.13. Unsteady pressures at P_1 and P_2 at a flow rate of 1 litres/min for $P_E - P_2$ = 80cmH_2O

It can be seen that for the larger $P_E - P_2$ value (Figure 5.13) the oscillations measured at P_2 had much larger amplitude and a higher frequency. Amplitude 280 cmH_2O and 5.33 Hz for $P_E - P_2$ = 80 cm H_2O compared with 70 cmH_2O and 2.28 Hz for $P_E - P_2$ = 10 cm H_2O.

Kounanis et al 1999 [18] observed a phase difference between upstream and downstream pressure signals, the latter being in advance. That is, during the shrinking of the tube, P_2 started first being reduced, whereas later on P_1 started increasing. This was observed here and can be seen in Figure 5.12 and Figure 5.13.

The side profile of the tube was captured over a complete cycle for $P_E - P_2$ = 10 cm H_2O at Q = 1 litres/min (corresponding to Figure 5.12). The period of the oscillations was very close to 0.44 seconds. This fitted nicely with the frequency of frame capture of the camera, which was one every 0.04 seconds. The resulting eleven frames are shown in Figure 5.14.

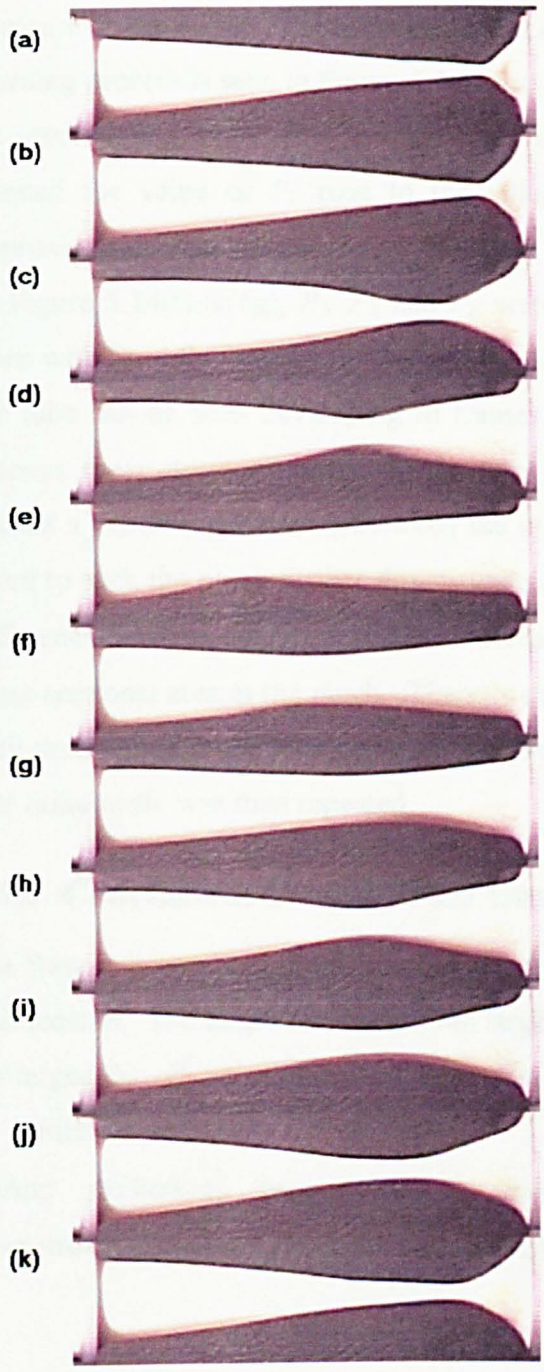

Figure 5.14. Transient response of the collapsible tube at a flow rate of 1 litres/min for $P_E - P_2 = 10cmH_2O$. Frames separated by 0.04 seconds.

The tube is shown in (a) when the pinch was at its closest to the outlet. The cause of the breakdown of steady flow was not considered here. Instead a description of the oscillations was made. Figure (a) represented the tube just after collapse. The collapse process caused the kinetic energy of the upstream fluid to be converted into a pressure increase. Also, the tube stresses at this point in time acting in the opposite direction to the flow due to the shear of the fluid and the suction from the low

pressure at the outlet. These two effects combined to cause the tube to open. The opening process is seen in Figure 5.14(a) to (e), where the tube walls at the pinch can be seen parting and a smaller pinch can be seen moving upstream. As the tube opened the value of P_2 rose to the value of P_1 (see Figure 5.12), which was approximately equal to P_E.

In Figure 5.14(f) to (g), P_1, P_2 and P_E were approximately equal and the tube was open with fluid flowing freely through it. A pinch slightly to the downstream side of the tube can be seen developing in frames (h) and (i). This was the result of the viscous shear stresses exerted on the tube walls by the flowing fluid. The pinch caused a pressure difference between the upstream and downstream sections, which acted to suck the pinch further downstream in (j) and (k). There was also a pressure difference between the outlet and the external sections that acted to further reduce the cross-sectional area at the pinch. Therefore the pinch was pulled further downstream until the stresses in the tube walls were significant enough to stop this movement (a). The same cycle was then repeated.

5.4.3 Conclusions Drawn From Unsteady Flow Experiments

The flow rate at which breakdown of steady flow occurred was dependent on axial wall tension. The larger the tension the larger the flow rate.

For larger $P_E - P_2$ values the oscillations had larger amplitude and a higher frequency for similar values of Q.

During oscillations there existed a phase difference between upstream and downstream pressure signals, the latter being in advance.

6 Preliminary Verification of FSI in LS-DYNA

In the earlier versions of LS-DYNA (pre-version 950d) the numerical treatment of a flowing fluid was observed to be highly inaccurate. The extent of the error was such that the defined value of viscosity in the LS-DYNA model appeared to be completely ignored by the code. Several analyses were performed in order to determine the source of LS-DYNA's inaccuracies and concerns regarding the quantitative relationship between velocity gradient, shear stress, strain rate and viscosity were reported to LSTC. Consequently the fluid formulations in LS-DYNA were reprogrammed by LSTC for version 950d. Since earlier versions of the code contained inaccuracies the analyses run with these early versions are not included here. The main sections of this thesis only deal with analyses run using version 950d.

It must be remembered that the finite element method is used to solve a mathematical model that represents an idealisation of the actual physical problem considered. The governing equations of this mathematical model cannot be solved in closed analytical form. However, an approximation of the exact solution can be obtained, usually, with very high accuracy using finite element methods.

The accuracy of a solution increases with refinement of the mesh of elements and refinement of the time-step, the latter being a function of the former in an explicit analysis. However, both mesh density and the size of time-step have a massive influence on the CPU time required for a solution. For an accurate computational solution to be achieved it must exhibit some level of mesh independence as well as a certain degree of time-step independence. The degree of mesh and time-step independence depends on the degree of error that is acceptable within the solution. Therefore the notion of convergence must be introduced. A convergence study can be used to determine the most coarse mesh allowable or largest time-step allowable, that produces a solution within the tolerance of error; or it may be used to quantify the level of uncertainty within a particular numerical model.

The first step in any finite element analysis must therefore be the determination of mesh and time-step size for the best balance of accuracy and CPU solution time. Due to the complexity of the collapsible-tube model the initial determination of suitably accurate values of the above was made using a small test model.

6.1 Mesh Independence

6.1.1 The Test Model

A three-dimensional fluid control volume of 30mm x 300mm was modelled with reservoirs at both short ends. The control volume was split into various mesh densities, which utilised elements of cubes of 0.5mm edge-length (36000 solid elements), 1mm edge length (9000 elements), 2mm edge-length (2250 elements) and 5mm edge-length (360 elements).

The control volume was initially full and the fluid was static. One of the long sides was defined as a no-slip wall and the other a moving boundary with an applied velocity of 1m/s. The reservoirs were defined as datum pressures (0 MPa). The faces of the solid elements were defined as slipping walls effectively rendering the model two-dimensional. The Euler (main fluid) and ambient Euler (fluid reservoir) formulation were tested with the first order donor cell advection algorithm. A depiction of the numerical model is shown in Figure 6.1.

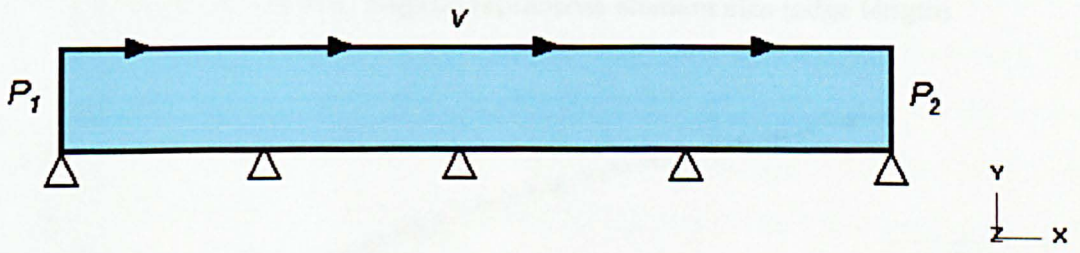

Figure 6.1. Two-dimensional moving wall model for testing of the fluid viscosity in LS-DYNA.

The properties of the fluid were $\rho_f = 1\text{x}10^3$ kg/m^3 (water), $\mu = 1\text{x}10^{-3}$ Pa s (water) and c = 10 m/s (the value of c for water is 1483 m/s). A further study was also carried out using a larger fluid viscosity of $\mu = 1\text{x}10^{-1}$ Pa s; this arbitrary fluid is referred to herein as oil.

6.1.2 Results

In both analyses, water and oil, a finer mesh allowed a smoother, more accurate, velocity profile and hence velocity gradient to develop. The resulting fluid velocity profile half way (150mm) along the tube was recorded after the steady state had been

reached. The velocity profile results are shown in Figure 6.2 and Figure 6.3 for the various mesh densities for water and oil respectively.

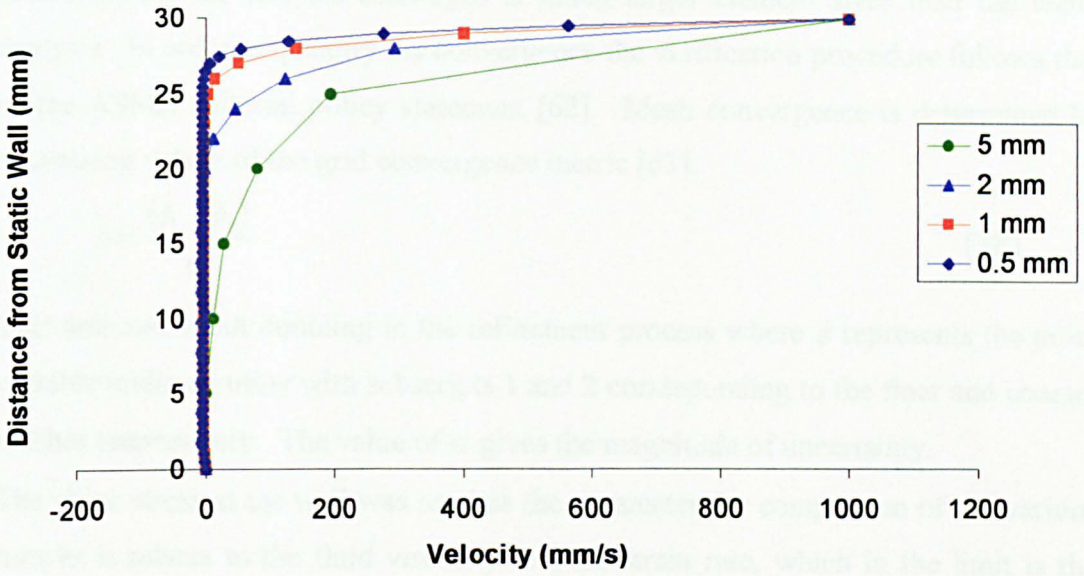

Figure 6.2 Velocity profile perpendicular to moving wall for Euler and Ambient Euler formulation in LS-DYNA v950d for a fluid with the properties of water $\mu = 1x10^{-3}$ Pa s, $\rho_f = 1x10^3$ kg/m^3, $c = 10$ m/s. Legend represents element size (edge length)

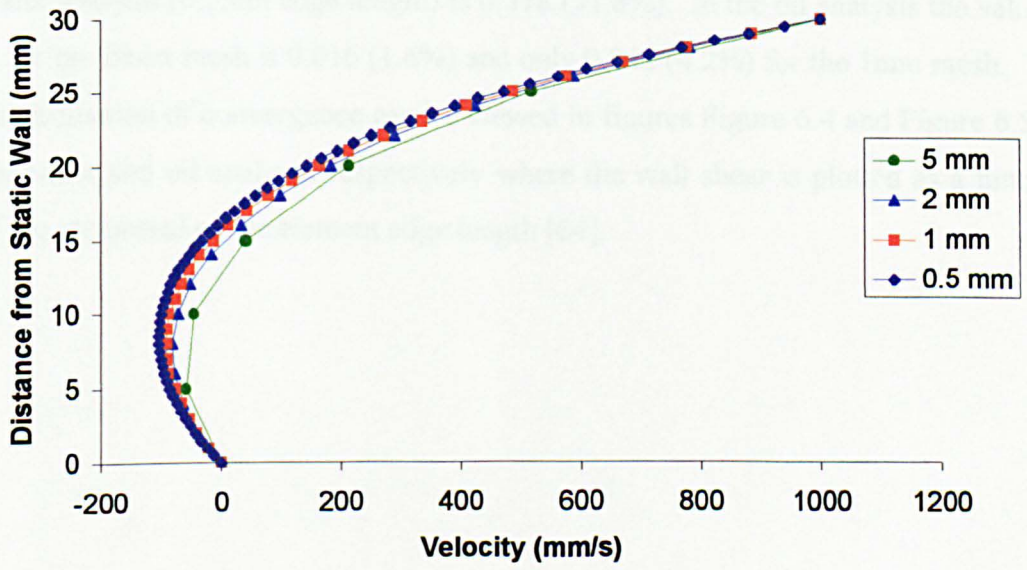

Figure 6.3 Velocity profile perpendicular to moving wall for Euler and Ambient Euler formulation in LS-DYNA v950d for a fluid with $\mu = 1x10^{-1}$ Pa s, $\rho_f = 1x10^3$ kg/m^3, $c = 10$ m/s. Legend represents element size (edge length)

It can be seen from Figure 6.2 and Figure 6.3 that the velocity gradient next to the wall gets larger and converges towards an exact solution as the mesh gets finer. However, the oil analysis converges at much larger element sizes than the water analysis. In order to quantify the convergence the verification procedure follows that of the ASME editorial policy statement [62]. Mesh convergence is determined by decreasing values of the grid convergence metric [63].

$$\in = \frac{(\phi_1 - \phi_2)}{\phi_1} \tag{28}$$

This assumes mesh doubling in the refinement process where ϕ represents the point variable under scrutiny with subscripts 1 and 2 corresponding to the finer and coarser meshes respectively. The value of $\in$ gives the magnitude of uncertainty.

The shear stress at the wall was used as the parameter for comparison of the various runs as it relates to the fluid viscosity and the strain rate, which in the limit is the same as the velocity gradient. This parameter was used to quantify the convergence of the solution.

In both analyses the value of $\in$ fell for each progressive refinement of the mesh indicating that the solution was convergent. The value of $\in$ for the finest mesh in the water analysis (0.5mm edge length) is 0.318 (31.8%). In the oil analysis the value of $\in$ for the finest mesh is 0.016 (1.6%) and only 0.042 (4.2%) for the 1mm mesh. This quantification of convergence can be viewed in figures Figure 6.4 and Figure 6.5 for the water and oil analyses respectively where the wall shear is plotted as a function of the reciprocal of the element edge length [64].

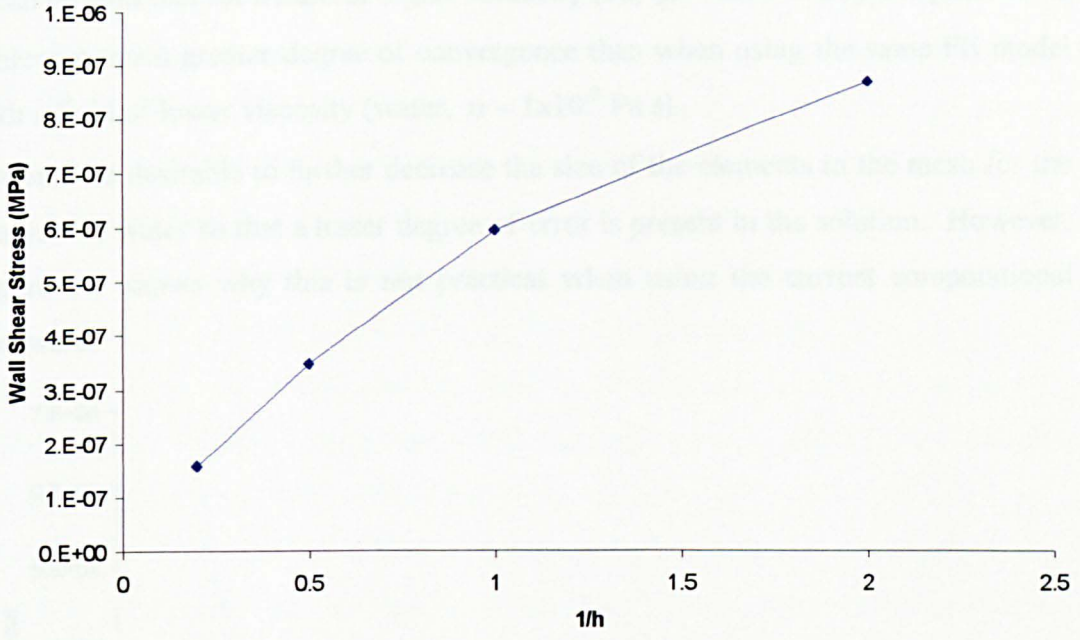

Figure 6.4 Wall shear stress of the finite element solution as the element size h is decreased for the analysis of water.

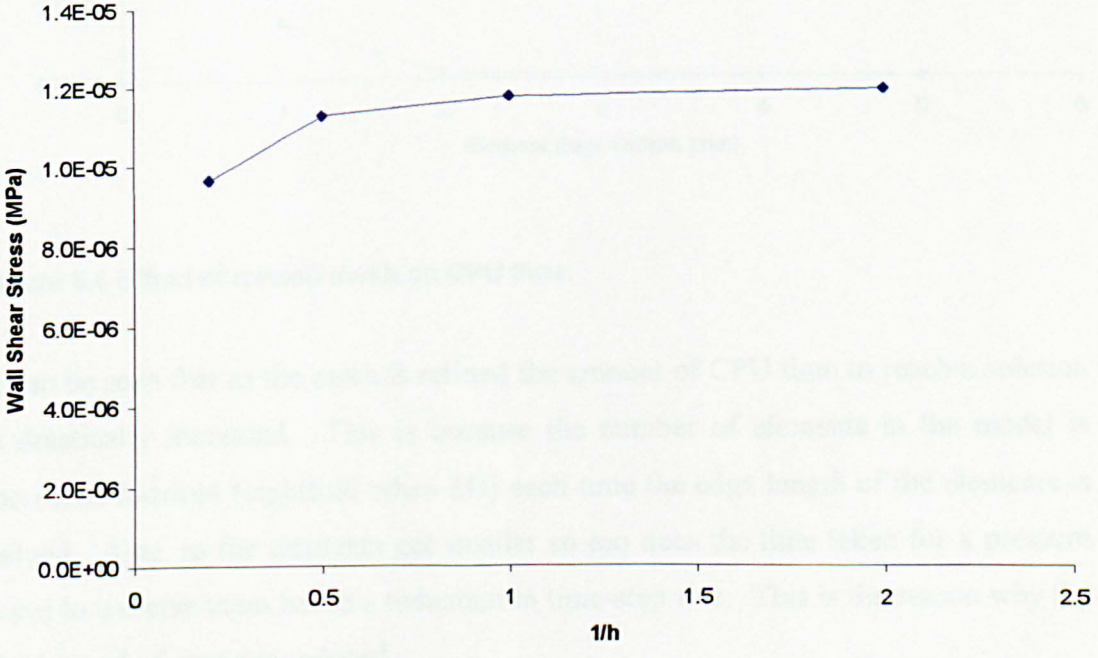

Figure 6.5 Wall shear stress of the finite element solution as the element size h is decreased for the analysis of oil. The plot shows convergence as the mesh is refined.

It can be seen that for a fluid of higher viscosity (oil, $\mu = 1x10^{-1}$ Pa s) it is possible to achieve a much greater degree of convergence than when using the same FE model with a fluid of lower viscosity (water, $\mu = 1x10^{-3}$ Pa s).

It would be desirable to further decrease the size of the elements in the mesh for the analysis of water so that a lesser degree of error is present in the solution. However, Figure 6.6 shows why this is not practical when using the current computational hardware.

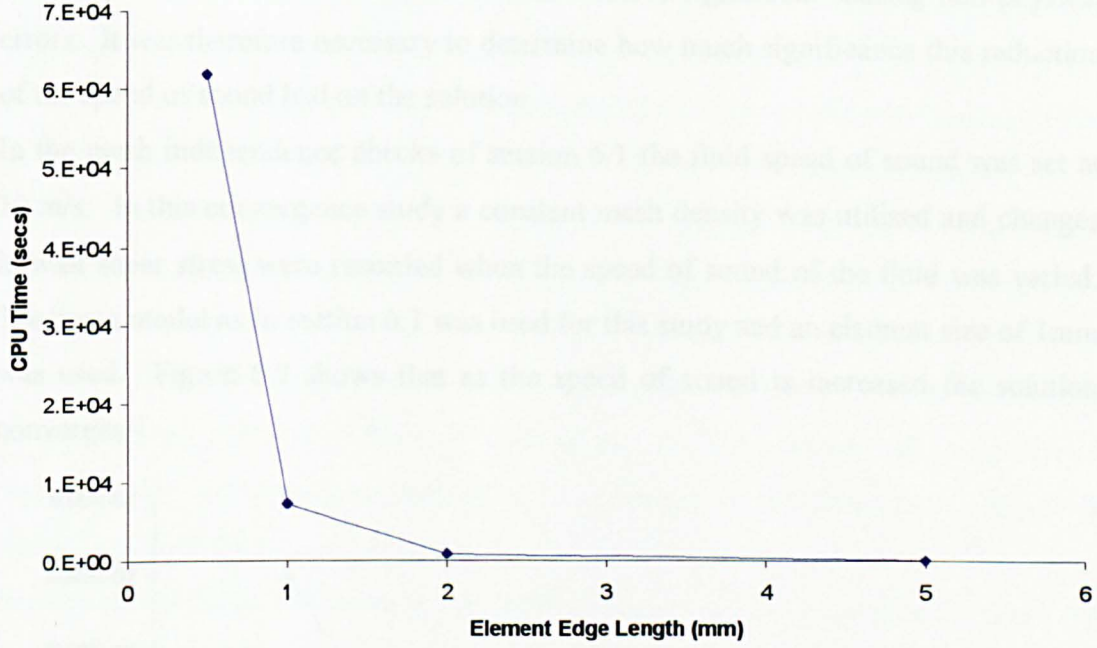

Figure 6.6 Effect of refined mesh on CPU time.

It can be seen that as the mesh is refined the amount of CPU time to reach a solution is drastically increased. This is because the number of elements in the model is increased fourfold (eightfold when 3D) each time the edge length of the elements is halved. Also, as the elements get smaller so too does the time taken for a pressure wave to traverse them hence a reduction in time-step size. This is the reason why the fluid speed of sound is reduced.

6.2 Time-Step Independence

It has already been discussed in section 4.1.3 that the time-step of an explicit technique is determined by the Courant limit. In other words the time-step is automatically set as to provide for the most accurate stable solution possible for any

particular mesh. The solution of the collapsible-tube models was greatly hindered by the high CPU time cost associated with the small time-step of the explicit technique. Because of this it was necessary to use some form of speed-up technique (as discussed in section 4.1.3). Since the effects of compressibility of the fluid in this particular analysis were deemed to be negligible the lowering of the fluid speed of sound, in order to raise the time-step, was deemed a necessary step in order to gain acceptable CPU run times. However, in doing this the compressibility of the fluid in the computer model is increased and could become significant causing non-physical errors. It was therefore necessary to determine how much significance this reduction of the speed of sound had on the solution.

In the mesh independence checks of section 6.1 the fluid speed of sound was set at 10 m/s. In this convergence study a constant mesh density was utilised and changes in wall shear stress were recorded when the speed of sound of the fluid was varied. The same model as in section 6.1 was used for this study and an element size of 1mm was used. Figure 6.7 shows that as the speed of sound is increased the solution converges.

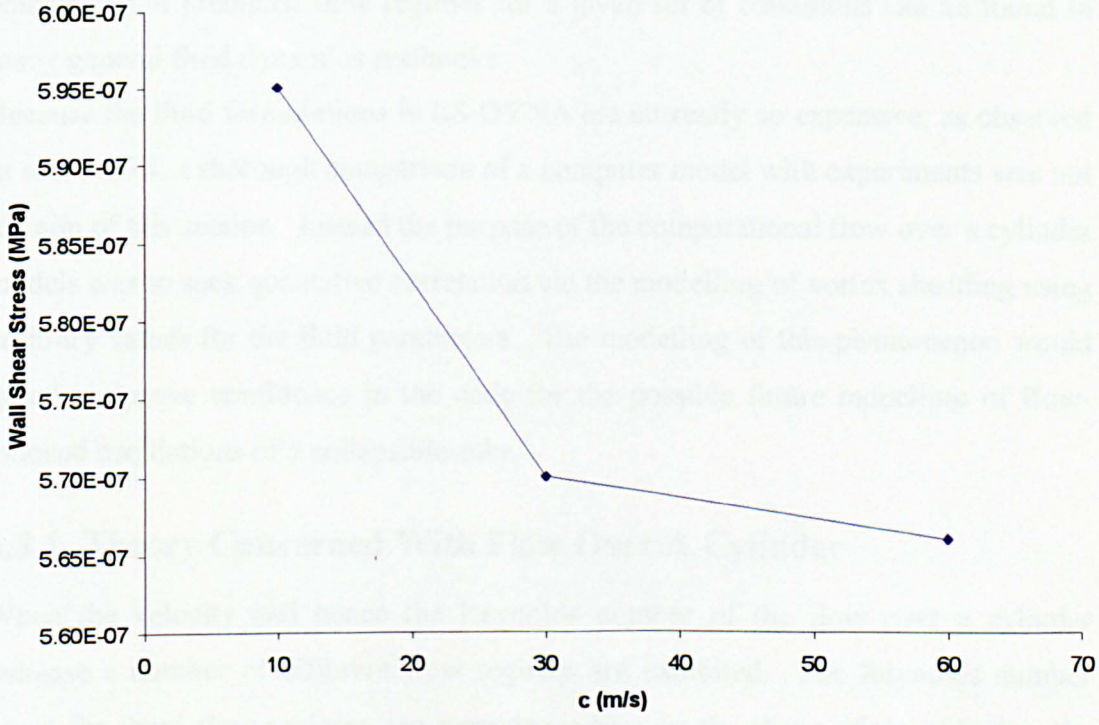

Figure 6.7 Wall shear stress of the finite element solution as fluid speed of sound is reduced.

The quantification of this convergence was carried out in a similar manner to that of the mesh independence checks. The value of wall shear stress was found to differ by 0.7% between c = 30 and 60 m/s and by 5.1% between c = 10 and 60 m/s.

6.3 Flow Over A Cylinder

The phenomenon of fluid flow over a cylinder provides a good test of a numerical fluid dynamics code. It has been used to test for the accuracy of a numerical codes ability to model viscous flow and particularly the transition from viscous-governed to inertia-governed flow and the onset of flow induced oscillations. More recently this testing has been extended to the numerical modelling of the vortex-induced vibration of the cylinder [65, 66] where the ALE method has been successfully employed.

For cylinders of high aspect ratio in uniform flow the geometry can be regarded as two-dimensional and defined by a very small number of parameters. The wealth of published data and reliability of the predictive equations make the two-dimensional flow over a cylinder model attractive as a comparison tool since no experiments need be performed. This is particularly true of the circular cylinder where predictive equations and predicted flow regimes for a given set of conditions can be found in many general fluid dynamics textbooks.

Because the fluid formulations in LS-DYNA are currently so expensive, as observed in section 6.1, a thorough comparison of a computer model with experiments was not the aim of this section. Instead the purpose of the computational flow over a cylinder models was to seek qualitative correlation via the modelling of vortex shedding using arbitrary values for the fluid parameters. The modelling of this phenomenon would greatly improve confidence in the code for the possible future modelling of flow-induced oscillations of a collapsible-tube.

6.3.1 Theory Concerned With Flow Over A Cylinder

When the velocity and hence the Reynolds number of the flow over a cylinder increase a number of different flow regimes are exhibited. The Reynolds number given for these flow regimes can vary depending on the shape of the cylinder, the turbulence in the flow before the cylinder, and due to other solid objects in the flow near the cylinder. The following description is concerned with flow over a circular cylinder. Experimentally determined values of Reynolds number at the transition

from one flow regime to the next can be found in many textbooks and may vary depending on the source data. The values given here are taken from Massey [67].

At Reynolds numbers of up to Re ≈ 0.5 the flow does not exhibit any separation from the cylinder since inertia effects are (Figure 6.8(a)). Between Re ≈ 2 and Re ≈ 30 flow separation occurs creating two eddies behind the cylinder which rotate in opposite directions, their energy being maintained by the separated flow (Figure 6.8(b)). As the Reynolds number increases these eddies increase in length (Figure 6.8(c)) and with a Reynolds number between Re ≈ 40 and Re ≈ 70 periodic transverse fluctuations of the flow can be seen after the cylinder, as the arrangement becomes unstable (Figure 6.8(d)).

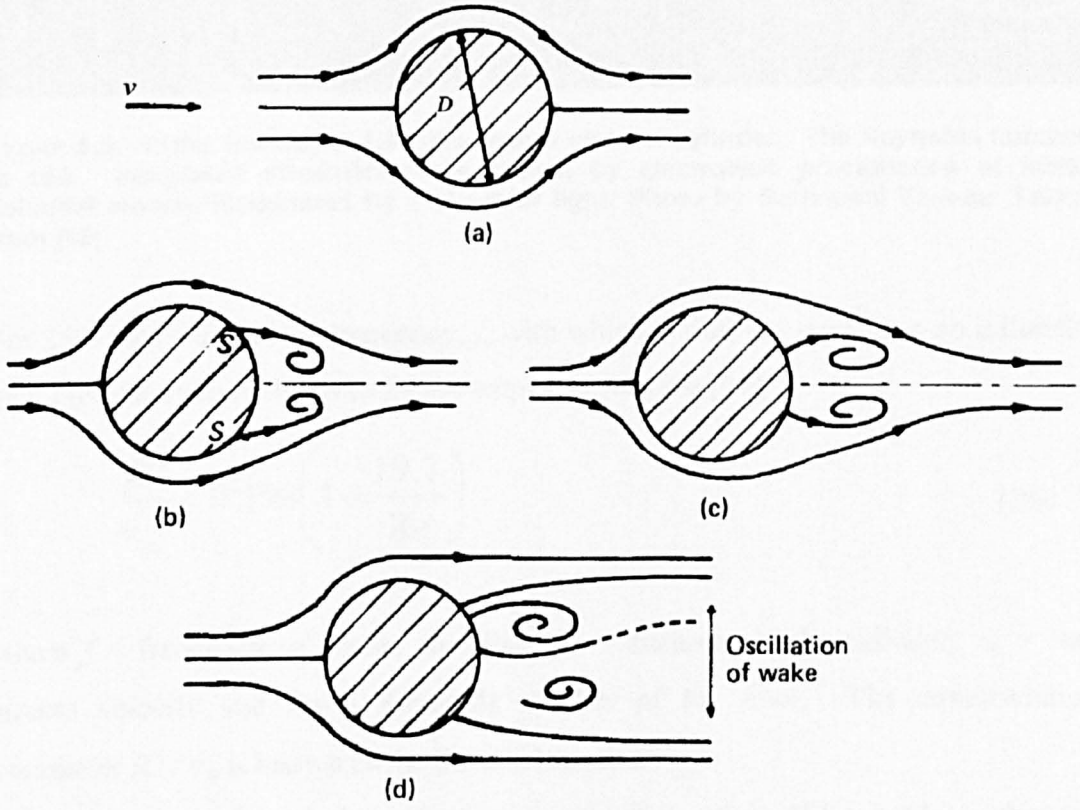

Figure 6.8. Flow Over a Cylinder at Various Reynolds Numbers; (a) Re ≈ 0.5, (b) 2 < Re < 30, (c) 2 < Re < 30, (d) 40 < Re < 70; Figure from Massey [67]

At a Reynolds number greater than about 90, for unconfined flow, eddies can be seen separating from the cylinder and being carried off downstream. Eddies separate alternately from the top and bottom of the cylinder and form two rows of vortices in the wake. This arrangement is known as a Vortex Street or von Karman Street and is shown in Figure 6.9.

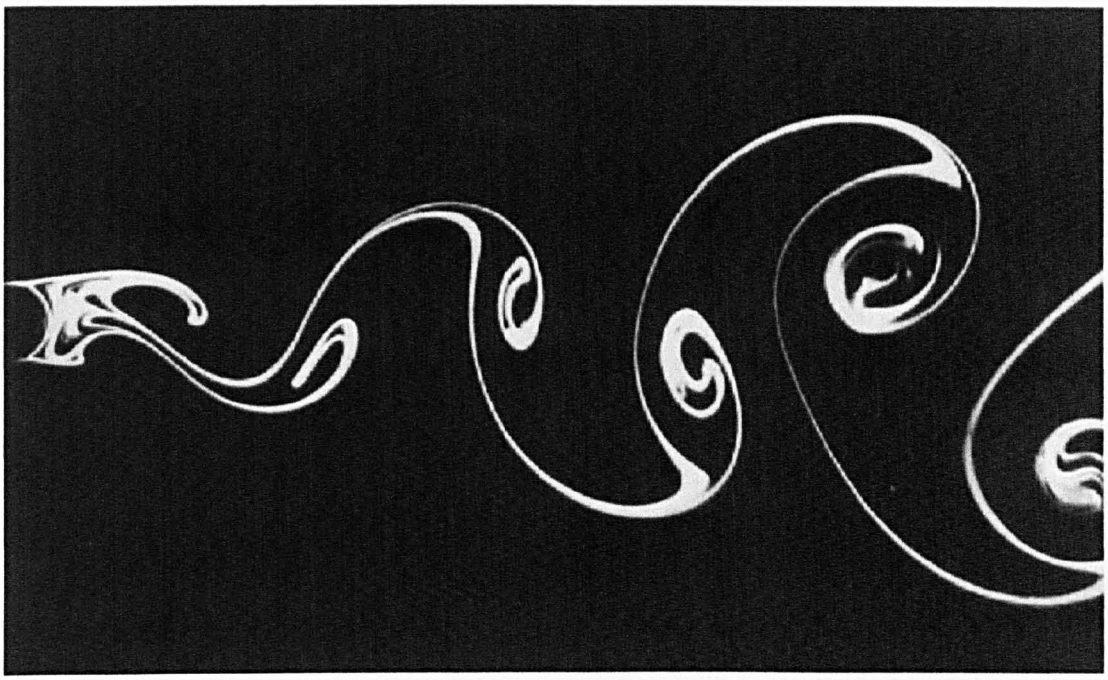

Figure 6.9. Water flowing at 1.4 cm/s over a circular cylinder. The Reynolds number is 140. Integrated streamlines are shown by electrolytic precipitation of white colloidal smoke, illuminated by a sheet of light. Photo by Sadatoshi Taneda. Taken from [68]

For $250 < \mathrm{Re} < 2\mathrm{x}10^5$ the frequency, f, with which eddies are shed from an infinitely long circular cylinder is given by the empirical formula [67]

$$\frac{fD}{v_\infty} = 0.198\left(1 - \frac{19.7}{\mathrm{Re}}\right) \tag{29}$$

where f = frequency of vortex shedding, D = diameter of the cylinder, v_∞ = free stream velocity and Re = Reynolds number of the flow. The dimensionless parameter fD / v_∞ is known as the Strouhal number.

By analysing this formula it can be seen that for high values of Reynolds number the right-hand side of the formula can be approximated to 0.198. The frequency of vortex shedding is then dependent on cylinder diameter and free stream velocity only.

6.3.2 LS-DYNA Model Of Flow Over A Cylinder

6.3.2.1 Model Construction

An arbitrary fluid flow domain was constructed of 8257 solid elements. The fluid domain had a circular hole in it, of diameter 4 m, which acted as the cylinder. The domain was 40 m long in the flow direction and 20 m perpendicular to the flow. The mesh was constructed three-dimensionally with a depth of 0.8 m. The resolution of the mesh was finer near the cylinder wall as shown in Figure 6.10. Ambient Eulerian elements were placed at the left and right edges of the control volume to act as reservoirs. The nodes situated on the boundary of the cylinder were fully constrained in all directions so that they acted like a no-slip wall. The front and rear faces of the solid elements were defined as slipping boundaries which allowed fluid to slide across them with no shear stress but would not allow any fluid to penetrate them. This effectively rendered the model two-dimensional.

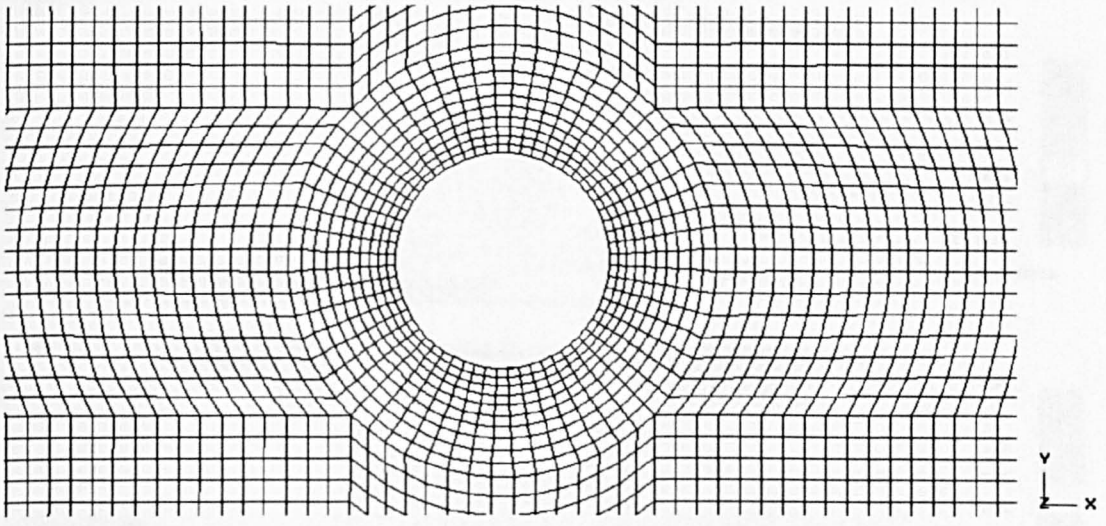

Figure 6.10. Finite element mesh close to the cylinder of the flow over a cylinder model for LS-DYNA

Velocity (displacement with respect to time) boundaries were defined at the inlet reservoir interface and the upper and lower walls. The velocities were purely in the x-direction and did not allow movement of fluid in y or z. The fluid had arbitrary properties of $\rho_f = 75$ kg/m^3, $\mu = 100$ Pas and $c = 340$ m/s.

Four values of Reynolds number were assessed with the above model. These were Re = 15, 75, 150 and 300, which utilised free stream velocities of 5, 25, 50 and 100 m/s respectively.

6.3.2.2 Results

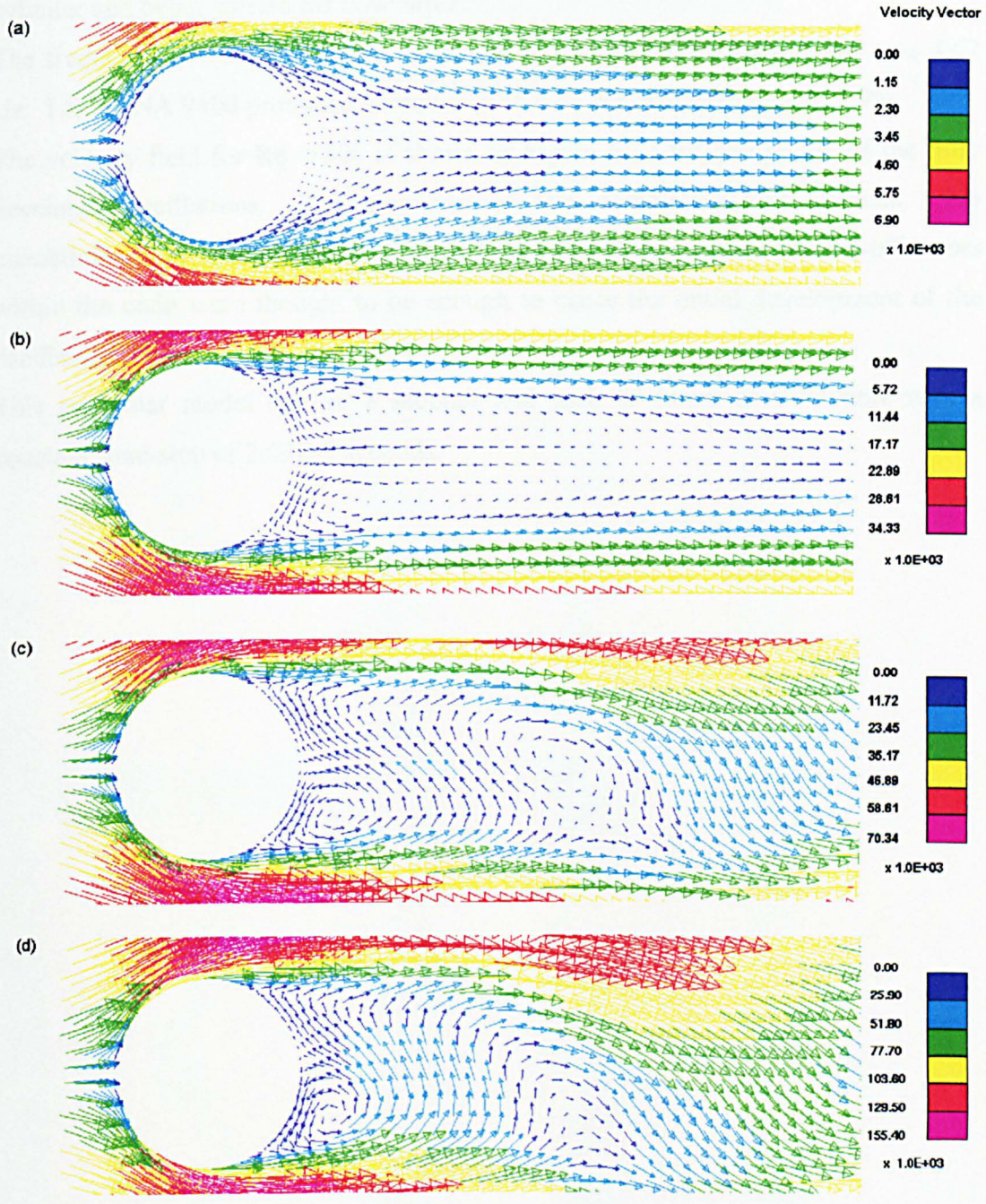

Figure 6.11. Fluid velocity vectors (mm/s) resulting from flow over a cylinder at (a) Re = 15, (b) Re = 75, (c) Re = 150 and (d) Re = 300

The fluid response of the LS-DYNA models in Figure 6.11 agrees with the flow regimes expected at such Reynolds numbers as shown in Figure 6.8. At Re = 15 there is separation of the flow and two counter-rotating eddies can be seen after the cylinder. At Re = 75 these eddies have increased in length and the flow pattern

remains steady. At Re = 150 and 300 the vortices can be seen detaching from the cylinder and being carried off downstream.

The frequency of vortex shedding predicted by equation 29 for Re = 300 was 4.62 Hz. LS-DYNA 940d produced a frequency of 4.44 Hz, a discrepancy of 3.9%.

The velocity field for Re = 300 is shown in Figure 6.12 for one period of the fully developed oscillations. This phenomenon was completely flow induced. No instabilities were introduced in order to create this flow regime. Round-off errors within the code were thought to be enough to cause the initial development of the oscillatory flow.

This particular model ran for 8 seconds and took 45 hours of CPU time with a constant time-step of 2.03E-5 seconds.

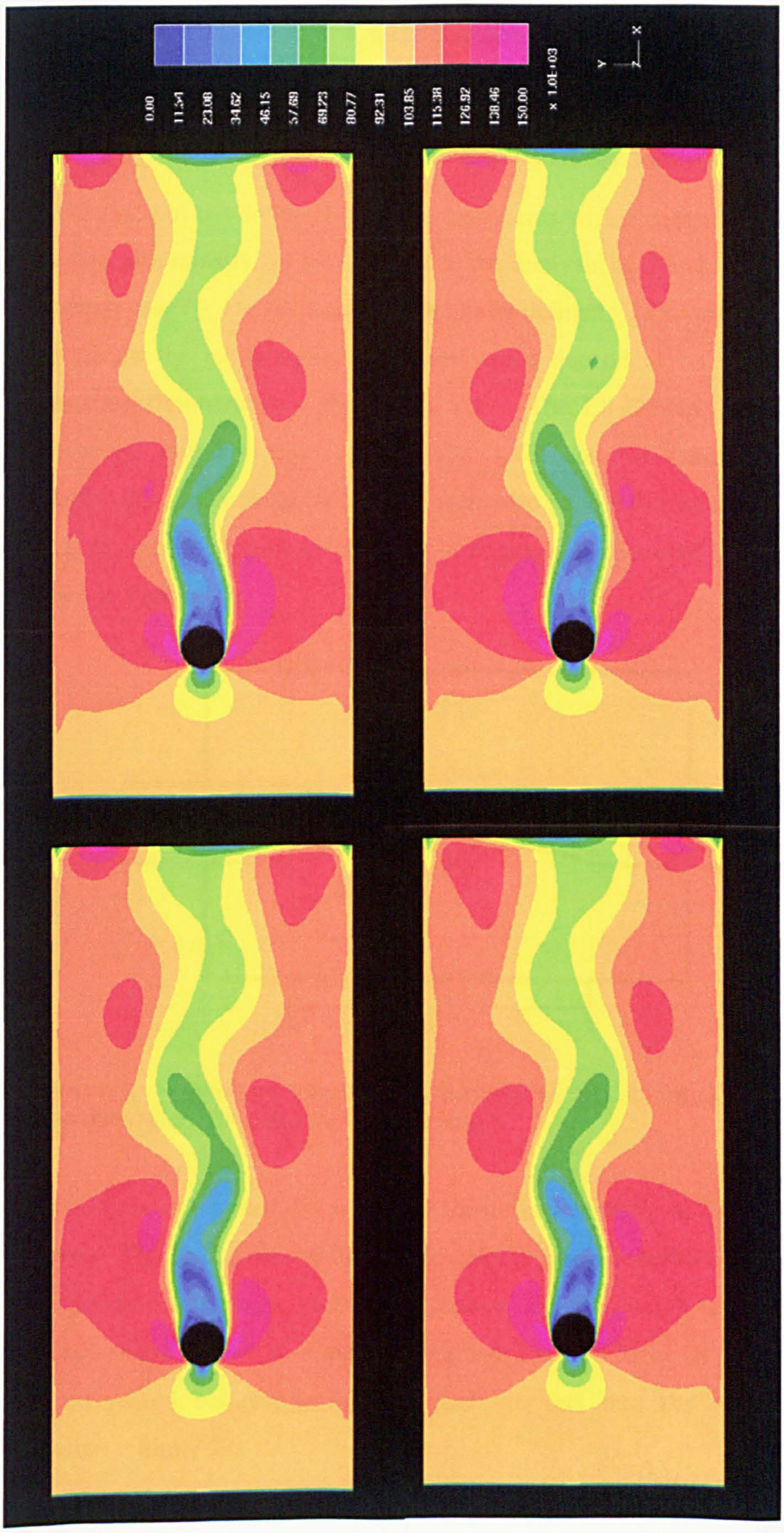

Figure 6.12 Vortex shedding at Re = 300. Contours show velocity (mm/s)

7 Modelling of the Collapsible-Tube Using LS-DYNA

7.1 Construction and Development of the LS-DYNA Model

Comparison of the collapsible-tube experiments with a computational model with its inherent size constraints was limited to the analysis of the collapsible section alone. In which case P_1, P_2, P_E and Q needed to be defined. This was acceptable for steady flow since the experiments performed were dependent on the flow, Q, and the pressure differences P_1 - P_2 and P_E - P_2. The LS-DYNA model also needed to include an initial tension in the tube walls and the residual stresses due the manufacture and packing since these were also parameters that affected the results of the experiments. A picture of the main computational model boundary conditions is shown in Figure 7.1.

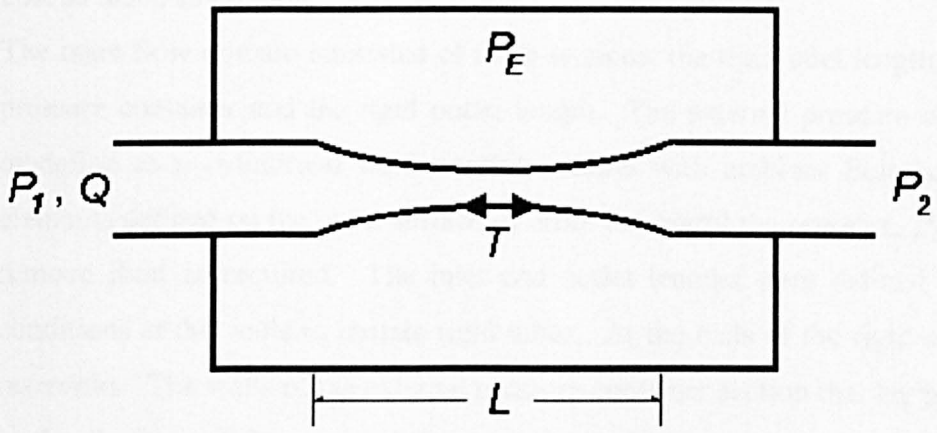

Figure 7.1. Boundary conditions required in the computational model of the collapsible-tube. T = tension, L = tube length

This set-up was numerically modelled three-dimensionally in HYPERMESH for LS-DYNA. The important variables calculated by the computational model were the tube geometry and stress, local fluid pressure, and the fluid flow patterns.

Parameters not shown in Figure 7.1 include the difference in diameter of the rigid and unstressed collapsible sections and the fact that the collapsible tube was modelled initially flat.

7.1.1 Fluid and Structure Discretization

The fluid discretization consisted of 79956 eight-noded solid elements and was split into four parts; these were the inlet, outlet and external reservoirs and the main flow domain. The size of the fluid elements was determined by the mesh independence checks carried out in section 6.1 and also by CPU constraints. It was accepted that the sizes of elements were subjected to a significant uncertainty as discussed in section 6 and as such the model was not expected to produce quantitatively accurate results. The element edge lengths normal to the flow did not anywhere exceed 1mm and were no greater than 0.5mm where tube wall contact was observed in the experiments. The edge lengths parallel with the flow were 1mm in the area where collapse was expected and at the transition from collapsible to rigid tube. In the main part of the rigid tube and in the centre section of the collapsible-tube the edge lengths parallel with the flow reached a maximum of 3.25mm in order to reduce CPU cost as much as possible.

The main flow domain consisted of three sections: the rigid inlet length, the external pressure container and the rigid outlet length. The external pressure container was modelled as a cylindrical fluid control volume with ambient Eulerian (reservoir) elements defined on the outer surface in order to control the pressure, P_E, and add or remove fluid as required. The inlet and outlet lengths were defined with no-slip conditions at the walls to imitate rigid tubes. At the ends of the rigid sections were reservoirs. The walls of the external pressure container section that lay perpendicular to the direction of flow were defined as walls with the slip condition. This allowed fluid to escape from the corners of this domain as the tube collapsed. Early attempts at running the model with the no-slip condition at this wall resulted in volumes of fluid being trapped and a non-physical bulge resulting in the tube.

The three reservoirs, inlet, outlet and external were given pressures P_1, P_2 and P_E respectively. Pressure differences $P_1 - P_2$ and $P_E - P_2$ were measured from the experiment in section 5 and were used as boundary conditions for the computational model. The flow rate, Q, was converted into an average velocity and applied as a flat profile at the inlet reservoir interface.

It was not practical to model the entire experimental system with R_1, R_2 and upstream and downstream reservoir pressures. The rigid inlet and outlet were therefore modelled substantially shorter than desirable. This was mainly due to the fine mesh

resolution in the fluid mesh cross-section. Increasing the inlet and outlet lengths would not only increase CPU by the addition of many more elements but would also increase the time taken for the model to settle, thus adding more CPU time onto an analysis. In the experiment P_1 and P_2 were measured 180mm upstream and downstream of the collapsible section. In the LS-DYNA model this distance was 19.5mm. However a model utilising inlet and outlet lengths of 37.5mm was also constructed so that an indication of the effect of the shortened inlet and outlet could be gained.

The collapsible tube structure was represented in the flow field using 9840 four-noded Belytschko-Lin-Tsay shells. These were coupled to the fluid enabling FSI.

The fluid and structural parts used in the LS-DYNA model can be seen in Figure 7.2.

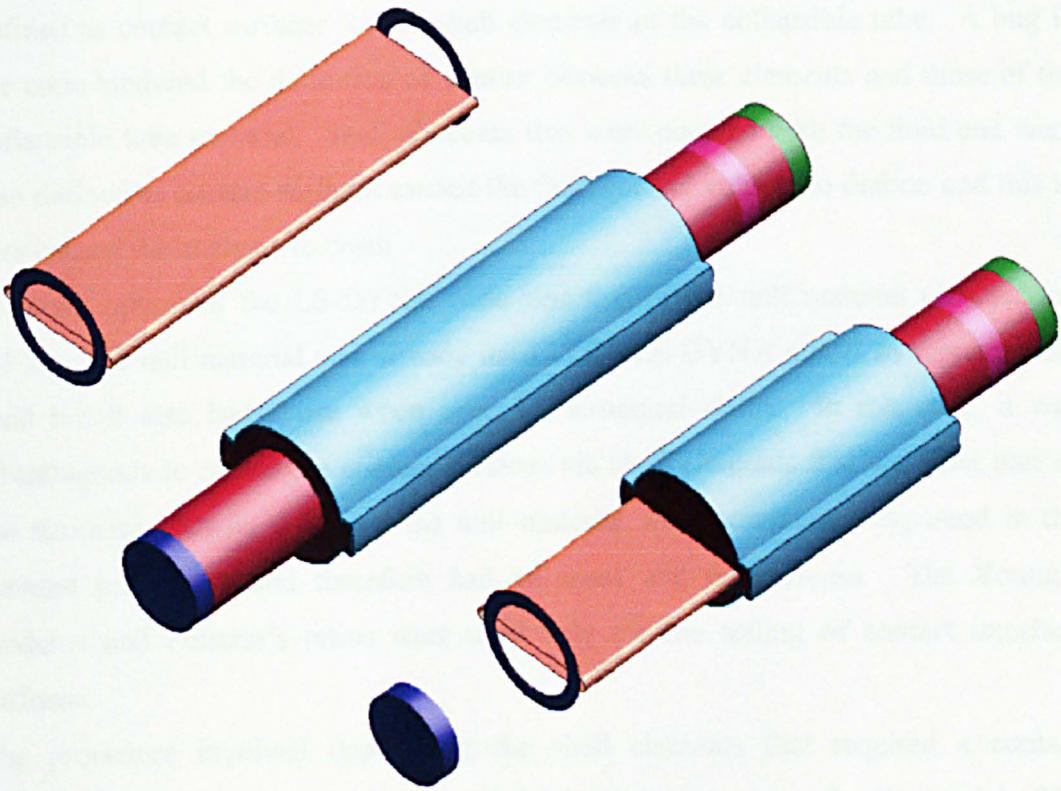

Figure 7.2. Structural (left), fluid (middle) and coupled (right) parts of the LS-DYNA model. The structural parts include the flat tube and the contact annuli, the fluid parts include the main flow domain and the reservoirs. The coupled picture shows half of the fluid part blanked.

7.1.2 Contact

Another condition necessary for an accurate model was that of the contact between the upper and lower walls of the tube and between the collapsible tube and the faces of the inlet and outlet tubes.

The tube wall was already subjected to coupling with the fluid elements. It emerged that no further definition was needed to define contact between the upper and lower walls. The FSI coupling acted as if self-coupling of the structure had already been defined.

It was seen in the experiments that at larger values of P_E the tube material pressed against the faces of the inlet and outlet. These faces were modelled as annuli constructed of 400 rigid shell elements each. The nodes of the rigid shells were defined as contact surfaces for the shell elements of the collapsible tube. A bug in the code hindered the definition of contact between these elements and those of the collapsible tube material. Shell elements that were coupled with the fluid and were also defined as contact surfaces caused the fluid control volume to deform and this in turn caused the analysis to crash.

A useful option of the LS-DYNA code was that of the null material (see section 4.1.2). The null material was already used in the LS-DYNA model to represent the fluid but it also had a use when used for structural shells. In this case, it was advantageous to model the contact surfaces via shell elements that were not part of the structure. Shells that used the null material were completely bypassed in the element processing and therefore had no mass and no stiffness. The Young's modulus and Poisson's ratios were used only for the setting of contact interface stiffness.

The procedure involved duplicating the shell elements that required a contact definition. These elements were then defined as separate parts of null material. The nodes of the null shells and the original shells were then combined so that the null shells were bonded to the originals. Contact surfaces were then defined on the null shells. Since the null shells were completely bypassed in the element processing there was no extra mass or stiffness to consider and the collapsible tube could deform as normal. However, when the null shells came into contact with the rigid nodes of the inlet and outlet faces, the movement of the null shells was halted which in turn

halted those shells that comprised the tube structure. This method of contact avoided any problems concerned with the definition of contact surfaces within fluids.

7.1.3 Preforming The Tube

The technique used in the LS-DYNA solution was to model the tube in its flat state and to form it into a cylindrical shape at the start of the analysis. This was done to imitate the action of stretching the tube onto the rigid inlet and outlet sections. This needed to be modelled since the stresses in the tube wall caused by the change of shape from flat to cylindrical were found to be a significant factor in determining the plane of collapse of the tube.

Preforming was accomplished by applying displacement vectors to each row of nodes on the tube to move them to a new position on the surface of an imaginary circular cylinder. The technique for applying the displacement loads is given in appendix D. When preforming was complete the displacement loads were removed with the exception of the end loads which were maintained in order to model the rigid/deformable tube transition. The tube then acted as if stretched onto the rigid inlet and outlet and the material between inlet and outlet was free from any constraints except its coupling to the fluid. The process of preforming can be seen in Figure 7.3.

Figure 7.3. Preforming process for the collapsible tube. (a) shows the tube in its undeformed 'flat' state; (b) shows the tube after the nodes have been displaced to the surface of the imaginary circular cylinder; and (c) shows the tube just after the displacement loads were removed.

The fluid-structure coupling was activated just after the nodes had been moved to the cylinder surface and just before the displacement loads were removed. The coupling of the tube to the fluid damped out the effect of the instantaneous release of the now stressed tube. Without the fluid coupling the shells hourglassed just after release.

The need to model the preforming of the tube was responsible for the development of several techniques for the construction of keyword data and translation of data from pre-processor to LS-DYNA input file. It was also responsible for some of the more drastic refinements to the collapsible-tube model in terms of mesh size and LS-DYNA technique.

7.1.4 Tube Tension

The technique for applying a tension to the tube required manipulation of the existing element data of the tube. This is included in appendix E.

In this case it was not a tension that was applied but a "compression" since in the experiment a 67 mm tube was mounted in a gap of 65 mm. The extra 2 mm was

taken up by the radial tension and subsequent axial tension caused by the mounting points being of a larger diameter than that of the undeformed tube. A stress was calculated using the following formula:

$$\left(\frac{L}{L_0}-1\right)E=\sigma \tag{30}$$

where L = distance between inlet and outlet rigid parts, L_0 = required unstressed length of tube, E = Youngs Modulus, σ = initial axial stress.

In terms of the experiment, L_0 was the length of unstressed tube mounted between an inlet and outlet of length L apart. In LS-DYNA the tube was modelled with a length L so that it could be relatively easily pre-formed from the flat state to the cylindrical state. This length, L, of tube was given an initial stress, σ, so that if released from all boundary conditions it would reform to a length of L_0.

7.1.5 Material Properties

The fluid properties were ρ_f = 998 kg/m^3 (water) and μ = 0.001 Pa s (water). The speed of sound in the fluid was reduced from 1483 m/s to 10 m/s in order to raise the time-step size and achieve practical solution times. The error associated with this approximation was found to be around 5% in section 6. A further model utilising a speed of sound of 30 m/s was run in order to check the actual level of error.

The computationally cheap linear elastic material model was used in LS-DYNA as an approximation of the rubber tube. Some alterations were needed to the experimentally measured properties (from section 5.1.3) in order to gain the correct collapse profile. These changes are explained in more detail in section 7.2.3. These new material properties were used in the knowledge that the stresses in the tube would be of a different magnitude than if the experimentally measured properties were used.

7.2 Calibration of Tube Material Using No-Flow Simulations

The zero-flow models were solved, essentially, to test the response of the linear elastic material in LS-DYNA and its interaction with the coarser than desirable fluid mesh. The use of the linear elastic material model to act as latex rubber was

desirable due to its computing economy. However, caution was necessary since the numerical modelling of rubber has long been a stumbling block for FE analysts. Compared with finite element analysis of other engineering materials, elastomers exhibit three problems:

(i) the occurrence of large deformations

(ii) near-incompressibility of the materials

(iii) non-linear force/deflection behaviour

Of these the last is still unresolved and there is no generally accepted, validated non-linear elasticity model for elastomers at high strains. However, it was predicted that the strains in this case would not require a non-linear analysis. Setting the Poisson's ratio to 0.49 instead of 0.5 eliminated the problems associated with the incompressibility of rubber.

LS-DYNA offered a two-parameter Mooney-Rivlin rubber material model. The stress/strain data needed by this model could be included as experimental curve data. However, the use of such a material model was found to take up to eight times as much CPU time as the linear elastic model rendering it highly undesirable in this analysis.

7.2.1 Model Properties

The real material properties of the tube described in section 5.1.3 were used in LS-DYNA with the linear elastic material model ($\rho = 920$ kg/m^3, E = 1.3 MPa, $\nu = 0.49$, w = 0.35, L = 65 mm). The fluid speed of sound was lowered from 1483 m/s to 10 m/s.

Tubes with unstressed lengths of L_0 = 63, 65 and 67 mm were modelled by applying initial axial stresses of 0.0413, 0 and –0.0388 MPa respectively to an initial length, L, of 65 mm.

P_1 and P_2 were prescribed with 0 pressure and P_E was prescribed with a positive pressure of 40 cmH_2O applied after the tube had been pre-formed.

7.2.2 Results

Figure 7.4 shows the collapse profile of a tube of 65 mm undergoing a transmural pressure of –40 cmH_2O. The cross-sectional profiles can be seen in Figure 7.5.

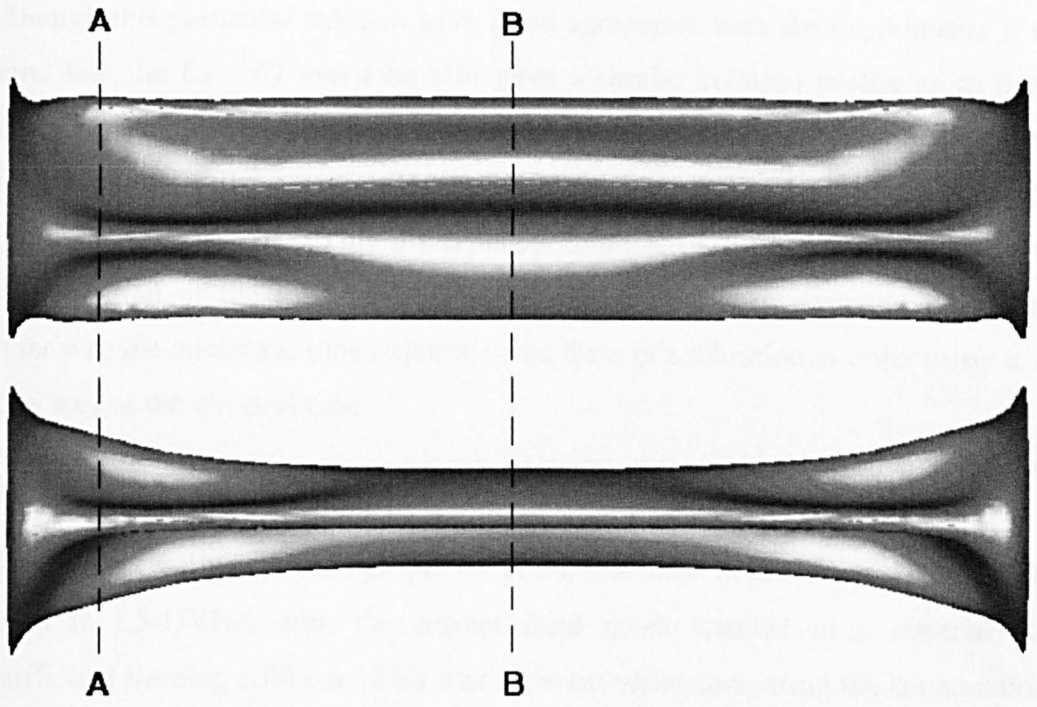

Figure 7.4. Top and side profiles of the L_0 = 65mm collapsible tube subjected to a transmural pressure of –40 cmH_2O.

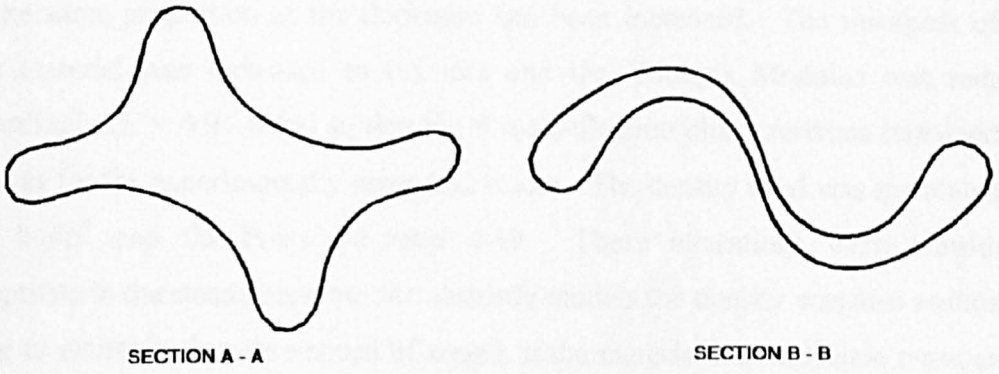

Figure 7.5. Cross-sectional profiles corresponding to the sections defined in Figure 7.4.

It can be seen that the collapse profile is qualitatively the same as that observed in the experiments for an unstressed tube length of 65 mm (Figure 5.7(b) and (c)). The tension in the tube caused by the large inlet and outlet diameter and the residual stresses due to manufacture and packing resulted in a four-way buckling of the tube at the entrance and exit (section A – A). An S-shaped profile was present at the centre of the tube (section B – B) due to the narrowing of the tube at the buckled ends.

Although this particular solution gave good agreement with the experiments it was found that the L_0 = 67 mm tube also gave a similar collapse profile as to that in Figure 7.4 and this was not the case in the physical experiments. The collapse profile of such a tube in the experiments was flat with two small channels on either side (Figure 5.7(e) and (f)). This discrepancy could have been due to an inaccurate approximation of the tube material or by the coarser than desirable fluid mesh. Either way the numerical tube required some form of calibration in order to act in the same way as the physical tube.

7.2.3 Calibration Technique

The experimentally measured properties of the tube used in the linear elastic material model in LS-DYNA with the current fluid mesh resulted in a material with insufficient bending stiffness. This was apparent when comparing the computational results of the L_0 = 67 mm tube with those of the experiments. Without resorting to a more complex, and more costly, material model the bending stiffness was increased by increasing the thickness of the shells. The consequence of a larger thickness was an increased overall stiffness. This was resolved by reducing the Young's Modulus by the same proportion as the thickness had been increased. The thickness of the tube material was increased to 0.5 mm and the Young's Modulus was reduced accordingly (E = 0.91 MPa) so that the force/deflection characteristics remained the same as for the experimentally measured values. The density used was maintained at 920 kg/m^3 and the Poisson's ratio 0.49. These alterations were considered acceptable in the steady state but for unsteady models the density was also reduced in order to maintain the same speed of sound in the material and the same mass as for the experimentally measured properties (ρ_s = 644 kg/m^3).

Using these altered properties the collapse profile of the L_0 = 67 mm model resembled that of experiments (Figure 5.7(e) and (f)).

7.3 Steady Flow Models

The new approximation of the tube material was implemented in the numerical model. A comparison of the results from the steady state part of the experiment described in section 5.4 with the computational model was then made.

7.3.1 Model Properties

The altered material properties from section 7.2.3 were used ($\rho = 920$ kg/m^3, E = 0.91 MPa, $\nu = 0.49$, $w = 0.5$, $L = 65$ mm). An unstressed length of tube $L_0 = 67$ mm resulted by applying an initial axial stress of –0.0271 MPa to the 65 mm tube.

Limited computing resources and time constraints required that attention be focused on a small selection of numerical models for comparison with the experimental results. It was decided that three different $P_E - P_2$ values were to be used (10, 40 and 80 cmH_2O). Each of these models was to be subjected to a value of Q in the Poiseuille region (0.1 litres/min), the compliant region (0.5 litres/min) and also in the region of instability in the experiments (1 litres/min). The operating points of interest can be seen in Figure 5.11. It was also decided, because of CPU constraints, that the first order accurate donor cell advection algorithm with c = 10 m/s was used. The uncertainty relating to this combination of mesh and time-step determined in section 6 was significant and could possibly become larger due to the complexity of the collapsible-tube model and the interaction involved. However, as a first step towards a comparison with the collapsible tube experiments this error was considered small enough to yield results qualitatively similar to the experiments. Further refinement of the mesh resulted in unrealistic solution times as did increases in the fluid speed of sound so the current configuration was the most accurate attainable for realistic CPU cost.

The boundary conditions were applied at the inlet and external reservoir interfaces for pressures P_1 and P_E. The values applied were relative to P_2, which was set to zero, and taken directly from the experimental results. The flow rate was converted into an average velocity and applied as a flat profile at the inlet reservoir interface. This velocity was defined as a displacement in LS-DYNA and controlled by the gradient of its load curve.

7.3.2 Results

The comparison between LS-DYNA and experiment for flow rates of 0.5 litres/min are shown in Figure 7.6 and Figure 7.7 for $P_E - P_2$ values of 10 and 80 cmH_2O respectively.

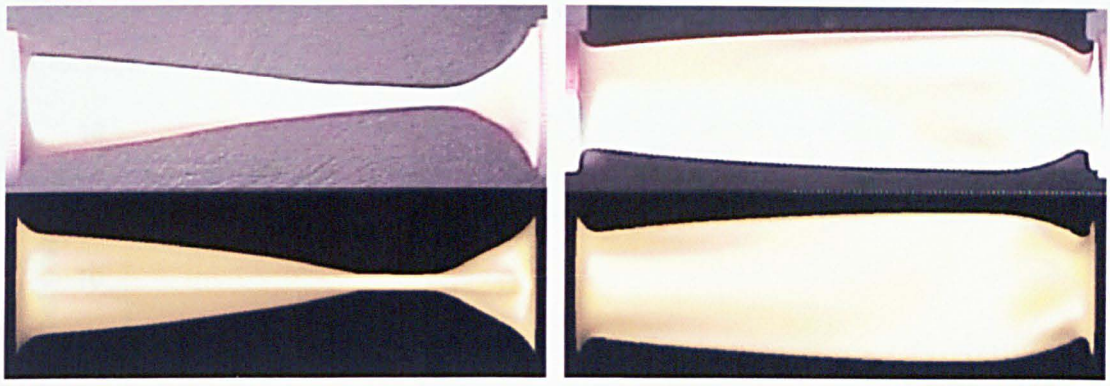

Figure 7.6. Side and top profiles of the experimental (top) and LS-DYNA (bottom) collapsible tubes subjected to a flow rate $Q = 0.5$ litres/min and $P_E - P_2 = 10$ cmH_2O

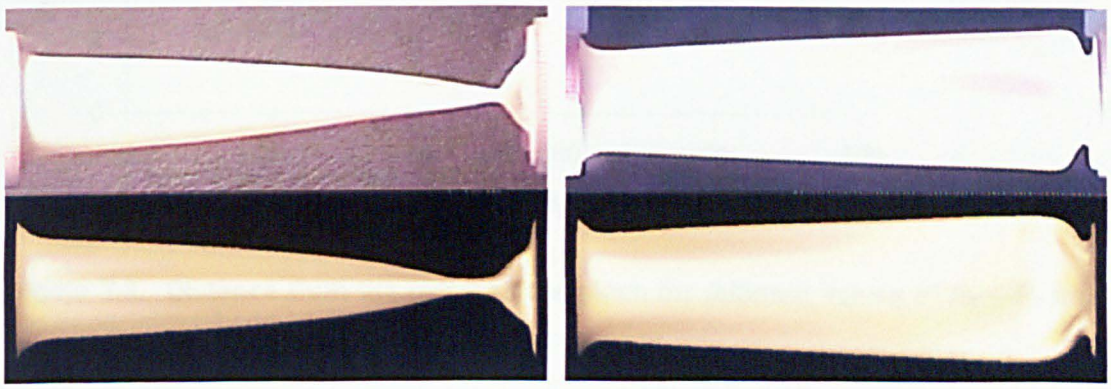

Figure 7.7. Side and top profiles of the experimental (top) and LS-DYNA (bottom) collapsible tubes subjected to a flow rate $Q = 0.5$ litres/min and $P_E - P_2 = 80$ cmH_2O

In both cases the LS-DYNA models show excellent similarity with the experiments for both inlet and outlet portions of the tube. The comparative shape and position of the pinch in the computer models were very similar to the shape and position from the corresponding experiment. In Figure 7.7 the contact with the rigid outlet face perpendicular to the flow is clearly visible in both experimental and computational results thus justifying its inclusion in the LS-DYNA model.

The only slight visible discrepancy in Figure 7.6 and Figure 7.7 is the fact that the pinch appears to cover a slightly greater length of the tube in the LS-DYNA results compared with the experiment. Also, for $P_E - P_2 = 80$ cmH_2O (Figure 7.7) small 'rigid' tunnels can be clearly seen angling in at approximately 48° to the tube axis in

the top view of the numerical results. This angle was approximately 60^{O} in the experimental results. This could have been a consequence of the use of a thicker material in the LS-DYNA model.

The position of the pinch in relation to the outlet was used as a tool for comparison. Figure 7.8 shows how the LS-DYNA and experimental models compared for $Q = 0.5$ litres/min.

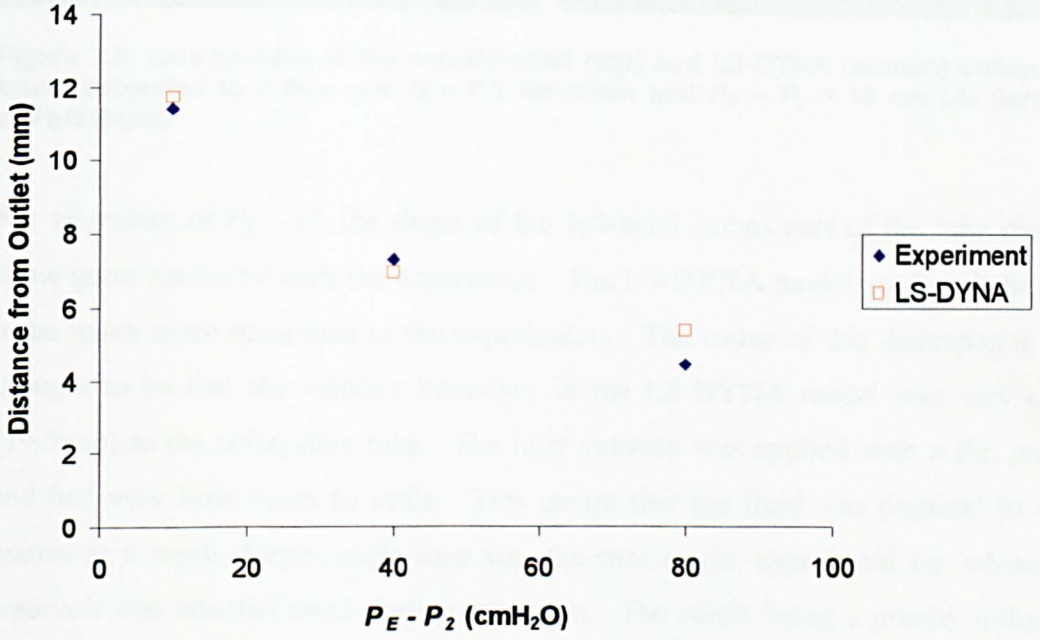

Figure 7.8. Distance from the outlet of the pinch for different values of $P_E - P_2$ from the experimental and LS-DYNA results.

The biggest difference was for $P_E - P_2 = 80$ cmH$_2$O which was 0.95mm (5.6% of the outlet tube outer diameter). The difference for the lower $P_E - P_2$ values was less than 0.35mm (<2% of the outlet tube outer diameter) in both cases. It is not surprising that the largest discrepancy was measured at the largest value of $P_E - P_2$ since the larger strains associated with larger transmural pressures would tend to magnify any flaws in the material properties and contact conditions used in the LS-DYNA model.

A similar set of data as to that in Figure 7.8 resulted for $Q = 0.1$ litres/min. However, there was a significant discrepancy in the upstream portion of the tube as shown in Figure 7.9.

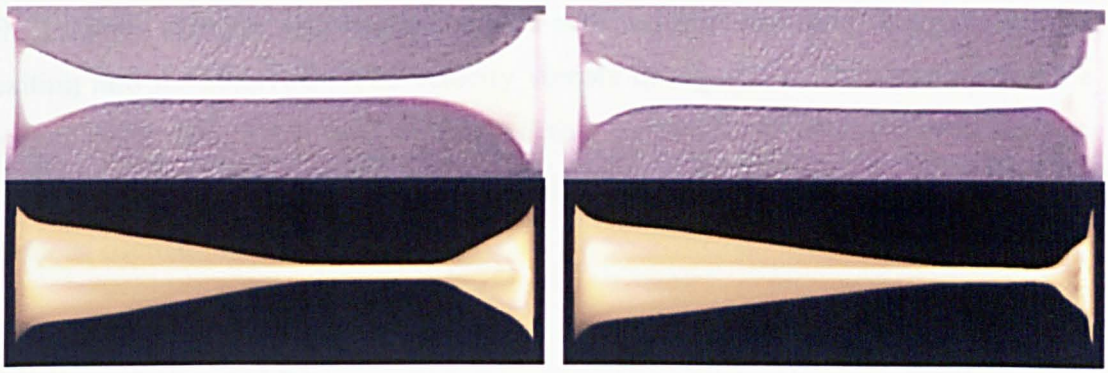

Figure 7.9. Side profiles of the experimental (top) and LS-DYNA (bottom) collapsible tubes subjected to a flow rate Q = 0.1 litres/min and $P_E - P_2$ = 10 cmH_2O (left), 80 cmH_2O (right)

For all values of $P_E - P_2$ the shape of the left-hand (inlet) part of the tube did not show good similarity with the experiment. The LS-DYNA model predicted the tube to be much more open than in the experiments. The cause of this discrepancy was thought to be that the velocity boundary in the LS-DYNA model was very close (19.5mm) to the collapsible tube. The inlet velocity was applied with a flat profile and had very little room to settle. This meant that the fluid was required to alter course at a much steeper angle than was the case in the experiment i.e. where the reservoir was situated much further upstream. The result being a greater influence on the tube shape in the LS-DYNA model.

7.3.2.1 Effect of a Longer Outlet Tube and Higher Fluid Speed of Sound

The effect of increasing the inlet and outlet lengths was assessed for the low flow models (Q = 0.1 litres/min) and also for the high flow rate models (1 litres/min) where the tube remained steady in the LS-DYNA model but was oscillatory in the experiments. Both inlet and outlet lengths were increased from 19.5mm to 37.5mm.

The results for the low flow (Q = 0.1 litres/min) were very similar to the run with the shorter inlet length. There was no significant difference in the tube profiles. It is thought that the inlet boundary was still too close to the tube to make a significant difference to the profile.

The analysis with $P_E - P_2$ = 10 cmH_2O and Q = 1 litres/min also exhibited a similar tube profile to that of the shorter inlet model. However, the fluid variables did exhibit significant differences, which could explain the failure of the model to predict flow-induced oscillations. Figure 7.10 shows the velocity vectors on the centre plane from a side view for both short and long outlet tubes. Figure 7.10(a) shows how the

fluid merely diverges and decelerates in a symmetric manner after the pinch before exiting into the reservoir. The velocity vectors in Figure 7.10(b) show that with a longer outlet length the fluid is allowed to separate from the upper wall and re-circulate, a phenomenon observed by Kounanis and Mathiolakis [18] before flow-induced oscillations began.

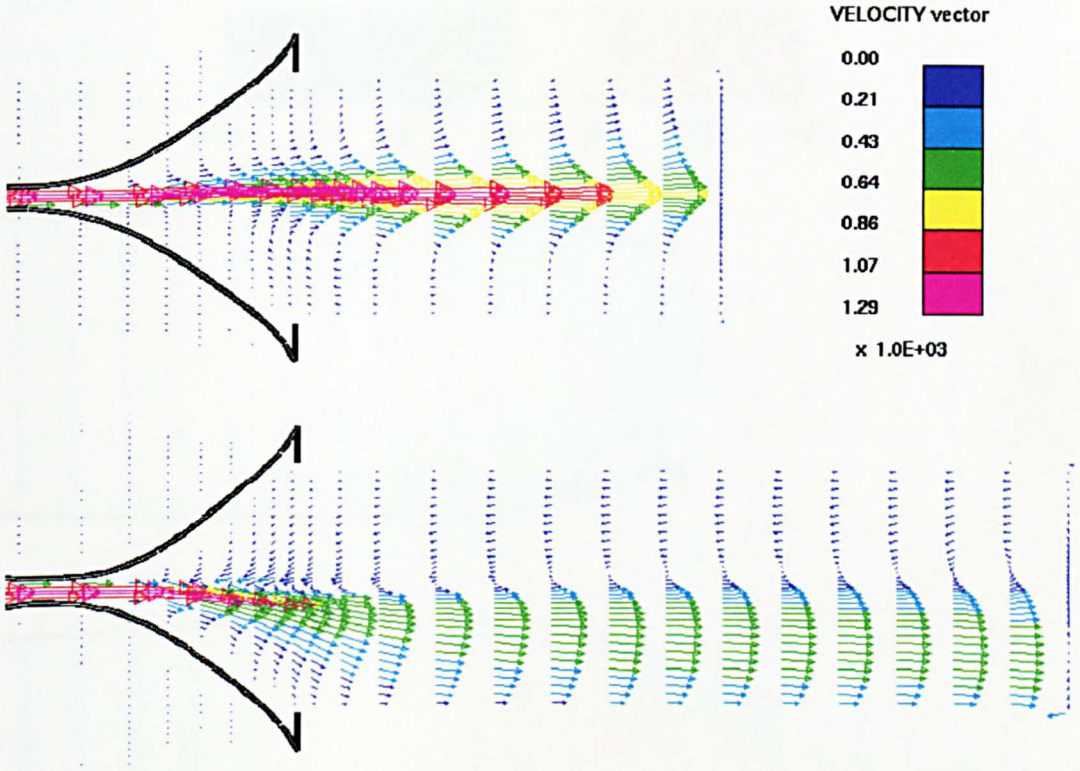

Figure 7.10 Side views of centre-plane velocity vectors (mm/s) for models of differing outlet lengths for $P_E - P_2 = 10$ cmH_2O and $Q = 1$ litres/min.

Yet another analysis was carried out which utilised a larger value of fluid speed of sound in order to ascertain to what degree this affected the solution of the full collapsible tube model. The results showed that for a flow rate of 0.5 litres/min and $P_E - P_2$ = 10 cmH_2O the maximum velocity at the pinch for the c = 10 m/s model was 1130 mm/s and for c = 30 m/s this value was 16% lower at 944 mm/s. The maximum principal stress in the tube was predicted to be 33% lower for c = 30 m/s and the minimum principal stress was 28% greater (negative value of 28% less magnitude). The error value predicted in section 6 was less than 5%. However, the larger error in the collapsible-tube model was thought to be caused by the interaction with the tube i.e. a small change in the fluid results causes a slightly different tube

profile which in turn affects the fluid. In other words the initially small error was magnified by the FSI in the system.

7.3.2.2 Fluid Velocity Profiles

The velocity profiles at the centre plane from the top view are shown in Figure 7.11 for the three values of Q with $P_E - P_2 = 10\text{cmH}_2\text{O}$.

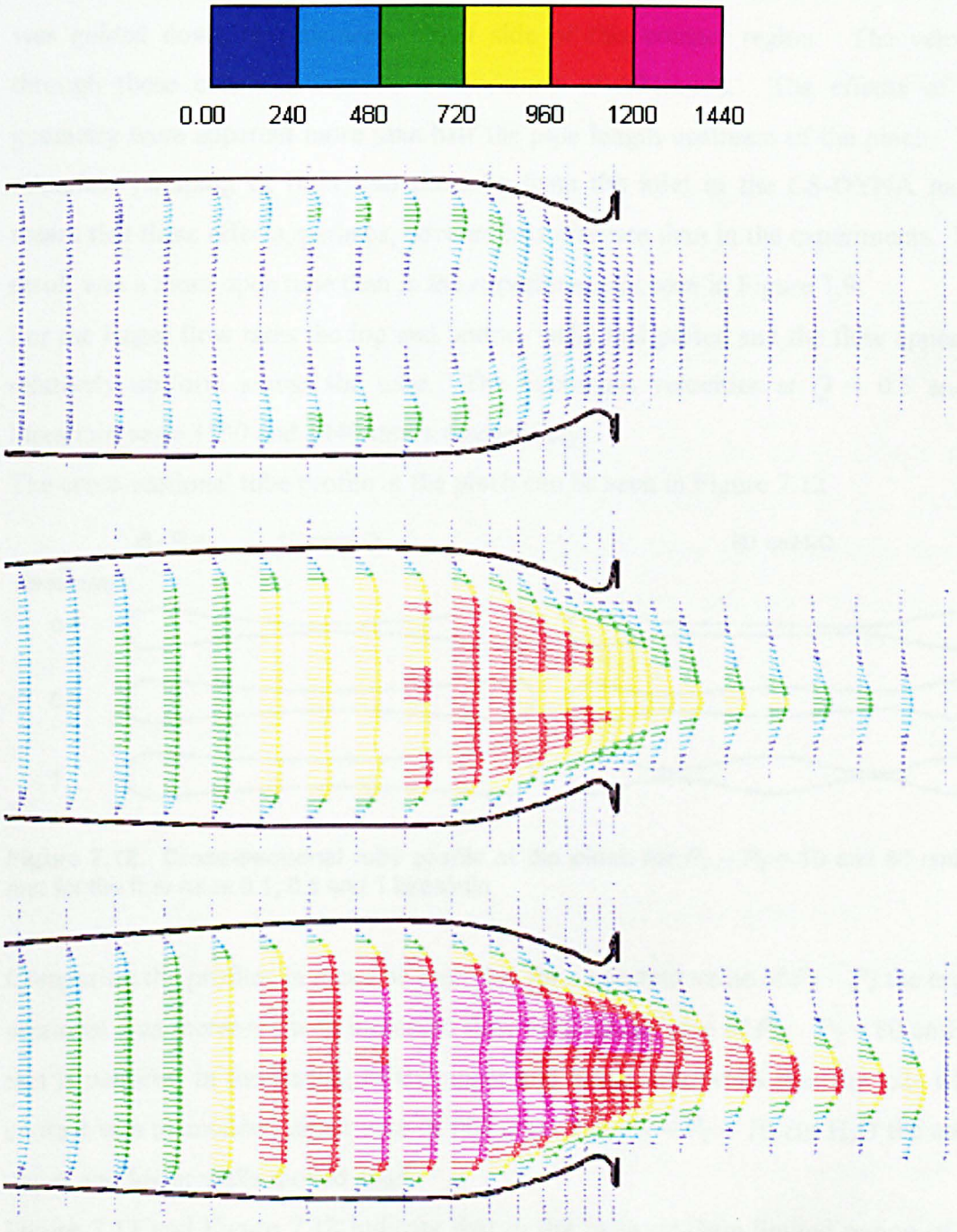

Figure 7.11. Top view of the centre plane velocity vectors (mm/s) at the tube pinch in mm/s for $P_E - P_2$ =10 cmH$_2$O and Q = 0.1 (top), 0.5 (middle) and 1 (bottom) litres/min

The quantitative accuracy of these velocity values was subject to uncertainty due to the current model configuration as well as the inability to compare with the experiments. Such a detailed description of the internal fluid flow would be difficult to retrieve from experiments.

By comparing the velocity vectors of Figure 7.11 together it can be seen that for the lowest flow rate (Q = 0.1 litres/min) there was tube contact at the neck and the flow was guided down two channels either side of this contact region. The velocity through these channels reached a maximum of 691mm/s. The effects of the geometry were apparent more than half the pipe length upstream of the pinch. The relentless pumping of fluid into the tube from the inlet in the LS-DYNA model meant that these effects, perhaps, covered less distance than in the experiments. The result was a more open tube than in the experiments as seen in Figure 7.9.

For the larger flow rates the top and bottom walls had parted and the flow appeared relatively uniform across the tube. The maximum velocities at Q = 0.5 and 1 litres/min were 1130 and 1440 mm/s respectively.

The cross-sectional tube profile at the pinch can be seen in Figure 7.12

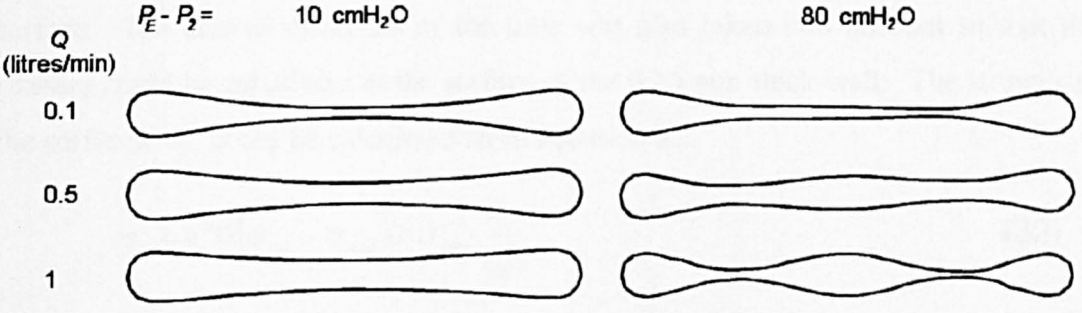

Figure 7.12. Cross-sectional tube profile at the pinch for $P_E - P_2$ = 10 and 80 cmH$_2$O and for the flow rates 0.1, 0.5 and 1 litres/min

Comparing the profiles in it can be seen that for a constant value of $P_E - P_2$ the cross-sectional area increased with increased flow rate. In the case of $P_E - P_2$ = 80 cmH$_2$O this is manifest in the parting of the upper and lower tube walls near the axis while contact was maintained either side of this area. For $P_E - P_2$ = 10 cm H$_2$O the entire upper and lower walls moved apart.

Figure 7.11 and Figure 7.12 indicate that in the pressure-drop-limited region of the characteristic curve the maximum local velocity at the pinch got larger along with an increase in cross-sectional area.

7.3.2.3 Stresses in the Tube Walls

The tube wall stresses calculated by the LS-DYNA model were different from those of the experimental tube owing to the altered properties. However, these stresses remained proportional to those of the experiment as the force-deflection characteristics were maintained in the linear elastic LS-DYNA material.

The actual mid-plane stress, σ_m, could be calculated from equation 31.

$$\sigma_m = \sigma_{mid} \times \frac{E_e}{E_D} \tag{31}$$

where σ_{mid} = mid-plane stress from LS-DYNA, E_e = experimentally determined value of Young's modulus and E_D = Young's modulus used in LS-DYNA model. Therefore the stress results from LS-DYNA required multiplication by a factor of 1.429 to gain stress results that could be compared to the stresses in the real tube (see section 7.2.3).

The retrieval of the stresses at top and bottom surfaces was achieved by extrapolation of the reported stresses at the top and bottom integration points to the physical surface. The altered thickness of the tube was also taken into account so that the stresses could be calculated at the surface of the 0.35 mm thick wall. The stresses at the surfaces, σ_s, could be calculated from equation 32.

$$\sigma_s = 1.73\left(\sigma_{top} - \sigma_{mid}\right) + \sigma_{mid}\frac{E_e}{E_D} \tag{32}$$

where σ_{top} = stress at top or bottom integration point in LS-DYNA, and the multiplier 1.73 is a value given in the OASys LS-DYNA users guide [69].

The good agreement between experiment and LS-DYNA for the shape of the tube instilled enough confidence in the code for the strains, hence the stresses, in the tube model to be qualitatively believable. Figure 7.13 and Figure 7.14 show the maximum and minimum principal stresses for the top integration point, middle plane and bottom integration point of the tube shells in the fully collapsed position near the outlet for $P_E - P_2 = 10$ cmH_2O and $Q = 0.5$ litres/min. Similar plots for $P_E - P_2 = 80$ cmH_2O can be seen in Figure 7.15 and Figure 7.16.

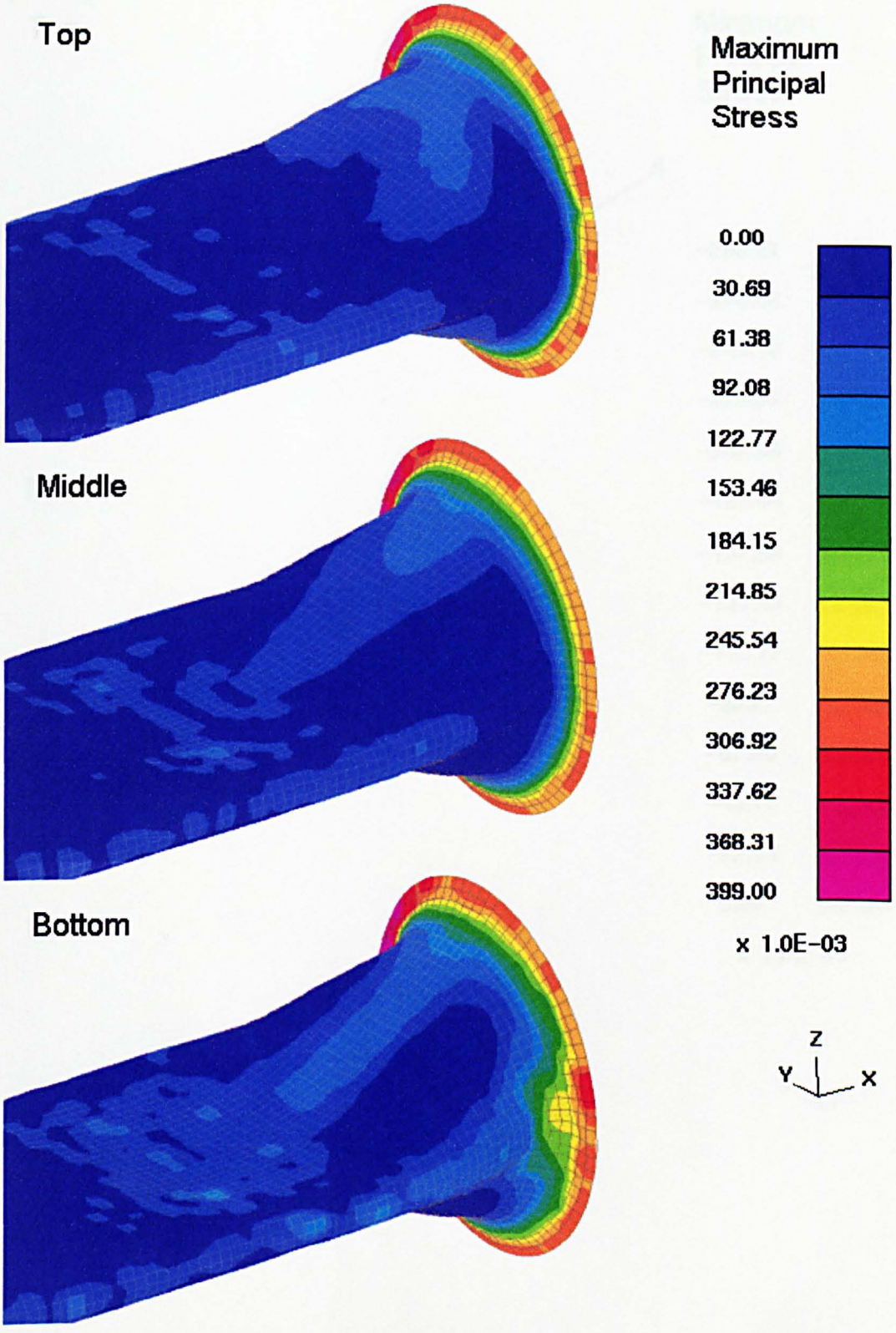

Figure 7.13. Maximum principal stress for the top, middle and bottom integration points of the collapsible tube at the outlet subjected to $Q = 0.5$ litres/min and $P_E - P_2 = 10$ cmH_2O. For stresses comparable to the experimental tube these stress values must be used with equations 31 and 32.

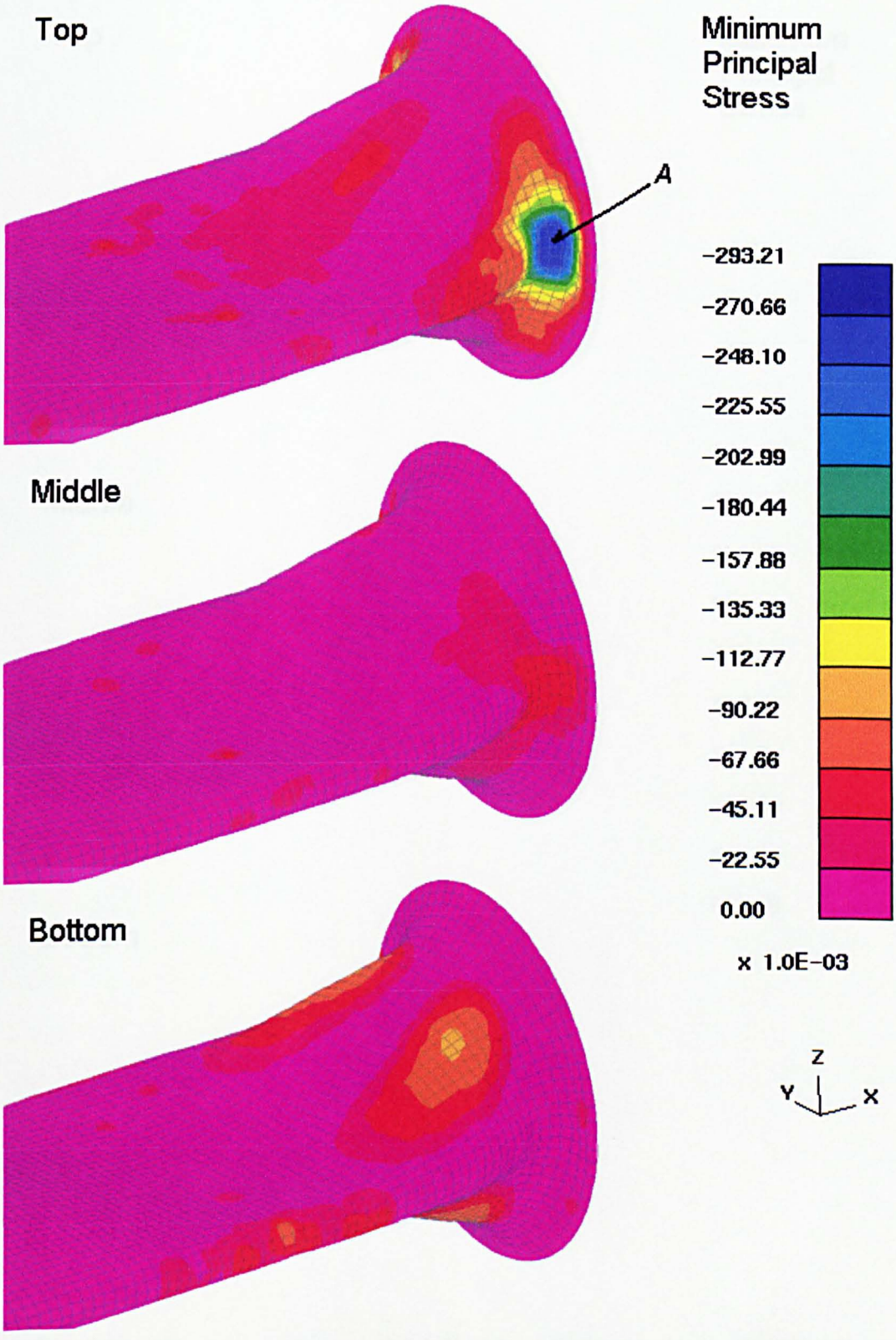

Figure 7.14. Minimum principal stress for the top, middle and bottom integration points of the collapsible tube at the outlet subjected to $Q = 0.5$ litres/min and $P_E - P_2 = 10$ cmH_2O. For stresses comparable to the experimental tube these stress values must be used with equations 31 and 32.

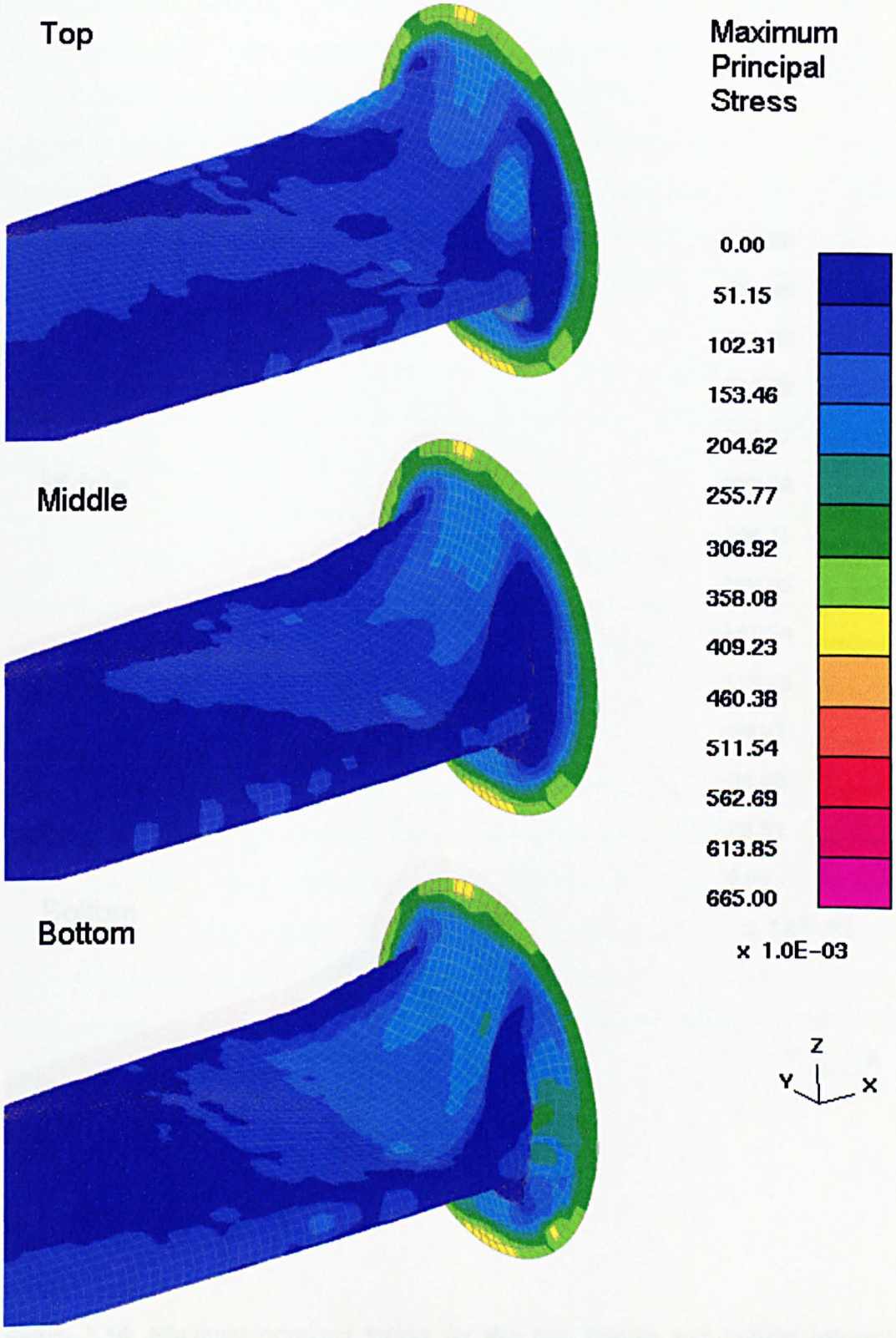

Figure 7.15. Maximum principal stress for the top, middle and bottom integration points of the collapsible tube at the outlet subjected to Q = 0.5 litres/min and $P_E - P_2$ = 80 cmH_2O. For stresses comparable to the experimental tube these stress values must be used with equations 31 and 32.

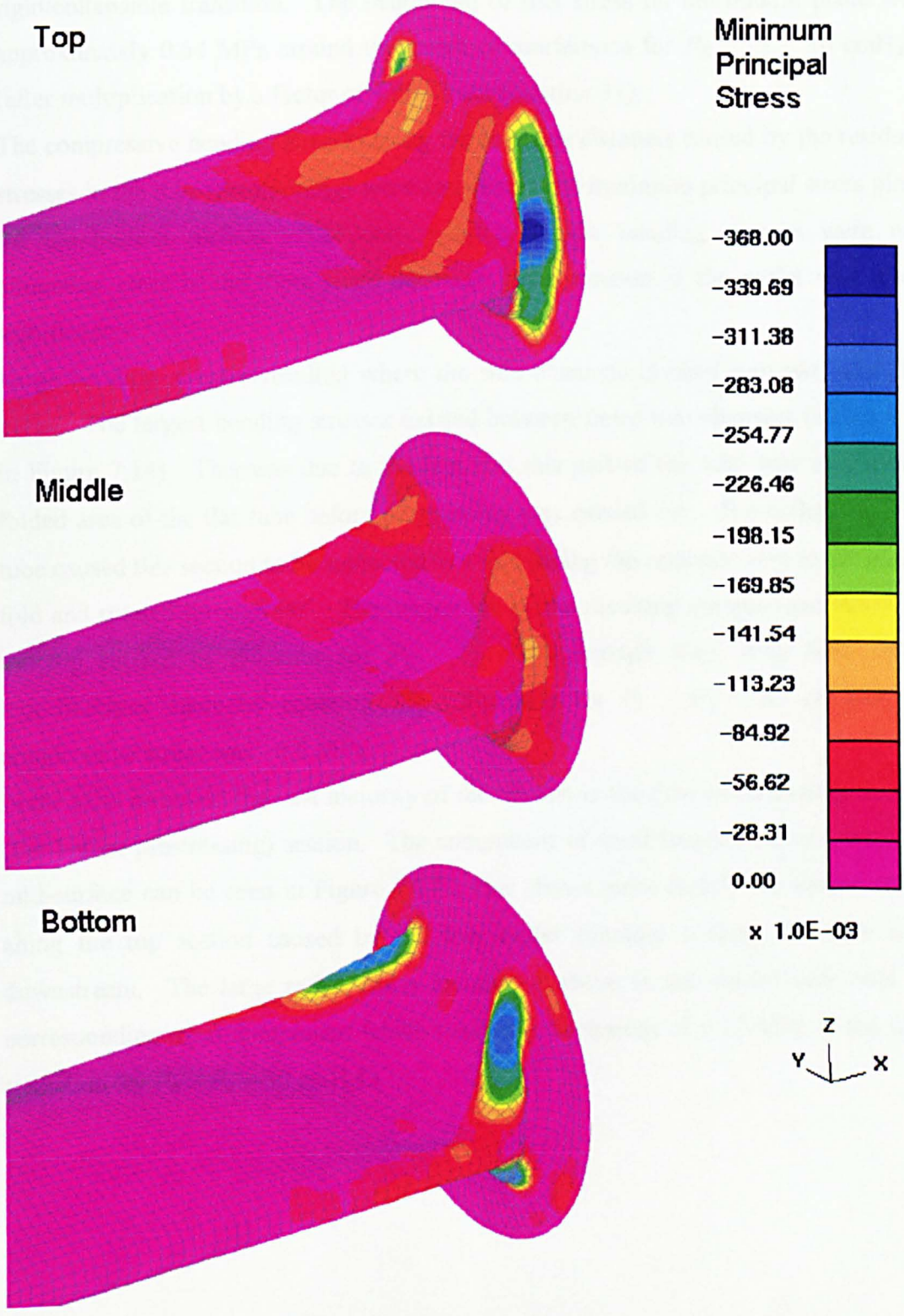

Figure 7.16. Minimum principal stress for the top, middle and bottom integration points of the collapsible tube at the outlet subjected to $Q = 0.5$ litres/min and $P_E - P_2 = 80$ cmH_2O. For stresses comparable to the experimental tube these stress values must be used with equations 31 and 32.

Owing to the large difference in the unstressed tube diameter and the diameter of the rigid inlet and outlet sections there existed a large radial stress in the proximity of the

rigid/collapsible transition. The magnitude of this stress on the middle plane was approximately 0.54 MPa around the entire circumference for $P_E - P_2 = 10$ cmH_2O (after multiplication by a factor of 1.429 from equation 31).

The compressive bending stresses along the two side channels caused by the residual stresses in the tube (prestressing) were apparent in the minimum principal stress plots for the bottom surface. The corresponding tensile bending stresses were not altogether clear in the plots since the large radial tension at the outlet was more significant.

Large bending stresses resulted where the side channels divided into two near the outlet. The largest bending stresses existed between these two channels (element A in Figure 7.14). This was due to the fact that this part of the tube was an initially folded area of the flat tube before prestressing was carried out. The collapse of the tube caused this section to be subjected to a fold facing the opposite way to the initial fold and rotated through 90°. The magnitude of the resulting compressive stress on the top surface of the tube for $P_E - P_2 = 10$ cmH_2O was –0.48 MPa (after modifications made by equation 32). Similarly for $P_E - P_2 = 80$ cmH_2O the compressive stress was –0.6 MPa.

In the axial direction the vast majority of the tension in the tube existed along the top (flat before prestressing) section. The component of local longitudinal stress at the mid-surface can be seen in Figure 7.17. This shows more clearly the tensile stress along the top section caused by the low outlet pressure sucking the tube wall downstream. The large radial stress mentioned above is not shown here only its corresponding axial component which reaches a maximum of 0.27 MPa at the tube transition for $P_E - P_2 = 80$ cmH_2O.

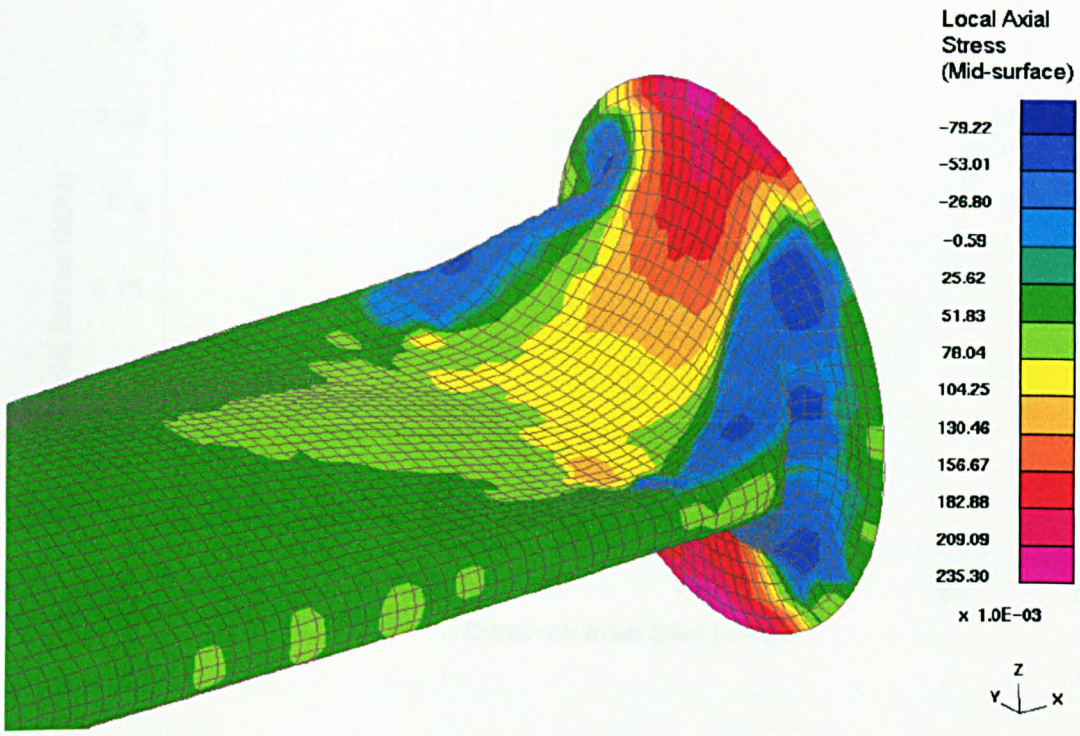

Figure 7.17. Local axial stress at the outlet end of the collapsible tube for Q = 0.5 litres/min and $P_E - P_2$ = 80 cmH_2O. For stresses comparable to the experimental tube multiply by 1.429

Nearly all the longitudinal tensile stress is placed along this top centre section near the outlet while the side channels at the outlet remain relatively unstressed in this direction. Figure 7.18 shows the longitudinal stress along the top centre line of the tube.

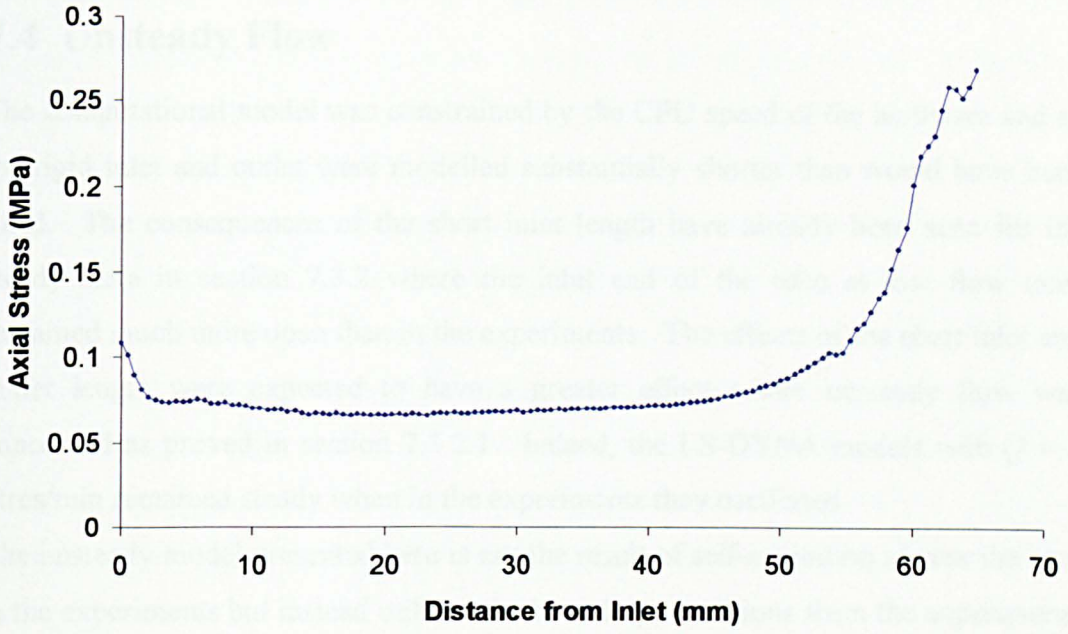

Figure 7.18. Longitudinal stress along the top centre-line measured at the mid-surface for $P_E - P_2 = 80$ cmH_2O and $Q = 0.5$ litres/min

It can be seen in Figure 7.18 that the longitudinal tension in the tube at the inlet is only 40% of the outlet value. After the initial large stress caused by the radial stretching at the inlet the tension then fell steeply to a value that remained fairly constant until near the pinch. After the pinch the tension then rose rapidly towards the outlet. Pedley [16] suggested that the tension in the tube wall needed to decrease with distance downstream in order to remain in equilibrium. However, for the range of results presented here any slack in the tube walls was taken up by the ability of the pinch to continue to stretch downstream thus extending the tube wall and maintaining the tension.

7.4 Unsteady Flow

The computational model was constrained by the CPU speed of the hardware and so the rigid inlet and outlet were modelled substantially shorter than would have been liked. The consequences of the short inlet length have already been seen for the steady state in section 7.3.2 where the inlet end of the tube at low flow rates remained much more open than in the experiments. The effects of the short inlet and outlet length were expected to have a greater effect where unsteady flow was concerned as proved in section 7.3.2.1. Indeed, the LS-DYNA models with Q = 1 litres/min remained steady when in the experiments they oscillated.

The unsteady model presented here is not the result of self-excitation as was the case in the experiments but instead utilised the boundary conditions from the experiments in an effort to force the oscillations. The results of such an analysis allow the behaviour of the stresses within the tube walls to be analysed over a complete cycle of an oscillation. It must be remembered that a solution to the puzzle of why oscillations occur was not the aim of this project but instead the construction of a computational model with a wide range of physiological uses was sought. The forced unsteady model has direct relevance to the original impetus for this project, which was the analysis of pulsatile flow through heart valves.

The unsteady flow model presented here is by no means the finished article. This analysis represents a first step towards the validation of unsteady models of this type in LS-DYNA. The edited LS-DYNA input file used in this analysis is given in appendix F.

7.4.1 Model Properties

The unsteady model utilised a structural density that resulted in the same mass and speed of sound as that of the experimentally measured values. This was achieved by reducing the density by the same proportion as the tube thickness had been increased and the Young's modulus had been reduced.

The fluid speed of sound was increased from the value used in the steady-state models in order to make it less compressible and have less of an effect on the pressure transients.

The material properties of the second model were for the pipe: ρ_s = 644 kg/m^3, E = 0.91 MPa, ν = 0.49, w = 0.5, L = 65mm. The fluid had properties ρ_f = 998 kg/m^3,

μ = 0.001 Pa s, c = 40 m/s. The pressure cut-off was set at –10 MPa. A 67 mm unstressed length of tube was modelled by applying an initial axial stress of –0.0271 MPa to the 65 mm tube.

The pressure signals resulting from the oscillations at 1 litres/min for a mean $P_E - P_2$ of 10 cmH_2O were recorded from the experiment (Figure 5.12) and used as boundary conditions in the LS-DYNA model. A simplified waveform was used for the P_1 and P_E values in the LS-DYNA model to represent the pressure differences $P_1 - P_2$ and $P_E - P_2$, which were assumed equal since this was approximately the case in the experiments. The value P_2 was set to zero in the LS-DYNA model. The waveform is shown in Figure 7.19. The flow was assumed constant at 1litre/min at the inlet, and was applied as a flat velocity profile of magnitude 125.6 mm/s.

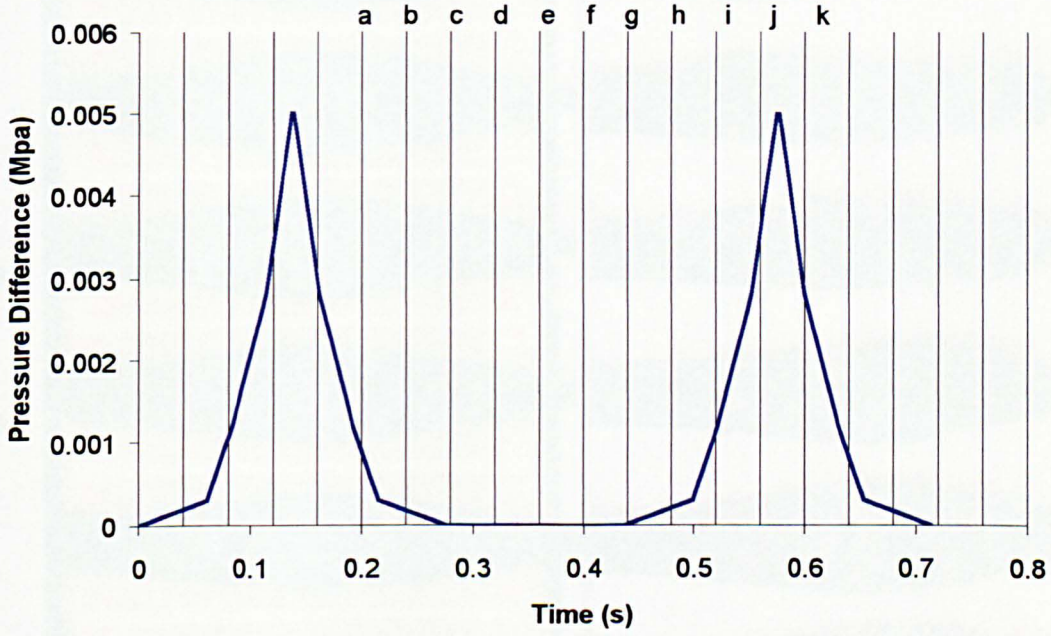

Figure 7.19. Unsteady boundary conditions used in the LS-DYNA model at P_E and P_1. Vertical lines represent the output plot times from the LS-DYNA results and correspond with the frames in Figure 7.20

7.4.2 Results

The LS-DYNA model was terminated after 6.509 seconds of model time that took 262 CPU hours (11 days) to solve. The side profile results are best viewed as an animation, the frames of which are shown in Figure 7.20 for one complete cycle and compared with the results from the experiments.

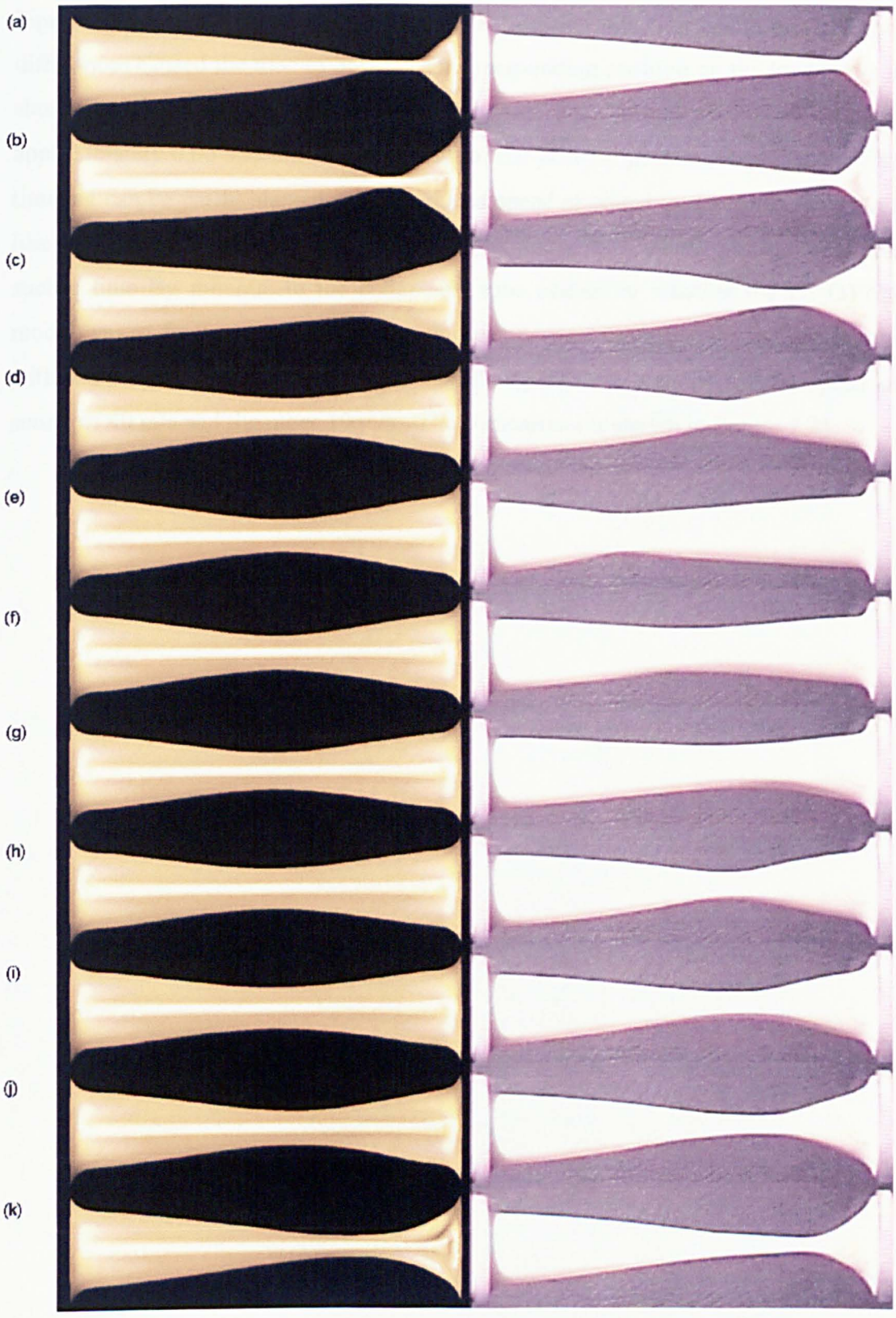

Figure 7.20. Transient response of the collapsible tube at a flow rate of 1 litres/min for $P_E - P_2 = 10cmH_2O$ for the LS-DYNA (left) and experimental (right) models. Frames separated by 0.04 seconds and correspond to Figure 7.19

Figure 7.20 (a) shows the tube profile just before the reduction in the two pressure differences caused the tube to open. The corresponding position on the load curve is shown in Figure 7.19. It can be seen that this heavily collapsed profile occurs approximately 0.06 seconds after the peak of the positive pressure load curve. This time lag can be partly blamed on the reduced speed of sound in the fluid. Without a like-for-like comparison with experiments it cannot be determined whether there was such a time lag inherent in the collapsible tube system or whether the LS-DYNA model was at fault. Instead a comparison was drawn between two LS-DYNA runs with the only difference between the two being that one utilised a fluid speed of sound of 40 m/s and the other 10 m/s. The comparison is shown in Figure 7.21.

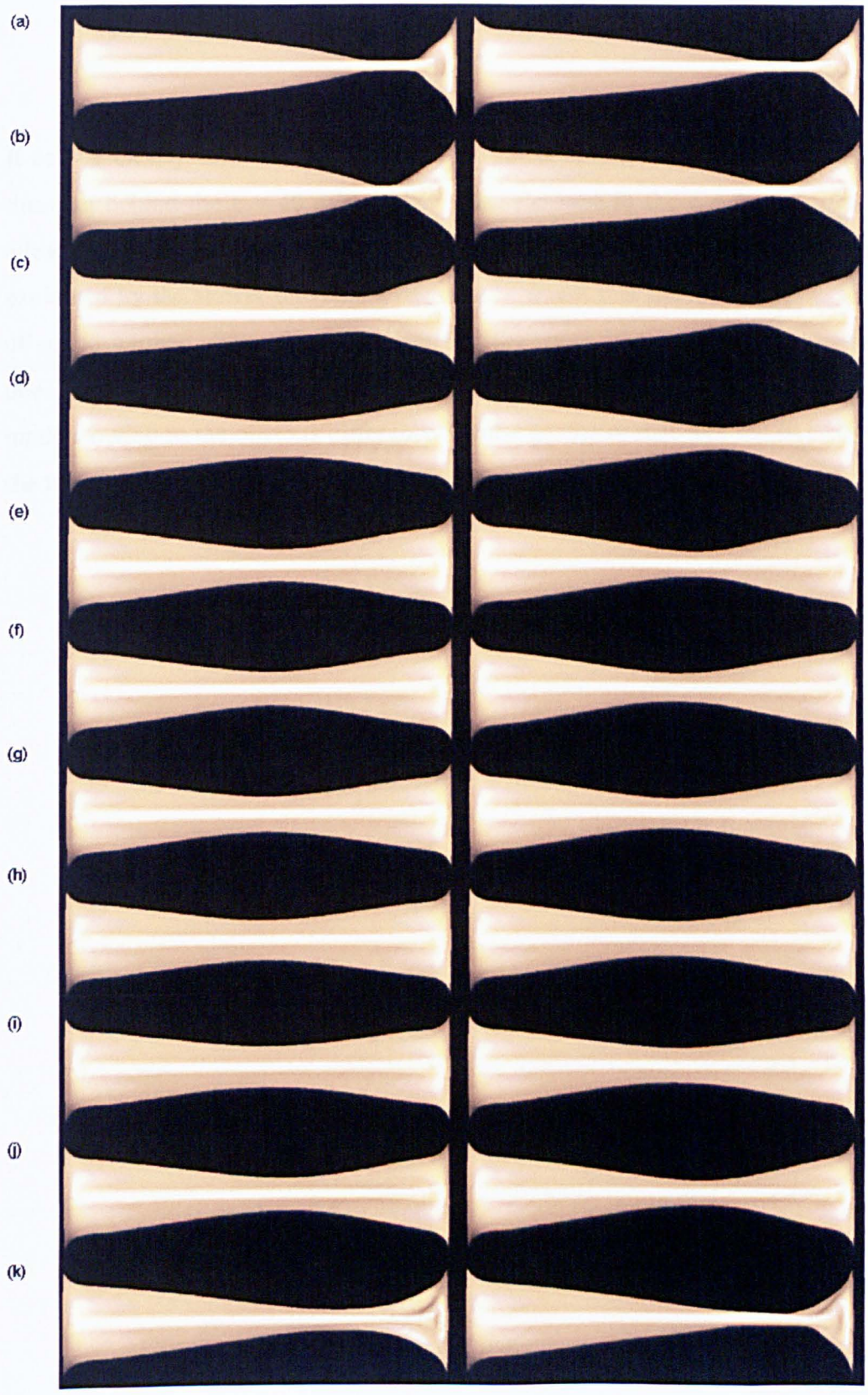

Figure 7.21 Comparison between similar forced oscillatory models with c = 40 m/s (left) and c =10 m/s (right)

It can be clearly seen that by frame (c) the lower speed of sound model exhibits a time lag behind the c = 40 m/s model. Also the tube in the c = 10 m/s run is not allowed to open up as much before once again collapsing. This can be simply explained by the slower movement of pressure waves that the reduction in the speed of sound implies. Therefore it is clear that the value of c in the oscillatory models does have a significant effect on the solution. More so than in the steady state models owing to the obvious difference in tube geometry that was observed between the two unsteady models.

8 Discussion

Analytical modelling of complex three-dimensional deformable structures interacting with fluids is, in the main, not viable. Experimental analysis continues to provide the only viable method for the retrieval of data from these systems. This research aimed to assess the validity and viability of the computational modelling of these FSI systems using an explicit finite element code: specifically the suitability of this method of analysis for highly deformable physiological components such as heart valves interacting with a fluid. However, the collapsible-tube experiment was chosen as a tool for comparison as it represents a complex dynamic FSI system but which utilises a relatively simple geometry and homogenous material. The experiments performed were dependent on the elastic properties of the structure as well as the viscous nature of the fluid and therefore provided for an excellent example of fluid-structure interaction, particularly when the system became unsteady. From a computational viewpoint the collapsible-tube profile could not be accurately modelled if the viscous fluid were not included since it was the flowing fluid that caused the collapse to occur at the downstream end which in turn affected the fluid flow and so on.

The fluid was computationally modelled using a spatially fixed Eulerian mesh. Lagrangian, Eulerian and ALE formulations have all been used to computationally model fluids but only the Eulerian and ALE formulations can be effectively used when the fluid is required to flow any significant distance. A Lagrangian mesh would simply deform with the shear and vorticity inherent in most fluids and would very rapidly become useless for any analytical purpose. The Eulerian mesh was used as the fluid-structure coupling involved a Lagrangian structure that moved through the Eulerian mesh. This immersed boundary method of fluid-structure interaction was observed to not be without its problems but was necessary when considering the large deformation of the tube as it collapsed; a detail that rendered the ALE moving-wall type of FSI undesirable due to the distortion of the elements. A problem that was identified with the Lagrangian-in-Eulerian FSI method was that when the structural mesh was too coarse the fluid escaped through it. Also, the method of coupling required that the fluid elements that contained the structural nodes were constrained to move with them during the Lagrangian time-step. Therefore, the no-

slip condition acted at all the nodes of these fluid elements. If the fluid elements were large the nodes at which the no-slip condition acted could have been a significant distance from the structure itself. It is this no-slip condition that also caused the automatic activation of contact between the top and bottom tube walls when within the Eulerian mesh. This feature of the FSI method did not cause a major problem in this case, however it did mean that the fluid elements were required to be very small where tube self-contact was expected to take place. If this were not the case then effective contact would occur when the tube walls were still a significant distance apart and fluid flow in this region would cease resulting in non-physical results.

The mesh independence checks of section 6.1 determined that the mesh resolution required for accurate modelling of the viscous properties of water was too fine for feasible solution times even with an artificially increased time-step size. The uncertainty of the solution for a mesh with elements of edge length 0.5 mm was 31.8% when analysing a numerical fluid with the properties of water. However, mesh independence was achieved to a satisfactory level when utilising a fluid of viscosity two orders of magnitude greater than that of water. This successful convergence has little use for comparison with the collapsible tube experiments but it does prove that fluids with realistic properties can achieve mesh independence with the current configuration of computer hardware. This is a problem faced by all CFD codes in that the lower the fluid viscosity the finer the mesh needs to be in order to accurately calculate the velocity profile. With a relatively high viscosity a coarser mesh resolution became acceptable. It was observed that, for the current configuration of computer hardware, mesh independence was not achieved to a satisfactory level for a good quantitative comparison with the current experiments. This was not only a result of an exponentially increased number of elements for every refinement of the mesh but also a function of the smaller time-step associated with smaller elements.

Although it is implicit codes (ADINA and FIDAP) that appear to be leading the way in numerical modelling of FSI it is the explicit method that offers the resolution in the time domain to enable contact, material non-linearity and the modelling of rapid events and large displacements. Such attributes are vital for the accurate analysis of heart valves and the like. The explicit technique is conditionally stable and has a relatively small time-step compared to the implicit technique. This means that an

explicit analysis requires more solution cycles through the model than an implicit technique before the termination time is reached. However, the implicit technique suffers from the need to solve large global matrices rendering each time-step much more computationally expensive than the relatively simple explicit time-step. The major stumbling block regarding the use of the explicit technique for the analysis of these FSI systems is the resolution of the finite element model needed and the consequent solution time. All this adds up to a much greater CPU time for a solution. It was therefore necessary to raise the time-step of the analysis. The speed of sound in the rubber tube was naturally so low that the water could be considered incompressible. In other words any fluctuation in fluid pressure would readily be smoothed by the compliance of the tube wall and not in the compression of the fluid. However, the condition of incompressibility could not be modelled in the Eulerian formulation of LS-DYNA 950d and the use of the real speed of sound resulted in an unacceptably small time-step. The time-step was artificially increased by reducing the speed of sound of the fluid as explained in section 4.1.3.

The speed of sound convergence study in section 6.2 utilised a small, fluid-only test model that achieved convergence to an acceptable level (0.7%) at c = 30 m/s and an arguably acceptable convergence (5%) was achieved at c = 10 m/s. In the steady state models, the speed of sound in the fluid was reduced to 10 m/s and the effect of this reduction of c in the full collapsible-tube model was quantified by running another model with c = 30 m/s. The difference between the two sets of results ranged from a 16% error in the prediction of the fluid velocity at the pinch to 33% error for the maximum principal stress in the tube walls. Comparing these values to the error determined by the small test model it can be seen that the error has been magnified by the FSI in the system i.e. a small change in the fluid results caused a slightly different tube profile which in turn affected the fluid. This magnification of error in the FSI system is not surprising but is significant. This proves that the error tolerance in interacting systems such as these must be smaller than if a fluid-only or structure-only analysis were being run. Unfortunately this statement cannot be accurately quantified here due to the level of uncertainty within the current model.

For the purposes of this research the current uncertainties relating to the numerical modelling of water were tolerated, the alternative was to seek mesh independence and tolerate CPU times of several months (see Figure 6.6). Although the uncertainty

appeared large when striving for quantitatively accurate results it was not so large that good qualitative comparison with experiments could not be achieved.

A linear elastic material model represented the Latex tube structure in the full collapsible-tube model. The density, geometrical dimensions and stress-strain characteristics of the Latex rubber Penrose tube were experimentally determined. When these properties were used in the computer model an insufficient bending stiffness was apparent since the collapsed tube exhibited ridges on both top and bottom surfaces. This collapse profile was observed in the experiments when a higher tension existed in the tube walls (see Figure 5.7 (b) and (c)). However, this was not the correct profile for the configuration of the tube being modelled. In order to alleviate this problem the linear elastic material was calibrated by using an increased tube-wall thickness to increase the bending stiffness. The Young's modulus of the material was reduced by the same proportion so that the force-deflection characteristics of the tube remained the same, the density was also increased accordingly so that the mass of material and the speed of sound in the material remained the same.

How, then, was such good geometrical correlation achieved when such a large degree of uncertainty existed in the discretization of the fluid and the material properties of the tube had been altered? The answer to this question may lie in the significance of the fluid viscosity and shear stresses in the physical problem. Fluid shear is vital in order to achieve a qualitatively accurate solution since it is the fluid shear that causes the collapse of the tube at the outset. The error associated with a coarse fluid mesh tended to magnify the viscosity so that a new 'effective' viscosity was utilised by the computer model (see Figure 6.2). In the collapsible-tube model this increased viscosity was effectively balanced by the increase in thickness of the collapsible tube material, which is how good geometrical agreement existed. The position of the pinch at the downstream end differed by less than 5.6% of the outlet tube outer diameter in the worst case.

A discrepancy was observed in the collapsible-tube model at low flow rates where the collapsed section of the tube was observed to extend upstream in the experiments. The LS-DYNA model predicted a much more open tube than those observed in the experiments. This was caused by a combination of two reasons. Firstly the discrepancy may have been contributed to by the altered material properties. Secondly, the close proximity of the inlet velocity boundary acted as a

flow pump. This meant that fluid was relentlessly introduced into the main flow domain at a constant velocity only 19.5mm from the tube inlet. This condition was not alleviated when the inlet length was increased to 37.5 mm therefore this second possibility has not been proved.

The comparison of the computer model with experiments for the tube geometry marked the extent of the qualitative validation due to the known errors inherent in the current computational model. The reason it was only the geometry that was compared was due to the difficulty of accurately retrieving stresses and strains from the walls of the tube and the difficulties associated with the visualisation of the internal fluid flow. It is these very difficulties associated with experiments of this nature that renders computational modelling a necessity for any future improvement in the understanding of such systems. The ability to view detailed stress results in the tube walls and the response of the fluid flowing internally was a major achievement and is an excellent example of the integrated use of experiments and computational analysis to gain an understanding of a multi-physics problem. It also represents a major advantage over experimental studies. Of course, the coarser than desirable fluid mesh coupled with a low fluid speed of sound meant that the quantitative stress and velocity results must be treated with caution. This point was proved, as mentioned previously, when two similar models utilising different fluid speed of sound values (c = 10 m/s and 30 m/s) produced a discrepancy of 33% for the calculated maximum principal stress.

Boundary conditions that resulted in self-excitation of the tube in the experiment remained steady in the LS-DYNA model. This was due to the short outlet length. When a longer outlet length was used a different velocity profile resulted which included flow separation and recirculation but not oscillations. It has been shown that LS-DYNA can model flow-induced vortex shedding from the flow over a cylinder analysis. Therefore, self-excitation of the collapsible tube should also be possible. With increases in CPU speed it will be possible to refine the fluid mesh and incorporate a longer outlet length so that this theory can be proved.

Since self-excitation of the tube was not achieved with this particular computational model the measured results from the unsteady experiments were used as the boundary conditions in an LS-DYNA analysis. The resulting oscillatory profiles were compared to the self-excited oscillations observed in the experiment. In the experiments the pinch completely traversed the entire tube and returned to the outlet

end as the tube collapsed. In the LS-DYNA model the movement of the pinch was halted only halfway up the tube. This inaccuracy was caused by the close proximity of the upstream velocity boundary, the relentless pumping of fluid into the tube acted to stop the movement of the pinch travelling upstream as was seen in the experimental results in Figure 7.20 (c) to (e). Here the pinch remained at the centre of the tube in the LS-DYNA model but continued travelling to a point near the inlet in the experimental results. The effect of the lowered fluid sonic velocity, 40 m/s instead of 1483 m/s, was also a contributing factor in the model's inaccuracies as it introduced a time lag. Unfortunately this lag could not be accurately measured, as it was unclear whether the pictures being compared were in phase with one another. In the experiment no effort was made to record the pictures in phase with the recorded pressure signals. Kounanis and Mathioulakis [18] used a trigger pulse that was sent to their video camera at the instant pressure measurements were initiated. The output of which (one picture and its time code) were digitised. Thus, knowing the time code of the particular picture that the pressure measurements started, all pictures recorded later were in phase with the pressure signals. Such a procedure must be followed if a good comparison is to be drawn between experiments and the LS-DYNA model in the future. The time lag was visualised however when the same LS-DYNA model was run with c =10 m/s (compared with 40 m/s) enabling a like-for-like comparison. The faster speed of sound model produced a much quicker opening of the tube and also a larger magnitude of opening. Obviously, the reasons behind this were that the pressure signals from the fluid boundaries travelled more quickly in the higher speed of sound model.

The comparison between LS-DYNA and the unsteady experiment (Figure 7.20) was made due to consideration of the original impetus for this research, which was the modelling of heart valves. Like the modelling of the collapsible tube the FSI modelling of a heart valve requires that it be separated from its immediate surroundings and be subjected to certain boundary conditions that mimic the pulsatile blood flow. These boundary conditions being determined via an in-vitro experiment or intrusively in-vivo. The cause of the pressure fluctuations could be the heart valve itself or some other occurrence outside of the section under study and may be highly dependent on the system as a whole. This was also true of the collapsible-tube experiment. The pressure fluctuation in this case being caused by the self-excitation of the tube which derived its energy from the constant upstream head and was also

dependent on the downstream section. Therefore, the application of the experimentally recorded values as boundary conditions in the FSI model and then drawing comparison with the experimental results was not exactly a like-for-like comparison. However, the forced unsteady model still showed some qualitative agreement with the experiment.

In this research it was necessary to sacrifice a certain degree of mesh and time-step independence in order to achieve realistic solution times and only qualitatively accurate results. It is clear that further work is needed to quantitatively validate the FSI facilities in LS-DYNA. This investigation has travelled a long way towards that goal and from here the validation procedures that need to be followed are much clearer. The applications of FSI in LS-DYNA will, in time, become feasible. However, this feasibility is dependent on increases in computing speeds and to a lesser extent computer memory. With the current trend for computing speed to double every eighteen months and the suitability of the explicit method for parallel processing it may be sooner, rather than later, that mesh and time-step independent solutions of the collapsible-tube model become viable.

9 Conclusions

The collapsible-tube experiment was used as a tool for comparison and validation of the (FSI) facilities in the explicit finite element code LS-DYNA. A finite element analysis was performed that modelled the collapsible-tube experiment in both steady and unsteady states. This finite element model contained internal fluid flow; external, inlet and outlet pressures; tube-wall tension; pre-stressing from a flat profile; and contact with the annular faces of the inlet and outlet sections.

This research fell short of a thorough quantitative validation of the code due to known uncertainties in the computer model. These uncertainties were present due to approximations made in order to reduce CPU times to acceptable levels. These approximations were a) a mesh resolution that failed to achieve a sufficiently accurate mesh independent solution, b) a reduced speed of sound in the fluid in order to increase the time-step and c) an altered tube material model.

Although sufficiently accurate mesh independence could not be achieved for practicable solution times the steady-state results still showed good agreement with experiments (Figure 7.6 and Figure 7.7). The resultant position of the pinch at the downstream end differed by just 5.6% of the tube diameter in the worst case.

The unsteady collapsible tube model showed some agreement with the experiment even though the oscillation of the tube was produced via unsteady boundary conditions instead of being self-excited, as was the case in the experiment. The successful modelling of vortex shedding from a circular cylinder indicated that the modelling of self-excited oscillations in the collapsible tube model is achievable with the correct boundary conditions and with an acceptable mesh resolution.

LS-DYNA was proven to be qualitatively valid but with current computing resources the viability, in terms of CPU expense, of modelling the collapsible-tube and similar phenomenon using the explicit technique is currently highly questionable.

10 Acknowledgements

The author would like to thank Ove Arup and Partners for software, technical support and funding; the Engineering and Physical Sciences Research Council for funding; and the various members of the Soft Structures research group (previously the Heart Valve research group) in particular C. J. Carmody and Dr A. Yoxall for assistance with the analysis software and Dr S. B. M. Beck, Professor E. A. Patterson and Professor I. Howard for many helpful discussions. The author would also like to acknowledge the contribution of the technical support staff in the Department of Mechanical Engineering for their help in the construction of the collapsible tube experiment.

11 References

1 Bluestein, D., Schoephoerster, R. T., Simulation Of Turbulent Pulsatile Flow Past A Mechanical Heart Valve, ASME Advances In Bioengineering, BED-Vol 33, pp 285 - 286, 1996.

2 Wang, J. H., Guo, G., Schreck, S., Prisco, M., A Numerical Study of Flow Through a Mechanical Heart Valve, ASME Advances in Bioengineering, BED- Vol 33, PP 275 – 276, 1996.

3 LS-DYNA, Livermore Software Technology Corp, Livermore, California, 2000

4 Patterson, E. A., Howard, I. C., Thornton, M. A., A Comparative Study Of Linear And Nonlinear Simulations Of The Leaflets In A Bioprosthetic Heart Valve During The Cardiac Cycle, Journal Of Medical Engineering And Technology, Vol 20, pp 95 - 108, 1996.

5 Carmody, C. J., Howard, I. C., Patterson, E. A., Chew, G. G., Some Examples of Coupled Fluid-Structural Analysis, First European LS-DYNA Users Conference, March 1997.

6 Patterson, E. A., Carmody, C. J., Howard, I. C., Simulating the Motion of Heart Valves Under Fluid Flows Induced by Cardiac Contraction, Sixth International LS-DYNA Users Conference, 9^{th}-11^{th} April 2000, Dearborn, Michigan, Livermore Software Technology Corp, Livermore, California.

7 Patterson, S. W., Piper, H., Starling, E. H., The Regulation of the Heart Beat, Journal of Physiology, Vol 48, pp 465, 1914.

8 Holt, J. P., The Collapse Factor in the Measurement of Venous Pressure: The Flow of Fluid Through Collapsible Tubes, American Journal of Physiology, Vol 134, pp 292 – 299, 1941.

9 Conrad, W. A., Pressure-Flow Relationships in Collapsible Tubes, IEEE Transactions on Bio-Medical Engineering, Vol BME-16, pp 284 – 295, 1969.

10 Brower, R. W., Noordergraaf, A., Pressure-Flow Characteristics of Collapsible Tubes: A Reconciliation of Seemingly Contradictory Results, Annals of Biomedical Engineering, Vol 1, pp 333 – 355, 1973.

11 Katz, A. I., Chen, Y., Moreno, A. H., Flow Through a Collapsible Tube: Experimental Analysis and Mathematical Model, Biophysical Journal, Vol 9, pp 1261 – 1279, 1969.

12 Holt, J. P., Flow of Liquids Through Collapsible Tubes, Circulation Research, Vol 7, pp 342 - 353, 1959.

13 Rodbard, S., Flow Through Collapsible Tubes: Augmented Flow Produced by Resistance At the Outlet, Circulation, Vol 11, pp 280 – 287, 1955.

14 Rodbard, S., Saiki, H., Flow Through Collapsible Tubes, American Heart Journal, Vol 46, pp 715 - 725, 1953.

15 Bertram, C. D., Pedley, T. J., A Mathematical Model of Unsteady Collapsible Tube Behaviour, Journal of Biomechanics, Vol 15, pp 39 – 50, 1982.

16 Pedley, T. J., Longitudinal Tension Variation in Collapsible Channels: A New Mechanism for the Breakdown of Steady Flow, ASME Journal of Biomechanical Engineering, Vol 114, pp 60 – 77, 1992.

17 Brower, R. W., Scholten, C., Experimental Evidence of the Mechanism for the Instability of Flow in Collapsible Vessels, Medical and Biological Engineering, Vol 13, pp 839 – 845, 1975.

18 Kounanis, K., Mathioulakis, D. S., Experimental Flow Study Within a Self Oscillating Collapsible Tube, Journal of Fluids and Structures, Vol 13, pp 61 – 73, 1999.

19 Bertram, C. D., Unstable Equilibrium Behaviour in Collapsible Tubes, Journal of Biomechanics, Vol 19, pp 61 – 69, 1986.

20 Bertram, C. D., Raymond, C. J., Butcher, K. S. A., Oscillations in a Collapsed-Tube Analog of the Brachial Artery Under a Sphygmomanometer Cuff, Journal of Biomechanical Engineering, Vol 111, pp 185 – 191, 1989.

21 Bertram, C. D., Raymond, C. J., Pedley, T. J., Mapping of Instabilities For Flow Through Collapsed Tubes of Differing Length, Journal of Fluids and Structures, Vol 4, pp 125 – 153, 1990.

22 Bertram, C. D., The Dynamics of Collapsible Tubes, Biological Fluid Dynamics, edited by Ellington, C. P., Pedley, The Company of Biologists Ltd, Cambridge, pp 253-264, 1995.

23 Cancelli, C., Pedley, T. J., A Separated Flow Model for Collapsible Tube Oscillations, Journal of Fluid Mechanics, Vol 157, pp 375 – 404, 1985.

24 Shapiro, A. H., Steady Flow in Collapsible Tubes, ASME Journal of Biomechanical Engineering, Vol 99, pp 126 – 147, 1977.

25 Kamm, R. D., Shapiro, A. H., Unsteady Flow in a Collapsible Tube Subjected to External Pressure or Body Forces, Journal of Fluid Mechanics, Vol 95, pp 1-78, 1979.

26 Shapiro, A. H., Physiologic and Medical Aspects of Flow in Collapsible Tubes, Proceedings of the 6^{th} Canadian Congress of Applied Mechanics, pp 883 – 906, 1977.

27 Rast, M. P., Simultaneous Solution of the Navier-Stokes and Elastic Membrane Equations by a Finite Element Method, International Journal for Numerical Methods in Fluids, Vol 19, pp 1115 – 1135, 1994.

28 Luo, X. Y., Pedley, T. J., A Numerical Simulation of Steady Flow in a 2-D Collapsible Channel, Journal of Fluids and Structures, Vol 9, pp 149 – 174, 1995.

29 Luo, X. Y., Pedley, T. J., A Numerical Simulation of Unsteady Flow in a Two-Dimensional Collapsible Channel, Journal of Fluid Mechanics, Vol 314, pp 191 – 225, 1996.

30 Heil, M., Stokes Flow in Collapsible Tubes: Computation and Experiment, Journal of Fluid Mechanics, Vol 353, pp 285 – 312, 1997.

31 Bathe, K. J., Zhang, H., Shanhong, J., Finite Element Analysis of Fluid Flows Fully Coupled With Structural Interactions, Computers and Structures, Vol 72, pp 1 – 16, 1999.

32 Bathe, K. J., Dong, J., Solution of Incompressible Viscous Fluid Flow with Heat Transfer Using Adina-F, Computers and Structures, Vol 26, pp 17 – 31, 1987.

33 Tang, D., Yang, C., Huang, Y., Ku, D. N., Wall Stress and Strain Analysis Using a Three-Dimensional Thick-Wall Model With Fluid-Structure Interactions for Blood Flow in Carotid Arteries with Stenosis, Computers and Structures, Vol 72, pp 341 – 356, 1999.

34 Bathe, M., Kamm, R. D., A Fluid-Structure Interaction Finite Element Analysis of Pulsatile Blood Flow Through a Compliant Stenotic Artery, ASME Journal of Biomechanical Engineering, Vol 121, pp 361 – 369, 1999.

35 Wang, X., Velocity/Pressure Mixed Finite Element and Finite Volume Formulation with ALE Descriptions for Nonlinear Fluid-Structure Interaction Problems, Advances in Engineering Software, Vol 31, pp 35 – 44, 2000.

36 Peskin, C. S., McQueen, D. M., A General Method for the Computer Simulation of Biological Systems Interacting with Fluids, Biological Fluid Dynamics, edited by Ellington, C. P., Pedley, T. J., The Company of Biologists Ltd, Cambridge, pp 265-276, 1995.

37 York, A. R., Sulsky, D., Schreyer, H. L., Fluid-Membrane Interaction Based on the Material Point Method, International Journal For Numerical Methods In Engineering, Vol 48, pp 901 – 924, 2000.

38 Chen Da-peng, Zhang Jian-hai, Transient Analysis Of Artificial Mechanical Valve-Blood Interaction, Applied Mathematics and Mechanics (English Edition), Vol 16, pp 437 - 442, 1995.

39 Soria, A., Casadi, F., Arbitrary Lagrangian-Eulerian Multicomponent Compressible Flow With Fluid-Structure Interaction, International Journal For Numerical Methods In Fluids, Vol. 25, pp 1263 - 1284, 1997.

40 Anju, A., Maruoka,A., Kawahara, M., 2-D Fluid-Structure Interaction Problems By An Arbitrary Lagrangian-Eulerian Finite Element Method, International Journal of Computational Fluid Dynamics, Vol 8, pp 1 - 9, 1997.

41 Kerh, T., Lee, J. J., Wellford, L. C., Transient Fluid-Structure Interaction In A Control Valve, Transactions Of The ASME, Journal Of Fluids Engineering, Vol 119, pp 354 - 359, 1997.

42 Wang, Z., Tan, S. K., Coupled Analysis Of Fluid Transients And Structural Dynamic Responses Of A Pipeline System, Journal Of Hydraulic Research, Vol 35, pp 119 - 131, 1997.

43 Heinsbrook, A. G. T. J., Fluid-Structure Interaction In Non-Rigid Pipeline Systems, Nuclear Engineering And Design, Vol 172, pp 123 - 135, 1997.

44 Benney, J. B., Stein, K. R., Computational Fluid-Structure Interaction Model of Parachute Inflation, Journal of Aircraft, Vol 33, pp 730 – 736, 1996.

45 Riemslagh, K., Vierendeels, J., Dick, E., Coupling of a Navier Stokes Solver and an Elastic Boundary Solver for Unsteady Problems, ECCOMAS 98, John Wiley and Sons Ltd, 1998.

46 Blom, F. J., Leyland, P., Consistency Analysis of Fluid-Structure Interaction Algorithms, ECCOMAS 98, John Wiley and Sons Ltd, 1998.

47 Bathe, K. J., Finite Element Procedures in Engineering Analysis, Prentice-Hall, Englewood Cliffs, New Jersey, 1982.

48 Benson, D. J., Computational Methods In Lagrangian And Eulerian Hydrocodes, Computer Methods In Applied Mechanics And Engineering, Vol 99, pp 235 - 394, 1992.

49 Hallquist, J. 0., LS-DYNA Theoretical Manual, Livermore Software Technology Corp, Livermore, California, 2000.

50 Hirt, C. W., Amsden, A. A., Cook, J. L., An Arbitrary Lagrangian-Eulerian Computing Method For All Flow Speeds, Journal Of Computational Physics, Vol 14, pp 227 - 253, 1974.

51 MSC.DYTRAN Users Manual, MSC Software, 815 Colorado Boulevard, LA, California, USA, 1999.

52 Jones, R. D., Kemp, M. D., An Overview of Explicit Finite Element Technology in Industry, BENCHmark, pp 8 – 12, October 1999.

53 ADINA, ADINA R and D, Watertown, MA, December 1999.

54 MSC.DYTRAN Version 4.7, MSC Software, 815 Colorado Boulevard, LA, California, USA, 1999.

55 Souli, M., LS-DYNA Advanced Course In ALE And Fluid/Structure Coupling, Livermore Sortware Technology Corporation, Livermore, California, 1998.

56 VonNuemann, J., Richtmyer, R. D., A Method For The Calculation Of Hydrodynamic Shocks, Journal Of Applied Physics, Vol 21, pp 232 - 237, 1950.

57 Wilkins, M. L., Use Of Artificial Viscosity In Multidimensional Fluid Dynamic Calculations, Journal of Computational Physics, Vol 36, 381 - 403, 1980.

58 OASys LS-DYNA Environment 8.0, OASys Limited, 13 Fitzroy Street, London, 2000.

59 ANSYS, Proprietary Software, Swanson Analysis Systems Inc., 1997.

60 Thornton, M. A., Chew, G. G., Yoxall, A., DYNASYS - An Interface Between ANSYS and OASYS LS-DYNA3D. Proprietary Software, Department of Mechanical and Process Engineering, The University of Sheffield, 1996.

61 HyperMesh, Altair Engineering, Pury Hill, Northamptonshire, 2000.

62 American Society of Mechanical Engineers (ASME), Editorial Policy Statement on the Control of Numerical Accuracy, ASME Journal of Fluids Engineering, Vol 115, 340 - 340, 1993.

63 Coleman, H. W., Stern, F., Uncertainties and CFD Code Validation, ASME Journal of Fluids Engineering, Vol 119, 795 – 803, 1997.

64 Bathe, K. J., What Can Go Wrong in FEA, Mechanical Engineering, May 1998, 63 – 65, 1998.

65 Nakayama, T., Matsuzawa, R., Finite Element Analysis of Flow-Induced Vibration of a Two-Dimensional Rigid Body Using Composite Overlapping Meshes, ECCOMAS 98, John Wiley and Sons Ltd, 1998.

66 Mendes, P. A., Branco, F. A., Analysis of Fluid-Structure Interaction by an Arbitrary Lagrangian-Eulerian Formulation, International Journal of Numerical Methods in Fluids, Vol 30, pp 897 – 919, 1999.

67 Massey, B. S., Mechanics of Fluids 6th Edition, Chapman and Hall, London, 1989.

68 VanDyke, M., An Album of fluid motion, Parabolic Press, Stanford, California, 1982.

69 LS-DYNA User Guide, OASys Limited, 13 Fitzroy Street, London, 1998.

A. Physiological Examples of Collapsible Tubes

Nature's use of non-rigid materials is apparent when considering the components and their specific functions within the bodies of living beings. Physiological components such as the heart and lungs have mechanical properties that are exquisitely tuned to the tasks they perform. The flexibility of such components and the arteries that feed them is vital to their continuing performance.

Let us take as an example the vessels that carry blood from the heart and deliver it around the body before returning it back to the heart. Considering that this is a closed, circulatory system, the heart could not possible function if the system consisted entirely of rigid vessels. In its systolic squeeze, the chambers of the heart get smaller as the blood is forced out; liquids are not easily compressed so with a rigid system the heart would not be able to eject any blood unless another part of the system could expand.

The collapsible tube experiment has been used as an analogue for many different physiological tubes. Some examples are given below.

A.1 Veins

Where arteries are designed to remain distended, veins are required to distend and collapse. Veins sustain much lower pressures than do arteries, and their mechanical properties are, not unexpectedly, different. The walls of veins are five to ten times thinner than the walls of corresponding arteries. They are highly compliant vessels that exhibit large area changes in response to small changes in transmural pressure. The transmural pressure that a vein is subjected to is therefore much more significant than in the case of an artery.

Holt [70] observed that the veins entering the upper end of the thoracic cage in a living dog were seen to be normally partially collapsed or to dilate and collapse synchronously with respiration. Holt's experiments on collapsible tubes were directly related to the collapsible nature of veins. Holt used the excised jugular vein of a dog to perform these experiments.

Holt modelled the collapse of veins using an inclined collapsible tube and gave a good description of the phenomenon using the flow of blood form the aorta to the head of a giraffe as an example. "Only a relatively small amount of energy is required to move a given quantity of blood from the aorta to the head when the head is at heart level. However, a much larger amount of energy is needed to raise the same amount of blood when the head is in the vertical position because of the large difference in potential energy. This large amount of energy is dissipated in the form of heat when the blood flows back to the heart through the collapsed veins in the neck where the resistance is large and the velocity high. It would appear that the collapse of veins in the neck of a giraffe is a protective mechanism that tends to maintain the pressure in the capillaries of the head above atmospheric. It also dissipates the large amount of potential energy that the blood possesses at head level on its return to the heart in this way the blood returns to the heart without excessive kinetic energy."

Pedley [71] and Hargens [72] also investigated the gravitational haemodynamics of the giraffe. In particular they studied how the physiology of the giraffe prevents Oedema, the accumulation of fluid in the tissue spaces of the body. An upright giraffe, by analogy with humans, ought to suffer massive oedema in its feet [71].

However, the tight skin and fascial layers of the giraffe leg provide a functional 'antigravity suit' to prevent this [72].
Kresch and Noordergraaf [73] constructed a mathematical pressure-flow relationship in a segment of vein. They found it necessary to take into account the non-linear phenomenon represented by the changes in the cross-sectional shape that can occur because of the low pressure found within the veins. The collapsible tube analogy was therefore used. This was a phenomenon that they found unnecessary in their mathematical models for arteries since they don't tend to collapse.
The collapse of the veins is easily viewed by performing a simple experiment. Distended veins can be seen on the back of the hand when it is held below the level of the heart. As the hand is raised up to the heart level these veins visibly collapse.

A.2 Arteries

The condition *atherosclerosis* is the commonest form of arterial disease in Western societies [74] and is defined as the thickening of and rigidity of the arteries. The result of *atherosclerosis* is that the circulatory system lacks sufficient compliance and requires a higher pressure to push blood through the capillaries at an adequate rate. This, of course, causes the heart to be unduly stressed.
The flexibility inherent in the material of arteries is for the purposes of storing blood during systole and ejecting it during diastole. Flexible arteries also smooth out the abrupt changes in pressure and flow that can be caused by the opening and slamming shut of valves within the beating heart. Arteries are analogous to capacitors in an electrical system, which smooth out the sudden voltage load when a switch is turned on; or a surge tank in a piping system, used to eliminate waterhammer caused by sudden valve closure or pump trip.
Normally, the arteries have a positive transmural pressure, and are therefore distended. However, large accelerations due to impact or aircraft and space vehicle manoeuvres may alter the internal pressure distribution in an artery as to make the transmural pressure negative and result in vessel collapse.

A.3 Lungs

Pulmonary capillaries are easily collapsible by reason of their highly compliant walls and their geometry. These characteristics have important consequences to the regulation and distribution of blood flow. The alveoli (a small cavity of the lungs) more or less surrounds the pulmonary capillaries, thus making the shape and cross sectional area of the capillaries strongly dependent upon the relative levels of alveolar pressure, pulmonary arterial pressure, and pulmonary venous pressure. Lopiz-muniz [75] explored the limitations of the collapsible tube model as applied to the pulmonary circulation in the excised lung of a dog and determined that under certain conditions the alveolar pressure can be considered the effective external pressure surrounding the collapsible blood vessels of the lungs. The collapsible tube model was therefore considered a sufficient approximation of this phenomenon.
During forced expiration of air from the lungs the flow rate is found to reach a maximum value, dependent on lung volume, as pleural (watery membrane lining the pulmonary cavity) pressure is increased [76]. In a collapsible tube model, the flow limits when the flow velocity equals the speed of propagation of pressure pulse waves at some point within the tubes.

A.4 Autoregulation of Blood Flow

In a number of different tissues the blood flow appears to be adjusted to the existing metabolic activity of the tissue. Furthermore, imposed changes in the arterial blood pressure at constant levels of tissue metabolism are met with vascular resistance changes that tend to maintain a constant blood flow. This mechanism is commonly referred to as autoregulation.

A plausible mechanism of the autoregulation phenomenon involves flow in collapsible tubes. Rodbard [77] studied autoregulation as demonstrated in a modified version of the collapsible tube experiment in which the arterial stream communicated with the extravascular fluid compartment in order to model various levels of permeability of the capillary wall. Rodbard suggested that a variation in this degree of permeability could cause changes in the extravascular pressure surrounding the capillary, thereby changing the cross-sectional area and thus the flow resistance. He summarised that the phenomenon of autoregulation may be a mechanical property of the effect of flow on the wall of enclosed collapsible vessels.

A.5 Urethra

While most of the urethra is normally distended during micturition (mammalian urination), certain portions are partially collapsed by reason of sufficiently low intraurethral pressure. Griffiths [78, 79] concluded that in males the urethra behaves like a thin-walled elastic tube. In the typical male urethra during micturition there appear to be two sonic constrictions separated by a hydraulic jump. The first of these, which is near the junction of the prostatic and membranous parts of the urethra, determines the flow rate (in conjunction with the bladder pressure and the energy losses between the bladder and the constriction) (Figure 11.1).

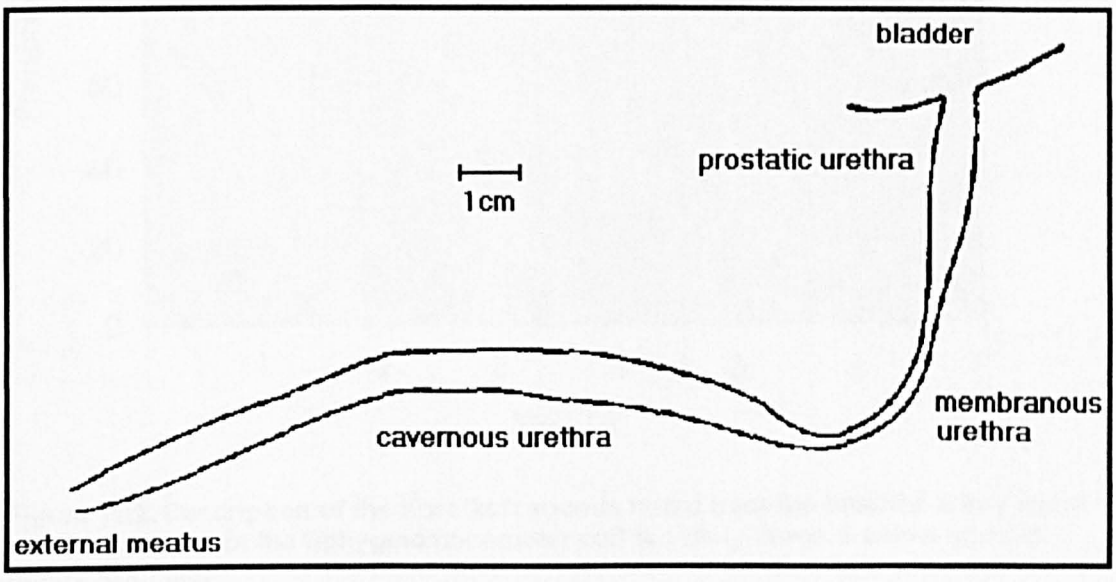

Figure 11.1. The mammalian male Urethra. Figure from [78]

The second constriction, which is near the external meatus, is expected, in conjunction with the energy losses between the constriction and the meatus, to control the speed of the urine stream for the given flow rate.

A.6 Diagnostic Equipment

There are a variety of diagnostic procedures that involve flow in collapsible tubes for which an understanding of such flows offers insights. Measurement of blood pressure in humans is normally carried out using a Sphygmomanometer and the auscultatory method. A Sphygmomanometer consists of an inextensible cuff containing an inflatable bag. The cuff is wrapped around the arm so that the inflatable bag lies between the cuff and the skin, directly over the artery to be compressed. Inflating the bag to a pressure in excess of arterial systolic pressure occludes the artery. The practitioner listens with a stethoscope applied to the skin of the antecubital (in front of the elbow) space over the brachial artery. While the pressure in the bag exceeds systolic pressure, the brachial artery is occluded and no sounds are heard. Pressure is slowly released from the bag so that it falls below systolic pressure. When this happens the artery opens, blood escapes through the cuff and a slight tapping sound is heard with every heartbeat (Korotkoff sounds). The pressure at which the first sound is detected represents the systolic pressure (point A in Figure 11.2).

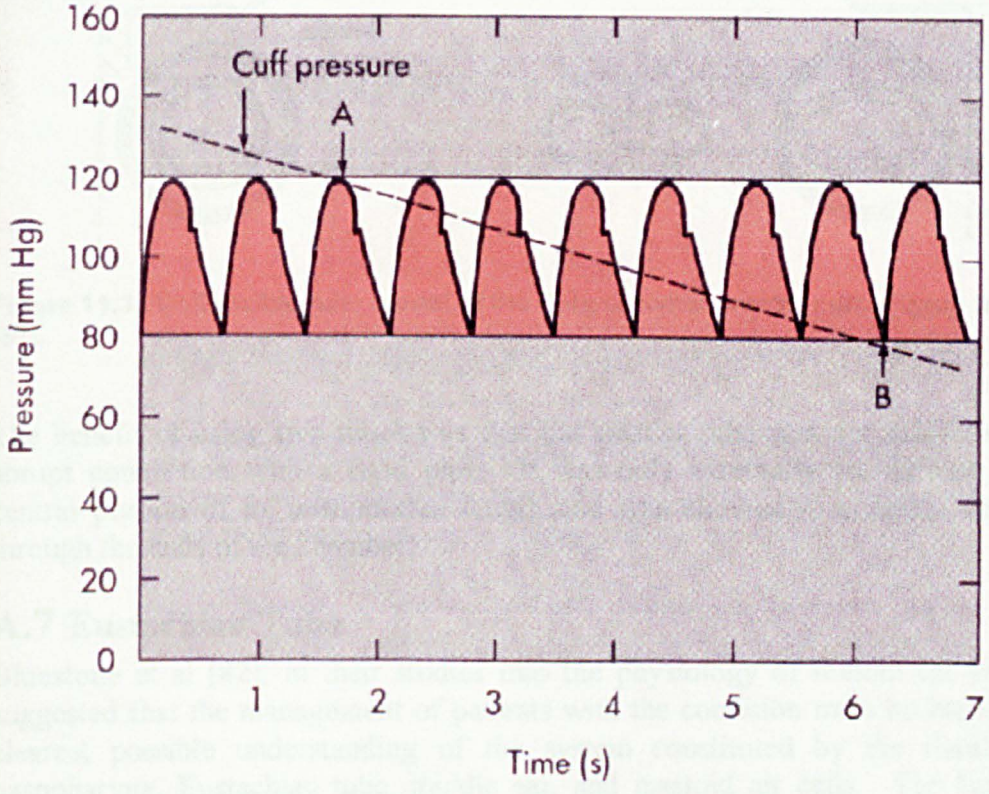

Figure 11.2. Description of the Korotkoff sounds heard from the brachial artery when the the pressure of the Sphygmomanometer cuff is slowly lowered below systolic. Figure from [80]

As inflation pressure is decreased further, more blood escapes through the cuff and the Korotkoff sounds become louder. The sounds become muffled as the inflation pressure nears the diastolic pressure and they disappear altogether once inflation pressure falls below diastolic pressure (point B) and flow is continuous in the brachial artery.

Bertram et al [81] experimentally modelled the brachial artery under a Sphygmomanometer cuff by using a modified version of the collapsible tube set-up.

In this set-up a collapsible tube (brachial artery) was passed through a second collapsible tube of larger diameter and shorter length (Sphygmomanometer cuff) which was mounted within a pressure container in the fashion of the standard collapsible tube set-up. Fluid flowed through the smaller tube while the larger tube was subjected to an external pressure thus collapsing both larger and smaller tubes.

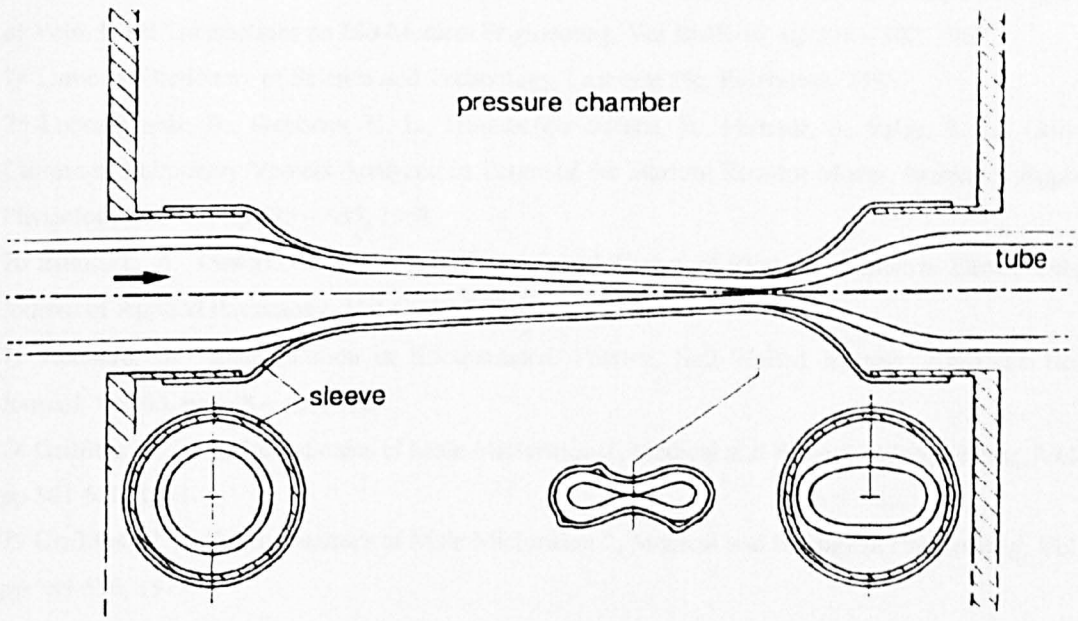

Figure 11.3. Collapsible tube model of the Sphygmomanometer cuff. Figure from [81].

The benefit of using two tubes was that the smaller tube was not subjected to the abrupt connection with a rigid pipe. It was only externally pressurised along a central portion of its unsupported length and was allowed to continue collapsing through the ends of the chamber.

A.7 Eustachian Tube

Bluestone et al [82], in their studies into the physiology of middle ear effusions, suggested that the management of patients with the condition must be based on the clearest possible understanding of the system constituted by the nasal cavity, nasopharynx, Eustachian tube, middle ear, and mastoid air cells. The Eustachian tube is a relatively long narrow channel that connects the middle ear cavity to the oral cavity. Its compliance appears to play an important role in determining its function. In particular, compliance appears to be an important factor in the response of the Eustachian tube to increased positive or negative pressures. The Eustachian tube probably has at least three physiological functions with respect to the middle ear: ventilation, protection from unwanted nasopharyngeal secretions, and drainage of normal or abnormal secretions produced within the middle ear itself. The ventilation of the middle ear involves flow of a gas through a compliant collapsible tube.

70 Holt, J. P., The Collapse Factor in the Measurement of Venous Pressure: The Flow of Fluid Through Collapsible Tubes, American Journal of Physiology, Vol 134, pp 292 – 299, 1941.

71 Pedley, T. J., How Giraffes Prevent Oedema, Nature, Vol 329, pp 13 – 14, 1987.

72 Hargens, A. R., Millard, R. W., Petterson, K., Johansen, K., Nature, Vol 329, pp 59 – 60, 1987.

73 Kresch, E., Noordergraaf, A Mathematical Model for the Pressure-Flow Relationship in a Segment of Vein, IEEE Transactions on Bio-Medical Engineering, Vol BME-16, pp 296 – 307, 1969.

74 Larousse Dictionary of Science and Technology, Larousse Plc, Edinburgh, 1995.

75 Lopez-Muniz, R., Stephens, N. L., Bromberger-Barnea, B., Permutt, S., Riley, R. L., Critical Closure of Pulmonary Vessels Analyzed in Terms of the Starling Resistor Model, Journal of Applied Physiology, Vol 21, pp 625 – 635, 1968.

76 Elliott, E. A., Dawson, S. V., Test of Wave Speed Theory of Flow Limitation in Elastic Tubes, Journal of Applied Physiology, Vol 43, pp 516 – 522, 1977.

77 Rodbard, S., Autoregulation in Encapsulated, Passive, Soft-Walled Vessels, American Heart Journal, Vol 65, pp 648 – 655, 1963.

78 Griffiths, D. J., Hydrodynamics of Male Micturition-1, Medical and Biological Engineering, Vol 9, pp 581-588, 1971.

79 Griffiths, D. J., Hydrodynamics of Male Micturition-2, Medical and Biological Engineering, Vol 9, pp 589-596, 1971.

80 Berne, R. M., Levy, M. N., Cardiovascular Physiology, Mosby, Missouri, 1986.

81 Bertram, C. D., Raymond, C. J., Butcher, K. S. A., Oscillations in a Collapsed-Tube Analog of the Brachial Artery Under a Sphygmomanometer Cuff, Journal of Biomechanical Engineering, Vol 111, pp 185 – 191, 1989.

82 Bluestone, C. D., Paradise, J. L., Berry, Q. C., Physiology of the Eustachian Tube in the Pathogenesis and Management of Middle Ear Effusions, Laryngoscope, Vol 82, pp 1654-1670, 1972.

B. Calculation of Glass Thickness

For a plate of glass of dimensions 300 x 300 mm the thickness required to withstand a uniform pressure of 22 kPa was calculated using the following equation [83]

$$\sigma_{max} = C\frac{3}{4}P\left(\frac{L}{w}\right)^2 \tag{33}$$

where σ_{max} is the maximum bending stress (Typical allowable stress for plate glass is 7 Mpa); P is the internal pressure; L is the distance across the shortest side of the plate; w is the wall thickness; and C is a factor relating to the ratio of the lengths of the two sides of the plate. In this case C = 0.45. This gives a glass thickness of 10 mm.

---

83 Bowes, W. H., Russell, L. T., Suter, G. T., Mechanics of Engineering Materials, John Wiley and Sons, New York, 1984.

C. The Conrad Experiments

The experiments performed by Conrad [84] were repeated in order to gain a better understanding of the collapsible tube phenomena. A section of Penrose tube was mounted on the inlet and outlet sections so that an undeformed length of 66mm occupied the 65mm gap. The 1mm of slack was taken up by the radial tension and subsequent axial tension caused by the inlet and outlet tubes being of larger diameter (17mm) than the undeformed Penrose tube diameter (13mm).

C.1 Method

The Conrad experiments consisted of three different families of curves. Each family consisted of several characteristic curves. The membership of a curve to a family was determined by the relationship between external pressure, P_E, and downstream resistance, R_2. R_2 was measured by the formula $P_2 = R_2Q^2$ when the tube was distended.

The method employed for each curve of a family was to fix external pressure P_E at some value above the outlet reservoir pressure ($P_E - P_O$ = constant). The downstream constriction, R_2, was also fixed for each subset. P_1 and P_2 (measured relative to P_O) were free to vary as the flow was varied. This control of flow was achieved by opening or closing the upstream resistance R_1.

For each family P_E was altered for each curve from 60cmH_2O down to 20cmH_2O, in increments of 10cmH_2O. The experiments were performed from high flow rates to low flow rates i.e. from distended tube to collapsed tube.

C.2 Results

C.2.1 P_E Varied, R_2 Constant

The membership of this family was determined by the value of R_2. The membership of each subset was determined by the value of P_E. The downstream resistance R_2 was set to 38 cmH_2O/(litres/min)^2.

The characteristic curves are shown in Figure 0.1.

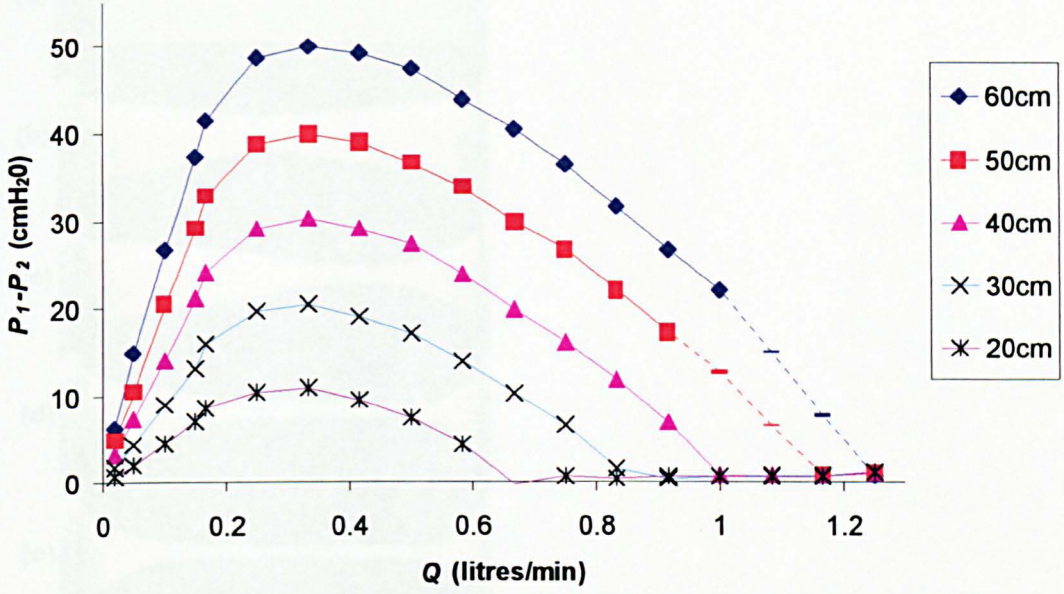

Figure 0.1. Characteristic curves resulting when P_E(legend) is varied and R_2 is held Constant. Dashed lines denote oscillations

By viewing the results in Figure 0.1 it can be seen that the flow rate at tube collapse, Q_{VP}, is different for all the curves. The larger the value of P_E the larger the value of Q_{VP}. It is also interesting to note that the peak $P_1 - P_2$ values all occur at around the same value of Q and the magnitude of this $P_1 - P_2$ value increases proportionally with the value of P_E. The slopes of the curves up to this maximum value are different for each subset. However, the slopes from the peak $P_1 - P_2$ value to the valley points are all approximately the same.

The shape of the tube at various flow rates for the subset $P_E = 40\text{cmH}_2\text{O}$ can be seen in Figure 0.2.

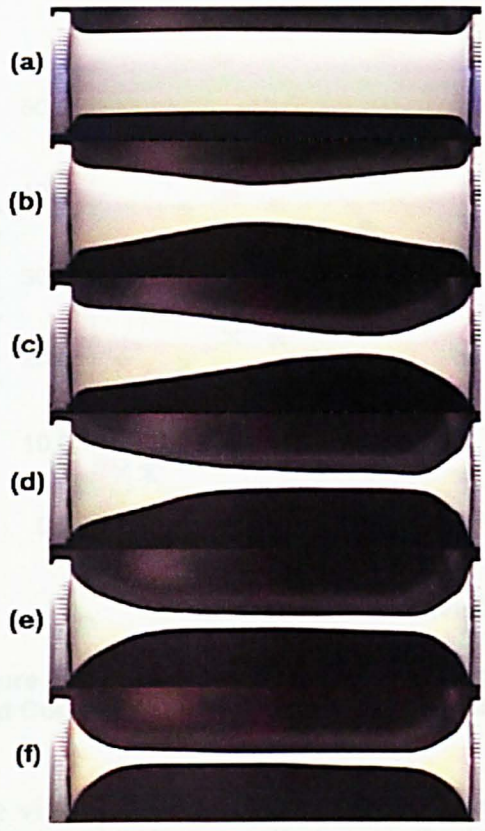

Figure 0.2. Side profile of the tube when P_E = 40cmH_2O, R_2 = 38 cmH_2O/(litres/min)^2 (a) 1.25 litres/min; (b) 1 litres/min, Q_{VP}; (c) 0.92 litres/min; (d) 0.33 litres/min, peak value of $P_1 - P_2$; (e) 0.17 litres/min; (f) 0.02 litres/min

The tube started off distended with a high flow rate (Figure 0.2(a)). This is shown on the right hand side of the graph in Figure 0.1 where P_1 - P_2 is near 0. Working from right to left, at some value of Q, referred to as the valley point flow rate (Q_{VP}), the upstream pressure P_1 tended to P_E and the tube became pinched off near the centre (b). The tube then collapsed towards the outlet end as the flow rate was further reduced (c). In some cases, with larger P_E values, oscillations were observed just after tube collapse which only died out with further reductions in Q. These are shown as dashed lines on the graph in Figure 0.1.

After tube collapse the value for $P_1 - P_2$ was greatly increased for every small decrease in flow rate Q. In other words resistance to flow was increased as the flow rate was reduced. The value of $P_1 - P_2$ continued to rise until it reached its peak value at 0.3 litres/min.

As the flow was reduced from this point the line contact at the downstream end of the tube began to spread upstream leaving only two small channels either side of the flattened area (e). As the flow rate tended to zero the entire tube was collapsed (f).

C.2.2 Ratio P_E : R_2 Constant

For the second family of curves the ratio of P_E to R_2 was held constant for all of the subsets. Again, values of 60cmH_2O to 20cmH_2O through increments of 10cmH_2O were used for the subsets and the R_2 values were altered accordingly. The characteristic curves are shown in Figure 0.3.

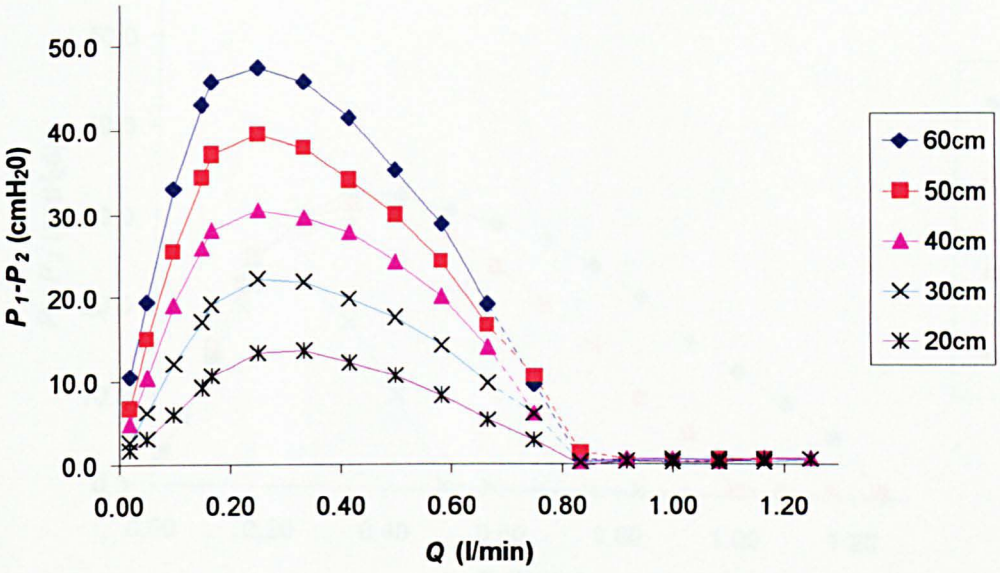

Figure 0.3. Characteristic curves resulting when Ratio P_E (legend): R_2 = 1.32 and is held Constant. Dashed lines denote oscillations.

The visible response of the tube followed the same qualitative pattern described in Figure 0.2. Differences in the quantitative responses were observed however.
The setting of a constant ratio of $P_E : R_2$ resulted in tube collapse at the same flow rate for all the subsets (Q_{VP} = 0.9 litres/min). Peak $P_1 - P_2$ values were reached at the same value of Q for all subsets (Q = 0.33 litres/min). Oscillations were observed for lower values of P_E than when P_E was varied at constant R_2.

C.2.3 P_E Constant, R_2 Varied

In the third family of curves P_E was held constant at 40cmH_2O while R_2 was varied arbitrarily. The characteristic curves are shown in Figure 0.4.

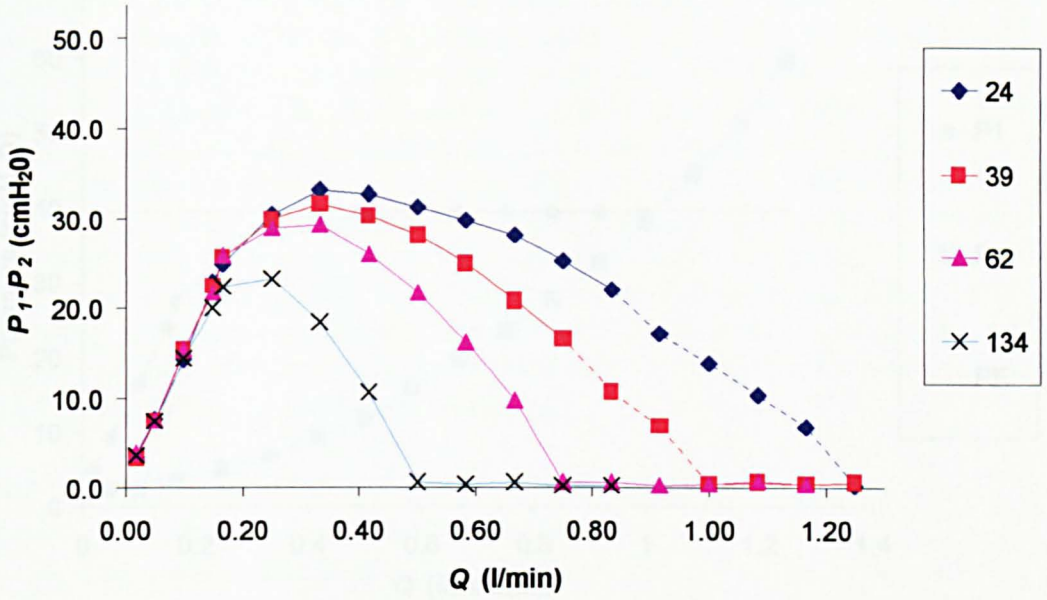

Figure 0.4. Characteristic curves resulting when P_E is held constant at 40 cmH$_2$O while R_2 is varied. Legend represents R_2 (cmH$_2$O/(litres/min)^2)

Again, the same qualitative response was observed for each individual curve but there were quantitative differences. As a family of curves it can be seen that the slopes of the curves at the low flow end (left-hand side) of the graph are all the same. The peak $P_1 - P_2$ values occurred at different flow rates. Q_{VP} is also different for each subset. Oscillations were observed for the lower values of R_2.

C.3 Discussion Of Conrad's Experiments

For each of the three families each characteristic curve followed the same qualitative pattern and the same visible tube response as that depicted in Figure 0.2. However, when the curves were grouped together as families several quantitative differences became apparent.

The subsets of Figure 0.1 and Figure 0.4 all exhibited different values of Q_{VP} whereas the subsets of Figure 0.3 all had the same Q_{VP} value. We know that for flow through an open tube $P_2 = R_2Q^2$ and at the valley point $P_2 = P_E$ (Figure 0.5), therefore substituting we get $Q_{VP} = (P_E/R_2)^{½}$. This mathematically predicts that the valley point is the same for any positive value of P_E when the ratio $P_E : R_2 =$ constant.

The slope of the curves between Q_{VP} and the peak value of $P_1 - P_2$ was the same for all the subsets of Figure 0.1. In Figure 0.3 the gradients can be seen to increase with increasing P_E and the opposite is true of Figure 0.4. In all the experiments this slope corresponds to a negative resistance.

This negative resistance can be better understood by analysing the relationship between P_1, P_2 and P_E as the flow rate was reduced (Figure 0.5)

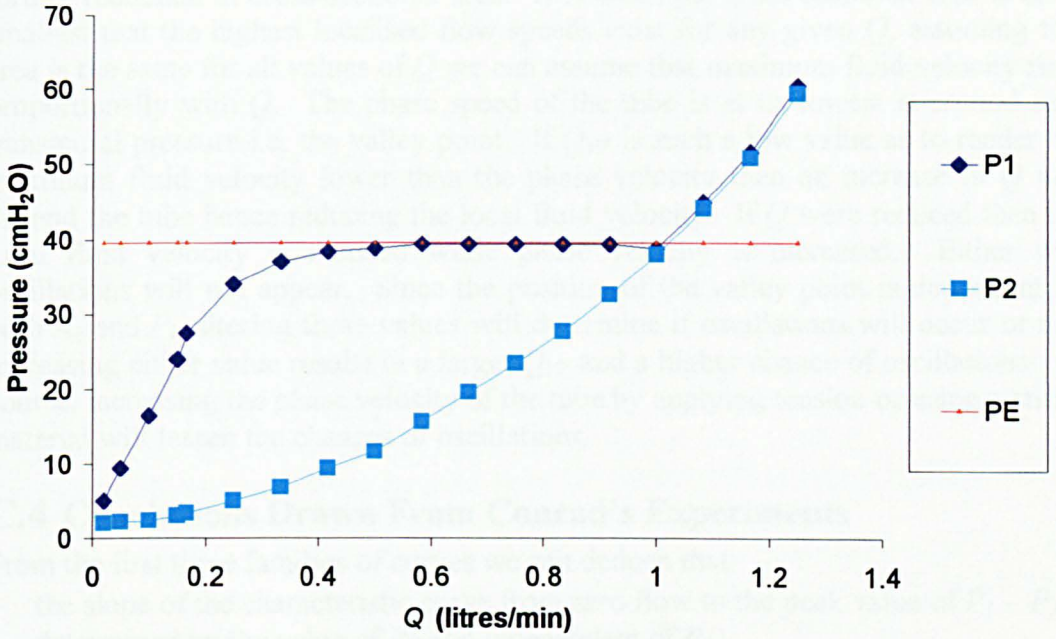

Figure 0.5. Relationship between P_1, P_2 and P_E

The valley point can be seen where the P_1, P_2 and P_E curves all join together, and corresponds to the transition from flow in an open tube to flow in a partially collapsed tube. As Q was reduced from Q_{VP}, P_1 remained roughly equal to P_E while P_2 continued to decrease, hence increasing $P_1 - P_2$ until it reached its maximum. The value of $P_E - P_2$ over this range can be seen to increase, thus the transmural pressure at the outlet end of the tube was gaining larger and larger negative values and the tube became further collapsed. This resulted in a reduction of cross-sectional area and an increased resistance to flow.

At some point as the flow was reduced, in all cases, the opposite walls of the tube contacted each other. The exact operating point where this happened is difficult to determine but this is not too important since even with contact the tube can remain highly compliant. What is important is the point at which the contact causes the structure of the tube to become rigid enough so as to require large changes in transmural pressure to cause any further reduction in cross-sectional area. It is at this point that the maximum value of $P_1 - P_2$ was reached in all cases. To the left of the point of largest $P_1 - P_2$ value the flow resistance reduces with a lowering of Q as in a Poiseuille flow and to the right the flow resistance reduces with a raising of Q as explained above (in reverse). The highly collapsed tube at low flow rate forms a rigid structure and Poiseuille's law is true, this can be seen by the linear nature of the curves of P_1 and P_2 up to $Q = 0.2$ litres/min in Figure 0.5.

The slopes of the curves from the peak $P_1 - P_2$ value to zero flow were different for each subset in Figure 0.1 and Figure 0.3 but had the same gradient for each subset of Figure 0.4. The gradient of this slope was therefore dependent on P_E and independent of R_2.

Oscillations were observed in all of the families of curves. These oscillations occurred just after tube collapse and as Q was lowered to a certain value they stopped suddenly.

It has already been explained that at a certain transmural pressure the tube takes on a rigid structure and it requires significant changes in transmural pressure to cause any

further reduction in cross-sectional area. It is when the cross-sectional area is at its smallest that the highest localised flow speeds exist for any given Q, assuming this area is the same for all values of Q we can assume that maximum fluid velocity rises proportionally with Q. The phase speed of the tube is at its lowest at around zero transmural pressure i.e. the valley point. If Q_{VP} is such a low value as to render the maximum fluid velocity lower than the phase velocity then an increase in Q will distend the tube hence reducing the local fluid velocity. If Q were reduced then the local fluid velocity is reduced while phase velocity is increased. Either way oscillations will not appear. Since the position of the valley point is dependent on both R_2 and P_E altering these values will determine if oscillations will occur or not. Increasing either value results in a larger Q_{VP} and a higher chance of oscillations. Of course, increasing the phase velocity of the tube by applying tension or using a stiffer material will lessen the chances of oscillations.

C.4 Conclusions Drawn From Conrad's Experiments

From the first three families of curves we can deduce that:

- the slope of the characteristic curve from zero flow to the peak value of $P_1 - P_2$ is determined by the value of P_E and independent of R_2
- the slope of the characteristic curve from peak $P_1 - P_2$ to the valley point is determined by the value of R_2 and independent of P_E
- the flow at which Q_{VP} occurs is determined by the ratio P_E: R_2

These relationships are qualitatively true. For different tubes of differing lengths the quantitative relationships would be different.

---

84 Conrad, W. A., Pressure-Flow Relationships in Collapsible Tubes, IEEE Transactions on Bio-Medical Engineering, Vol BME-16, pp 284 – 295, 1969.

D. Preforming of the Tube Wall in LS-DYNA

The technique for applying the displacement loads, in order to move the tube from the flat state to the circular cylindrical state is presented. The LS-DYNA template file for HYPERMESH version 3.1 did not allow the use of vectors when defining displacement loads. These displacement loads, therefore, needed to be defined as velocities since they could be defined with the use of vectors and were written out as separate loads in x, y and z via the LS-DYNA template. Displacements, velocities and accelerations in LS-DYNA input files all shared the same keyword (*BOUNDARY_PRESCRIBED_MOTION_NODE). The additional data needed to determine which type of load this keyword was requesting was provided via a single integer in one of the keyword cells. This meant velocities could be changed to displacements or accelerations very easily using a suitable text editor.

The process for preforming of the tube using HYPERMESH is shown below:

1) Create the geometry and mesh of the flat tube
2) Create a circle at one end of the tube on a plane perpendicular to the end set of nodes. The diameter of the circle should be that of the rigid inlet and outlet external diameters and should also share their axis.
3) Create temporary nodes on the circle so that each one corresponds to a row of nodes on the flat tube.
4) Measure and record the perpendicular distance between each temporary node and its corresponding row of nodes on the flat tube i.e. between the temporary node and the end node.
5) Create velocity loads for each row of nodes on a vector between the end node and the temporary node on the circle. Apply a magnitude of that measured in (4).
6) Apply a death time to all the loads other than at the ends of the tube.
7) Using the LS-DYNA template file write an LS-DYNA keyword file.
8) Edit the input file:
   a) change velocity definition to displacements,
   b) apply a different load curve to any displacements in the x direction or of zero magnitude in any direction. This load curve must be set to zero throughout the analysis. The load curve for the remaining loads should start at zero and go to 1 in a suitable time and then be held at 1 in order to maintain the constraints at the end of the tube.

E. Fortran Executable for Initial Stress Loads

After the LS-DYNA input file had been written out by HYPERMESH it was viewed using a text editor and the numbers of the shell elements that make up the tube determined. This element data was then saved in a separate file. The Fortran executable was then used to rewrite this data as *INITIAL_STRESS_SHELL keywords. This meant that an initial stress could be applied to each of the shell elements of the collapsible tube. The resulting data was then pasted back into the LS-DYNA keyword file. The Fortran executable is as follows:

```
PROGRAM TFILE
    INTEGER COUNT, EOF, EID, I1,I2,I3,I4,I5
    INTEGER NPLANE, NTHICK
    REAL TAW, SIGXX, SIGYY, SIGZZ, SIGXY, SIGYZ, SIGZX, EPS
    CHARACTER*20 FNAME
    DATA COUNT /0/
     NPLANE=1
     NTHICK=1
     TAW=0
     SIGXX=0
     SIGYY=10
     SIGZZ=0
     SIGXY=0
     SIGYZ=0
     SIGZX=0
     EPS=0
    PRINT *, 'ENTER NAME OF DATA FILE:'
    READ '(A)', FNAME
    OPEN (UNIT = 15, FILE = FNAME, STATUS = 'OLD')
    OPEN (UNIT=16,FILE='rich.out')
100  FORMAT(6I8)
120  FORMAT(3I10)
140  FORMAT(8E10.3E2)
    READ (UNIT = 15, FMT = 100, IOSTAT = EOF) EID,I1,I2,I3,I4,I5
10   IF (EOF .GE. 0) THEN
       COUNT = COUNT + 1
       WRITE (16,120) EID,NPLANE,NTHICK
       WRITE (16,140) TAW, SIGXX, SIGYY, SIGZZ, SIGXY, SIGYZ,
   +SIGZX, EPS
       READ (UNIT = 15, FMT = 100, IOSTAT = EOF)EID,I1,I2,I3,
   +I4,I5
    GO TO 10
    END IF
    CLOSE (15)
    CLOSE (16)
    END
```

F. Keyword Input File for LS-DYNA

Below is the keyword input file used to model the collapsible tube oscillatory model for $P_E - P_2 = 10$ cmH_2O and $Q = 1$ litre/min. Much of the numerical data has been excluded for brevity.

```
*KEYWORD
*CONTROL_STRUCTURED
*TITLE
OSCILLATORY TUBE MODEL
*CONTROL_TERMINATION
0.75          00.0     0.0     0.0
*CONTROL_CONTACT
   0.10           2      0      1      1      1
     0      0     10      0    4.0      0      0
*CONTROL_ALE
      1      1    10.0     0.0     0.0          0
0.0     0.0          11.0000E-040.0          2
*DATABASE_BINARY_D3PLOT
0.0           5      0      0
*DATABASE_BINARY_D3THDT
0.0           5
*MAT_ELASTIC
$HMNAME MATS      2flexshell
      2 6.440E-10 0.91     0.49     0.0      0.0      0.0
*MAT_NULL
$HMNAME MATS      1water
      1 9.980E-10 -1.0     1.000E-09 0.0      0.0
*MAT_NULL
$HMNAME MATS      6contactnullin
      6 9.200E-10                              1.3      0.49
*MAT_NULL
$HMNAME MATS      7contactnullout
      7 9.200E-10                              1.3      0.49
*MAT_RIGID
$HMNAME MATS      5rigid
      5 7.800E-09 1000.0   0.3      0.0      0.0      0.0
 1.0     7.0           7
 0.0     0.0     0.0     0.0     0.0     0.0
*PART
MAIN FLUID SECTION
      1      1      1      5      0      0      0
*PART
INLET RESERVOIR
      2      2      1      5      0      0      0
*PART
OUTLET RESERVOIR
      3      3      1      5      0      0      0
*PART
EXTERNAL RESERVOIR
```

```
     4     4     1     5     0     0     0
*PART
FLEXIBLE SHELLS
     5     6     2     0     0     0     0
*PART
DUMMY VOID FOR USE WITH ELEMENT FORMULATION 12 (define as
initial void)
     6     1     1     5     0     0     0
*PART
FLOWMETER (PART OF MAIN FLUID SECTION)
     7     1     1     5     0     0     0
*PART
INLET RIGID TUBE CONTACT
     9     7     5     0     0     0     0
*PART
OUTLET RIGID TUBE CONTACT
    11     7     5     0     0     0     0
*PART
CONTACT
    12     6     6     0     0     0     0
*PART
CONTACT
    13     6     7     0     0     0     0
*SECTION_SHELL
     6     2   1.0    20.0   0.0          0
0.5   0.5   0.5   0.5   0.0
     7     2   1.0    20.0   0.0          0
0.01  0.01  0.01  0.01  0.0
*SECTION_SOLID_ALE
     1     6     0
0.0   0.0   0.0   0.0   0.0   0.0   0.0
*SECTION_SOLID_ALE
     2     7     4
0.0   0.0   0.0   0.0   0.0   0.0   0.0
*SECTION_SOLID_ALE
     3     7     4
0.0   0.0   0.0   0.0   0.0   0.0   0.0
*SECTION_SOLID_ALE
     4     7     4
0.0   0.0   0.0   0.0   0.0   0.0   0.0
*CONSTRAINED_LAGRANGE_IN_SOLID
     5     1     1     1     0     2
  0.0011     0
*EOS_GRUNEISEN
     540000.0  1.979   0.0    0.0    0.11   3.0    0.0
0.0
*NODE
   1 0.0        9.64        0.0
   "node data"
 96026 63.15789469421  -3.573488708438 -1.001692374791
```

```
*ELEMENT_SHELL
  80757     5   473   474   469   470
  "shell element data"
  91396    13  96024  96023  96025  96026
*ELEMENT_SOLID
     1     1  6938  6939  6940  6941  8061  8062  8063  8064
     "solid element data"
  79956     7 10284 10283 10280 10281 11407 11406 11403 11404
*CONTACT_AUTOMATIC_NODES_TO_SURFACE_TITLE
      1inlet contact
     777     778       4       0                   0       0
0.0      0.0     0.0     0.0     0.0          0 0.0       1.0E+20
     1.0     1.0                  1.0     1.0     1.0     1.0
      0    0.10       0   1.02500.0           2             1
0.0           0       0       0
*SET_NODE_LIST
     777
    90939   90940   90941   90942   90943   90944   90945   90946
    "node list"
    91435   91436   91437   91438   91439   91440   91441   91442
*SET_SEGMENT
     778
     665     667     661     662
     "segment list"
    92157   92156   92158   92159
*CONTACT_AUTOMATIC_NODES_TO_SURFACE_TITLE
      2contact outlet
     888     889       4       0                   0       0
0.0      0.0     0.0     0.0     0.0          0 0.0       1.0E+20
     1.0     1.0                  1.0     1.0     1.0     1.0
      0    0.10       0   1.02500.0           2             1
0.0           0       0       0
*SET_NODE_LIST
     888
    91065   91066   91067   91068   91069   91070   91216   91217
    "node list"
    91891   91892   91893   91894   91895   91896   91897   91898
*SET_SEGMENT
     889
     4005    4006    4140    4138
     "segment list"
    96024   96023   96025   96026
*BOUNDARY_SPC_NODE
     8039       0       1       1       1
"load list"
    88629       0       1       1       1
*BOUNDARY_PRESCRIBED_MOTION_NODE
     6916       1       2       1 1.0           0.0
     6916       2       2       3 0.0           0.0
     6916       3       2       3 0.0           0.0
```

```
"load list"
    8038       1       2       1 1.0           0.0
    8038       2       2       3 0.0           0.0
    8038       3       2       3 0.0           0.0
*LOAD_SEGMENT
       6 1.0     0.0         6917     6941     6938     6916
       "load list"
       7 1.0     0.0        22372    24691    24684    22365
*BOUNDARY_PRESCRIBED_MOTION_NODE
       1       1       2       3 0.0000000       0.0
       1       2       2       4 -1.14           0.0
       1       3       2       3 0.00            0.0
"load list"
    95910       1       2       3 0.0000000       0.0012
    95910       2       2       4 -1.034037       0.0012
    95910       3       2       4 -0.176545       0.0012
$
*INITIAL_STRESS_SHELL
    80757       1       1
 0.000E+00-0.270E-01 0.000E+00 0.000E+00 0.000E+00 0.000E+00 0.000E+00
0.000E+00
"initial stress info"
    90596       1       1
 0.000E+00-0.270E-01 0.000E+00 0.000E+00 0.000E+00 0.000E+00 0.000E+00
0.000E+00
*DEFINE_CURVE
$ INLET VELOCITY
       1       0 1.0     1.0     0.0     0.0           0
  0.0             0.0
  0.0015          0.0
  0.1015          12.6
  1.0015          126.0
*DEFINE_CURVE
$ ZERO MOVEMENT
       3       0 1.0     1.0     0.0     0.0           0
  0.0             0.0
  1.0             0.0
*DEFINE_CURVE
$ PREFORMING OF TUBE
       4       0 1.0     1.0     0.0     0.0           0
  0.0             0.0
  0.00005           0.0001
  0.00095           0.9999
  0.001           1.0
  1.0             1.0
*DEFINE_CURVE
$ TIME BETWEEN D3PLOT AND THIS DUMPS
       5       0 1.0     1.0     0.0     0.0           0
  0.0             0.040
  1.0             0.040
```

```
*DEFINE_CURVE
$ INLET PRESSURE
      6       0 1.0      1.0      0.04      0.0            0
    0             0
"curve data"
    1             0
*DEFINE_CURVE
$ EXTERNAL PRESSURE
      7       0 1.0      1.0      0.04      0.0            0
    0             0
    "curve data"
    1             0
*END
```

G. Evaluation of FSI in MSC.DYTRAN

MSC.DYTRAN version 4.7 was evaluated over a two-month period beginning in March 2000. MSC.DYTRAN is a general-purpose, explicit finite element analysis program for simulating the non-linear dynamic response of solid components and structures. MSC.DYTRAN can also be used to effectively simulate more complex non-linear analysis problems, such as material flow and coupled fluid-structure interaction.

The explicit finite element technology for solving non-linear structural analysis problems is based primarily on the same algorithms used in LS-DYNA and originally developed at the Lawrence Livermore Laboratory and subsequently enhanced by MSC.

The material flow and coupled FSI technology in MSC.DYTRAN was developed entirely at MSC, and was based on an Eulerian formulation. The foundation for this technology came from MSC's 1990 acquisition of Pisces International and the PISCES software program, originally developed to solve complex FSI problems in the nuclear and defence industries.

Typical MSC.DYTRAN applications involving FSI mirror those applications of LS-DYNA; these include airbag inflation, bird strike on aircraft structures, and structural response to underwater explosion [51]

MSC.DYTRAN shares many fundamental similarities with the LS-DYNA technique described in section 4.1. It should be noted, however, that although the basic techniques were the same the details were different. Such differences do not need to be listed here since an in-depth mathematical analysis of the numerical codes was not the aim of this research. For the purposes of the MSC.DYTRAN evaluation, MSC.DYTRAN and LS-DYNA were assumed the same with some differences regarding the treatment of fluids and fluid-structure coupling. The differences that concerned this research are given below.

G.1 Elements

The fluid model was constructed using eight-noded hexahedral solid elements. These were defined as hydrodynamic elements within an Eulerian control volume. The Lagrangian structure utilised four-noded shell elements using the linear elastic material model.

MSC.DYTRAN also offered an ALE algorithm. However, viscosity for fluids was only implemented in the Eulerian ROE solver and the ROE solver could not be used in conjunction with the ALE formulation therefore viscous fluids could not be analysed in a model using the ALE formulation.

G.2 Boundary Conditions

The boundaries of the Eulerian mesh required definition. MSC.DYTRAN allowed pressure; velocity; flow, slip and no-slip wall boundaries. MSC.DYTRAN did not allow Eulerian boundary loads to be defined as load curves in the time domain. No transient loads were therefore possible. This also meant that any loads were applied instantaneously.

MSC.DYTRAN used an automatic coupling algorithm to calculate the physics of FSI. The first task in coupling the Eulerian and Lagrangian sections of the model was to create a surface on the Lagrangian structure. The surface on the Lagrangian

structure was used to transfer forces between the two parts in a similar way as that described in section 4.1.5.
In order to meet MSC.DYTRAN's internal requirements the coupling surface needed to have a positive volume. This meant that the normals of all the segments of the surface had to point outwards. More importantly the coupled surface had to form a closed volume. This was fundamental to the way the coupling worked in MSC.DYTRAN. It meant that there could be no holes in the surface and the surface had to be closed. The closed volume formed by the coupling surface had to intersect at least one Euler element; otherwise the coupling surface was not recognised by the Eulerian mesh.

G.3 Pre- And Post-Processing For MSC.DYTRAN

The fluid and structural parts were created simultaneously using MSC.PATRAN version 8.0. This coupled model was then converted into an MSC.DYTRAN input file using the standard preference template file in MSC.PATRAN. Significant editing of the resulting input file was required in order to achieve fluid flow and FSI. MSC.DYTRAN and MSC.PATRAN were installed on a SUN ULTRA 10 (Ticker).

G.4 MSC.DYTRAN Model Of A Collapsible Tube

The two-month evaluation of MSC.DYTRAN included a brief analysis of the collapsible tube phenomena. The model was not expected to produce results worthy of comparison with experiments but was simply used to highlight the problems one might face if one wished to use MSC.DYTRAN to model such an event.
The MSC.DYTRAN model was primitive in that the element meshes were coarse and there was simply a short length of tube subjected to an internal flow and a negative transmural pressure. No other parameters, such as tension, pre-stress or contact were considered.

G.4.1 Construction Of The MSC.DYTRAN Model

The fluid control volume consisted of one part (the main fluid control volume) made up of 2625 hexahedron Eulerian elements. The control volume was cylindrical with a diameter of 15 mm and length of 26 mm.
The tube was modelled as a hollow cylinder of 448 quadrilateral Lagrangian elements. No preforming could take place due to the non-transient nature of the Eulerian boundaries so there was no defined plane of collapse. The cylinder was 26.5 mm long with a diameter of 13 mm. 65 triangular Lagrangian elements were used to close off the volume of the tube in order to meet MSC.DYTRAN's internal requirements for FSI.

G.4.2 Model Properties

The polynomial equation of state was used for the fluid whereby the speed of sound was defined via the bulk modulus and the density. The fluid density was $\rho_f = 1000$ kg/m^3, viscosity was $\mu = 0.001$ Pa s and bulk modulus was $K = 2.2$ MPa. The minimum pressure cut-off was set to –10 MPa. These values resulted in a fluid speed of sound of approximately 47 m/s. The material properties of the tube were E =1.1 MPa, $\rho_s = 1000$ kg/m^3 and $\nu = 0.4$.
The free surface at the inlet end of the fluid control volume was defined as a flow boundary where fluid could either flow in or out. The outlet face was defined as a pressure boundary of an arbitrarily chosen magnitude of –0.1MPa. The definition of

the external face of the control volume was unimportant since the elements outside of the Lagrangian structure were not processed; however, a flow boundary was defined. Coupling of the fluid and structural parts was problematic as the coupling surface needed to form a closed positive volume. In order to create a closed volume, it was necessary to create dummy elements at the ends of the tube. These had to lie outside of the Eulerian control volume in order that they did not interfere with the fluid flow. They also had to be far enough from the deformable Lagrangian elements as not to interfere with their deformation.
The coupling was defined so that the Eulerian elements inside the cylinder were the contact elements and the Eulerian elements outside the cylinder were ignored.
The nodes at both ends of the closed cylinder were rigidly restrained in all directions but were allowed to rotate.

G.4.3 Results and Discussion

Sectional views before and after the application of the pressure load can be seen in figure 0.1. Half the structure and half the control volume are shown.

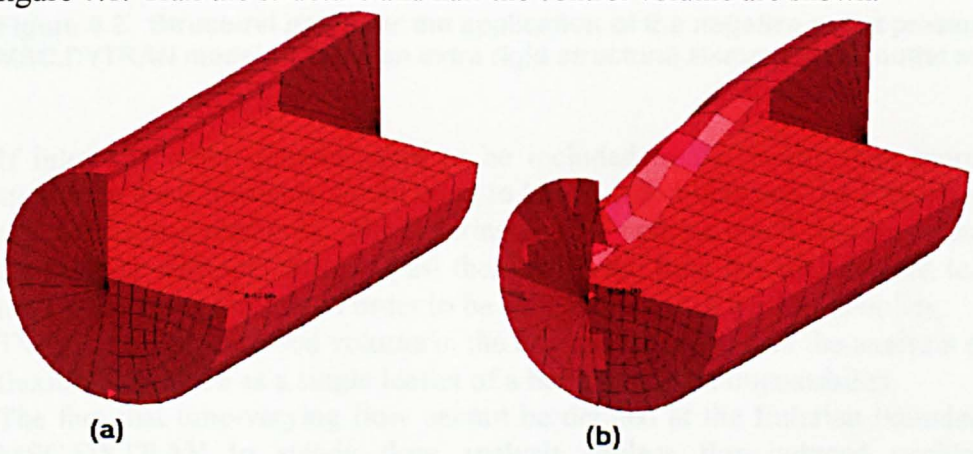

figure 0.1 Sectioned views of the fluid and structural parts (a) before and (b) after the application of the negative outlet pressure load.

The plane of collapse was not defined so the shell elements simply folded alternately inwards and outwards and formed a star shaped cross-sectional profile at the neck.
The dummy triangular elements can be seen at the end of the structure placed just outside the fluid control volume (figure 0.1 (a)). When the analysis begun and the tube collapsed the shell elements of the cylinder moved so far that they passed beyond these dummy elements, the coupling surface turned inside out and had a negative volume, causing MSC.DYTRAN to terminate (figure 0.1 (b)). This problem was resolved by including another row of shell elements in the cylinder before the dummy elements as shown in Figure 0.2 (dummy elements not shown).

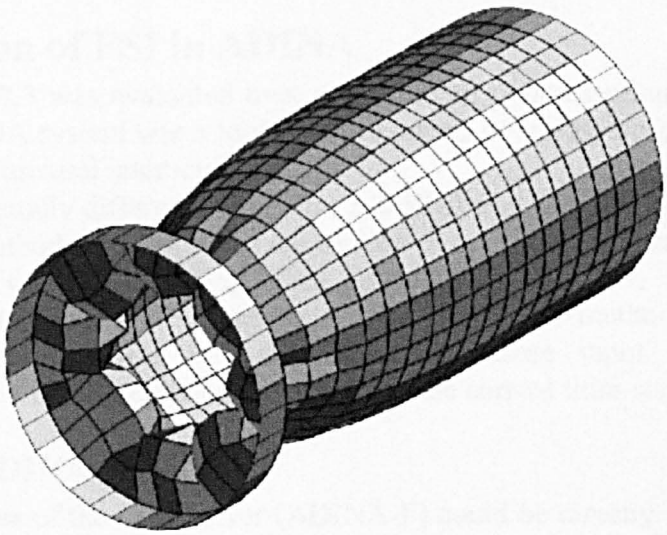

Figure 0.2. Structural part after the application of the negative outlet pressure for the MSC.DYTRAN model utilising an extra rigid structural element at the outlet end

If inlet and outlet lengths were to be included in the model then more rows of stationary shell elements would need to be modelled between the collapsible section and the dummy elements. The Eulerian control volume could then be extended up to the dummy elements, but not past them since the flow boundaries need to be inside the Lagrangian structure in order to be acknowledged in the FSI coupling.
The need for an enclosed volume in the FSI technique renders the analysis of a single flexible flap (such as a single leaflet of a heart valve) an impossibility.
The fact that time-varying flow cannot be defined at the Eulerian boundaries limits MSC.DYTRAN to steady flow analysis (unless flow-induced oscillations are achieved). This means that the modelling of pulsatile flow is out of the question.
Another limitation of the non-transient boundaries is that preforming cannot be carried out. A pre-stressed structure can be analysed in MSC.DYTRAN but the pre-stressing would need to be carried out in a separate model.

G.4.4 Conclusions Drawn From The MSC.DYTRAN Model

MSC.DYTRAN is currently unsuitable for modelling such systems as the collapsible tube and heart valves. This is because of the need for an enclosed volume in the FSI technique used. Other problems include the inability to model transient fluid-flow boundary conditions.

H. Evaluation of FSI in ADINA

ADINA version 7.3 was evaluated over a one-month period beginning in February 2000. The ADINA system was a tool for the analysis of solids, structures, fluids and fluid flow with structural interactions.

ADINA fundamentally differed from both LS-DYNA and MSC.DYTRAN in that the time-stepping method was implicit (see section 3.2). Transient analyses could be performed with variable time-step sizes, as input by the user, or by using an automatic-time-stepping (ATS) method. In the ATS method, the program automatically decreased the time-step size from those input by the user if convergence in the iterations was not reached for the current time-step considered.

H.1 FSI In ADINA

All the capabilities of the CFD solver (ADINA-F) could be directly used with all the capabilities of the structural solver (ADINA) in a fully coupled analysis. Entirely different meshes could be used for the structural and the fluid flow idealisations. For FSI boundaries an ALE formulation was used. The motion of an ALE mesh can either be user prescribed or automatically induced by the motion of an attached Lagrangian structure. This latter application of ALE is used in the solution of coupled FSI problems in ADINA. It involves a slideline being placed between the fluid and the structure so that the fluid and structural boundaries are clearly defined. The fluid is treated like an ALE formulation. This allows fluid to flow around the structure and deform it. The ALE mesh is deformed with the FSI interface. In this case the Lagrangian structure does not move through the fluid mesh but instead distorts it in some way (Figure 0.3).

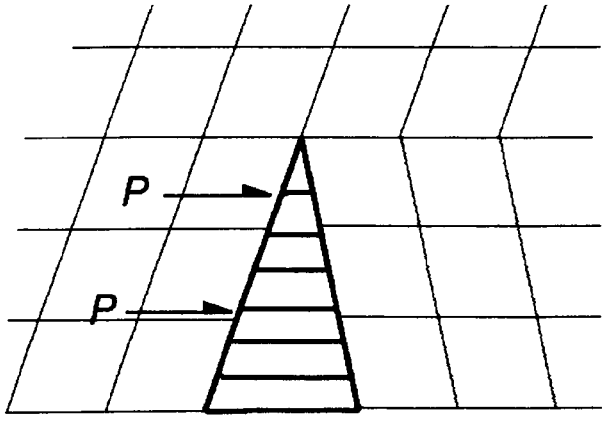

Figure 0.3. Coupling method used in ADINA showing a Lagrangian structural mesh within an ALE fluid mesh.

Due to limited time in which to evaluate ADINA the models were mainly two-dimensional. The fluid and structural parts were modelled separately. Firstly the structure was created using a Lagrangian surface of 2D plane-strain solid elements. The edges of the structure that were the intended FSI lines were copied into the fluid model and the fluid mesh was constructed around them i.e. a hole was left in the fluid mesh that would perfectly contain the structure. The fluid mesh consisted of four-noded planar elements.

Pressures, velocities, walls or FSI could be defined at the fluid mesh boundaries. Where FSI was used it was sometimes necessary to define leader and follower nodes in order to maintain acceptable mesh quality. The leader node was situated on the FSI boundary and the follower node was situated at a wall boundary some distance from the leader. During the analysis the follower node, and all nodes in between it and the leader node, displaced along the wall as the leader node displaced. If no leaders and followers were defined and large displacement occurred then the mesh may have become unduly distorted.

H.2 Pre- And Post-Processing For ADINA

An important aspect of ADINA was that the CFD capability (ADINA-F) was an integral part of the complete ADINA System, using the same graphical user interface based pre-processor (ADINA-IN) and post-processor (ADINA-PLOT) as used for the structural solver (ADINA).

H.3 ADINA Model Of Flow Over A Cylinder

During the evaluation of ADINA a flow over a cylinder model was analysed. This came as an example model with the software. The solution of the model appeared to give oscillations at a frequency of 10 Hz for a Reynolds number of 380. However, on closer inspection it was discovered that a movement of the cylinder wall started off these oscillations and the frequency of vortex shedding was related to this. It was also observed in the results that the amplitude of the transverse fluctuations was getting smaller as time progressed. This suggested that the vortex shedding may have vanished altogether if the model was left to run for long enough. Flow-induced vortex shedding was not achieved with ADINA in this study.

The cylinder model was altered to include a flexible flap attached to the rear. The model was not intended to give any results for quantitative or qualitative comparisons. The purpose of this model was as an example of the FSI produced from the ALE coupling technique used in ADINA. The velocity vectors at an arbitrary time can be seen in Figure 0.4.

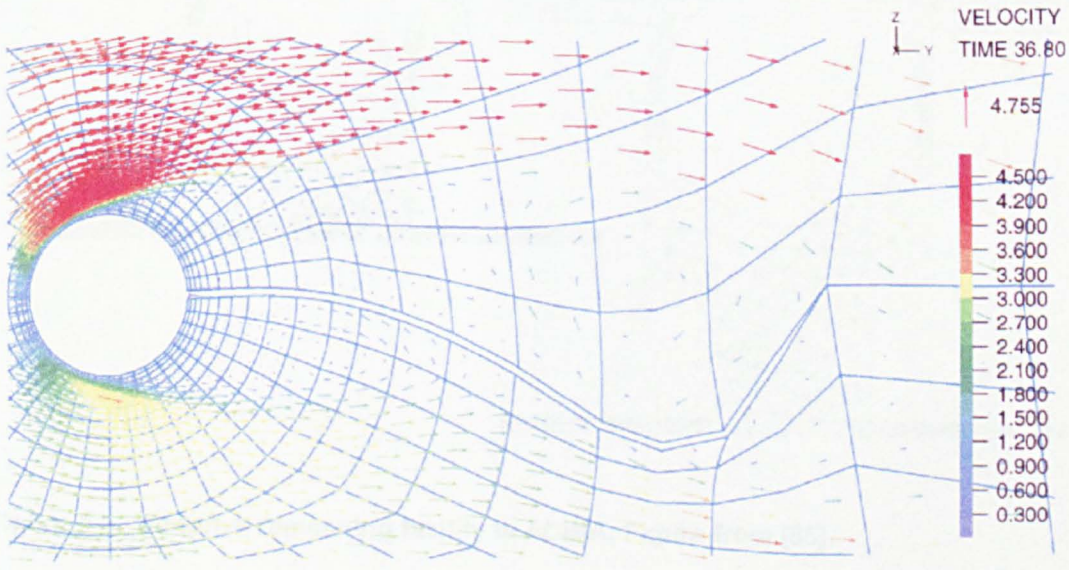

Figure 0.4. ADINA model of a flexible flap attached to the rear of a circular cylinder in fluid flow.

The fluid can be seen to flow through the ALE mesh while maintaining a deformable boundary with the flexible structure.
Figure 0.4 highlights one of the limitations of the sliding boundary technique of FSI. The ALE mesh distorted with the structure so if the deformation or displacement were large enough the ALE mesh would distort too much and cause the calculations to crash. The likelihood of this happening is increased when a structure is expected to fold over another structure. Contact between structures in the flow would be impossible with this method of FSI.
A solution to this problem is adaptive remeshing. ADINA has recently been enhanced with an adaptive remeshing capability. When the fluid mesh becomes too distorted for the solution to continue a complete restructuring of the mesh is performed. This can be seen in Figure 0.5 for a two-dimensional model of a ball valve. The ball moves upwards and the fluid mesh distorts but before the solution crashes the model is remeshed completely and the solution is allowed to continue. This remesh differs from those in ALE or Eulerian time-steps in that the structure and connectivity of the mesh is altered as well.
Of course the problem with adaptive remeshing involves CPU cost. Currently this facility only exists in two-dimensional analyses in ADINA.

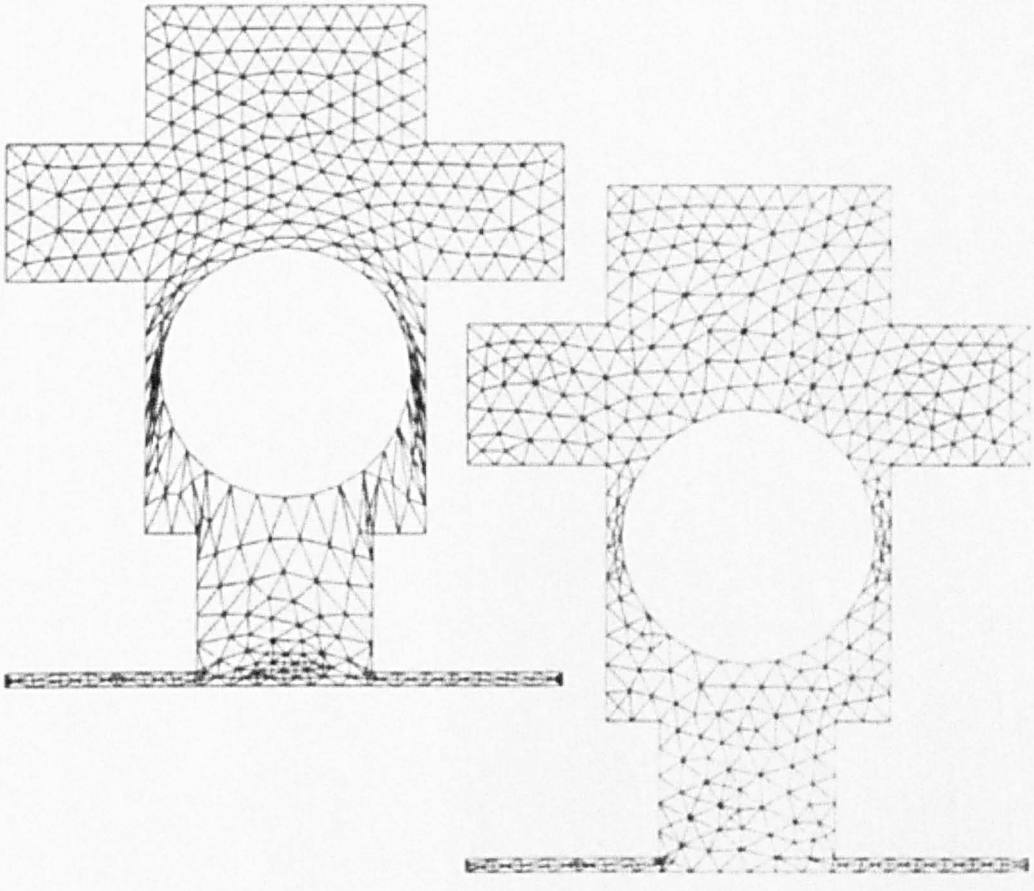

Figure 0.5. Adaptive remeshing facility in ADINA. Figure from [85].

---

85 Adina System Newsletter, Vol 2, Issue 2, ADINA R and D, Watertown, MA, December 1999.